

Air Force Institute of Technology

**AFIT Scholar**

---

Theses and Dissertations

Student Graduate Works

---

9-2011

## Hyperspectral-Based Adaptive Matched Filter Detector Error as a Function of Atmospheric Profile Estimation

Allan W. Yarbrough

Follow this and additional works at: <https://scholar.afit.edu/etd>



Part of the [Atmospheric Sciences Commons](#), and the [Signal Processing Commons](#)

---

### Recommended Citation

Yarbrough, Allan W., "Hyperspectral-Based Adaptive Matched Filter Detector Error as a Function of Atmospheric Profile Estimation" (2011). *Theses and Dissertations*. 1306.

<https://scholar.afit.edu/etd/1306>

This Dissertation is brought to you for free and open access by the Student Graduate Works at AFIT Scholar. It has been accepted for inclusion in Theses and Dissertations by an authorized administrator of AFIT Scholar. For more information, please contact [richard.mansfield@afit.edu](mailto:richard.mansfield@afit.edu).



HYPERSPECTRAL-BASED ADAPTIVE MATCHED FILTER DETECTOR  
ERROR AS A FUNCTION OF ATMOSPHERIC PROFILE ESTIMATION

DISSERTATION

Allan W. Yarbrough, Major, USAF

AFIT/DEE/ENG/11-13

DEPARTMENT OF THE AIR FORCE  
AIR UNIVERSITY

**AIR FORCE INSTITUTE OF TECHNOLOGY**

Wright-Patterson Air Force Base, Ohio

APPROVED FOR PUBLIC RELEASE; DISTRIBUTION UNLIMITED.

The views expressed in this thesis are those of the author and do not reflect the official policy or position of the United States Air Force, Department of Defense, or the United States Government. This material is declared a work of the U.S. Government and is not subject to copyright protection in the United States.

AFIT/DEE/ENG/11-13

HYPERSPECTRAL-BASED ADAPTIVE MATCHED FILTER DETECTOR  
ERROR AS A FUNCTION OF ATMOSPHERIC PROFILE ESTIMATION

DISSERTATION

Presented to the Faculty  
Graduate School of Engineering and Management  
Air Force Institute of Technology  
Air University  
Air Education and Training Command  
in Partial Fulfillment of the Requirements for the  
Degree of Doctor of Philosophy

Allan W. Yarbrough, B.E.E., M.S.E.E.  
Major, USAF

September 2011

APPROVED FOR PUBLIC RELEASE; DISTRIBUTION UNLIMITED.

HYPERSPECTRAL-BASED ADAPTIVE MATCHED FILTER DETECTOR  
ERROR AS A FUNCTION OF ATMOSPHERIC PROFILE ESTIMATION

Allan W. Yarbrough, B.E.E., M.S.E.E.  
Major, USAF

Approved:



Maj Michael J. Mendenhall, PhD  
(Chairman)

31-AUG-2011

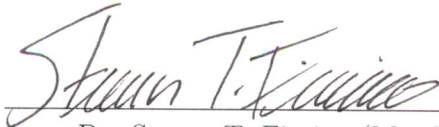
date



Dr. Richard K. Martin (Member)

31 Aug 2011

date



Dr. Steven T. Fiorino (Member)

31 Aug 11

date

Accepted:



M. U. Thomas

10 Sep 11

Date

Dean, Graduate School of Engineering and Management

*Abstract*

Hyperspectral imagery is collected as radiance data. This data is a function of multiple variables: the radiation profile of the light source, the reflectance of the target, and the absorption and scattering profile of the medium through which the radiation travels as it reflects off the target and reaches the imager. Accurate target detection requires that the collected image matches as closely as possible the known “true” target in the classification database. Therefore, the effect of the radiation source and the atmosphere must be removed before detection is attempted.

While the spectrum of solar light is relatively stable, the effect of the atmosphere on this profile varies significantly depending on multiple atmospheric parameters. There are several data processing methods available to researchers for removing the influence of these parameters; however, little research has been done to describe, in a general way, how the uncertainty and error associated with these methods affects target detection. Our objective is to characterize the uncertainty in the detection method due to the uncertainty in the estimation of atmospheric parameters. We apply a range of atmospheric profiles, correlated with relative humidity, to a radiative transfer model-based prediction of the atmospheric extinction effect using simulated hyperspectral imagery. These profiles are taken from known distribution percentiles as obtained from historic meteorological measurements at the simulated sites. We quantify the expected detection error, given the range of atmospheric conditions in the historic profile. We show that temporal variation in atmospheric parameters across their distribution impacts the accuracy of target detection. We show that this impact is more acute at high humidity than at low humidity. We show that, given the uncertainty associated with atmospheric profile estimation, the optimum assumption for purposes of target detection may be other than their median values, and that this effect is target dependent.

## *Acknowledgements*

I would like to thank Maj Mendenhall, Dr. Fiorino, and Dr. Martin for their assistance and encouragement, and Christina Schutte, Vincent Velten, and Phil Hanna for their sponsorship of my research. I would also like to thank my family for their patience and support over these years.

Allan W. Yarbrough

## Table of Contents

	Page
Abstract . . . . .	iv
Acknowledgements . . . . .	v
List of Figures . . . . .	viii
List of Tables . . . . .	xi
List of Symbols . . . . .	xii
List of Abbreviations . . . . .	xiv
I. Introduction . . . . .	1
1.1 Motivation . . . . .	1
1.2 Problem . . . . .	3
1.3 Scope . . . . .	6
1.4 Research Question . . . . .	7
1.5 Overview . . . . .	7
II. Background . . . . .	9
2.1 Adaptive Matched Filter . . . . .	9
2.2 A Survey of Atmospheric Correction . . . . .	12
2.2.1 Radiative Transfer . . . . .	12
2.2.2 Mathematical Methods . . . . .	14
2.2.3 In-Scene Correction . . . . .	19
2.2.4 Conclusion . . . . .	21
2.3 Empirical Line Correction (An In-scene Methodology) . . . . .	22
2.4 Radiative Transfer . . . . .	26
2.4.1 Pressure Broadening . . . . .	29
2.4.2 Doppler Broadening . . . . .	30
2.4.3 Density Effect . . . . .	31
III. Methodology . . . . .	32
3.1 Distances Between Atmospheres . . . . .	32
3.1.1 Water Vapor Relationships . . . . .	33
3.1.2 Water Vapor vs. Radiance Euclidean Distance Relationship . . . . .	36
3.2 Target Detection with the AMF . . . . .	40
3.3 Evaluating Target Detection Error . . . . .	41

	Page
3.3.1	The Bhattacharyya Coefficient . . . . . 41
3.3.2	AMF Detection with Atmospheric Error: a Pedagogical Example . . . . . 44
3.3.3	Determining the Best Atmospheric Assumptions . . . . . 49
3.4	Simulation Methodology . . . . . 49
3.4.1	Atmospheric Parameters . . . . . 51
3.4.2	PLEXUS . . . . . 52
3.4.3	Image Simulation . . . . . 52
IV.	Results . . . . . 54
4.1	Data . . . . . 54
4.1.1	DIRSIG-Generated Imagery . . . . . 54
4.1.2	Target Set . . . . . 56
4.1.3	Atmospheric Data . . . . . 58
4.2	Receiver Operating Characteristic as a Function of Atmospheric Percentile . . . . . 59
4.2.1	The ROC Explained . . . . . 59
4.2.2	ROCs by Target . . . . . 60
4.2.3	ROCs by Percentile . . . . . 62
4.3	Area under the Curve (AUC) as a ROC Performance Measure . . . . . 65
4.4	AUC Contours as a Function of True Atmosphere and Estimated Atmosphere . . . . . 70
4.5	Probability of Detection ( $P_d$ ) at a Constant Probability of False Alarm ( $P_{fa}$ ): Contour Plots . . . . . 71
4.6	Summary of Results . . . . . 74
V.	Conclusion . . . . . 78
5.1	Summary . . . . . 78
5.2	Contributions . . . . . 79
5.3	Possibility of Future Work . . . . . 80
	Bibliography . . . . . 81
Appendix A.	Spectral Signatures for All Automobiles . . . . . 85
Appendix B.	In-color ROC Curves by Percentile Atmosphere . . . . . 96
Appendix C.	Full-background ROC Curves by Percentile Atmosphere . . . . . 105
Appendix D.	AUC Contour Plots . . . . . 108
Appendix E.	$P_d$ Contour Plots . . . . . 117

## *List of Figures*

Figure		Page
1.	An example of a hyperspectral imagery (HSI) data cube shown as a three-dimensional matrix. . . . .	1
2.	Sunlight and skylight incident on a target. . . . .	3
3.	Plots of (a) spectral signatures and (b) average radiance by wavelength (feature) for four colored panels. . . . .	4
4.	Acquisition through detector response flow. . . . .	5
5.	Plot of laboratory-measured reflectance vs. image radiance for dimension 9 of four known classes. . . . .	24
6.	Plot of the first two principal components for four colored panels as corrected by the ELC method, overlaid with the same features from the spectral library signatures. . . . .	25
7.	Plot of ED between atmospheric water vapor content profiles ( $x$ -axis) and EDs between total atmospheric transmittances, target reflectances, and sensor-reaching radiances as modeled under those profiles ( $y$ -axis). . . . .	38
8.	Process flowchart detailing methodology that performed detection in radiance space using target spectra taken from class averages as they appear in the fiftieth percentile DIRSIG image. . . . .	42
9.	Plots of Bhattacharyya coefficients comparing the AMF output corresponding to each of nine percentile distributions of the atmospheric parameters to that of the other eight distributions. . . . .	43
10.	Scatter plots of targets (blue), decoys (red), and background (yellow) in two-dimensional hyperspectral space and associated AUC plots by estimated target location. . . . .	45
11.	Scatter plots of targets (blue), decoys (red), and background (yellow) in two-dimensional hyperspectral space and associated AUC plots by estimated target location. . . . .	48

Figure		Page
12.	Two examples from Appendix D of contour plots of the AUC for AMF detection of automobiles of the indicated colors as a function of estimated atmospheric profile ( $x$ -axis) and true atmospheric profile ( $y$ -axis), measured in percentiles of their historic distribution of relative humidity. . . . .	50
13.	Process flowchart detailing methodology that performed detection in reflectance space using PLEXUS-generated radiance data to convert image data cube to reflectance. . . . .	51
14.	The RGB representation of the simulated hyperspectral image of DIRSIG's "Megascene" RIT's by-element construction of a Rochester NY suburb [28]. . . . .	54
15.	Reflectance spectra for the green, gold, silver, and white automobiles. . . . .	57
16.	Plots of the atmospheric dew point percentile versus (a) the dew point value and (b) the atmospheric temperature in $^{\circ}F$ corresponding to that percentile. . . . .	58
17.	Receiver Operating Characteristic (ROC) curves for AMF detection of examples of the green, gold, silver, and white cars. . . .	61
18.	In-color ROC curves for the median, 25 <sup>th</sup> percentile, and 75 <sup>th</sup> percentile automobile. . . . .	64
19.	AUCs from AMF detection of automobiles with unique color combinations. . . . .	66
20.	AUCs from AMF detection of maroon, green, gold, and blue automobiles. . . . .	68
21.	AUCs from AMF detection of red, silver, white, and black automobiles. . . . .	69
22.	Contour plots of the average AUCs for AMF detection of the gold and green cars with the $P_{fa}$ 's calculated from false alarms generated by all background pixels, automobile pixels only, and like-color automobile pixels. . . . .	70

Figure		Page
23.	Contour plots of the average AUCs for AMF detection of the silver and white cars with the $P_{fa}$ 's calculated from false alarms generated by all background pixels, automobile pixels only, and like-color automobile pixels. . . . .	72
24.	Contour plots of the average ROC $P_d$ when $P_{fa} = 0.05$ for AMF detection of the gold and green cars with the $P_{fa}$ 's calculated from false alarms generated by all background pixels, automobile pixels only, and like-color automobile pixels. . . . .	74
25.	Contour plots of the average ROC $P_d$ when $P_{fa} = 0.05$ for AMF detection of the silver and white cars with the $P_{fa}$ 's calculated from false alarms generated by all background pixels, automobile pixels only, and like-color automobile pixels. . . . .	75
26.	Normalized histograms of the optimum atmospheric parameter assumptions along six metrics for purposes of target detection with the AMF. . . . .	77

## *List of Tables*

Table		Page
1.	LLRT Cost Function Definitions . . . . .	10
2.	Table of spectral energies (magnitude scaled by the spectral resolution) of four targets signatures. . . . .	39
3.	List of car colors and their material identification numbers that appear in the “megascene” image. Each material ID indicates a specific automobile. Note that there are often more than one car of the same color. . . . .	55
4.	Performance maximizing atmospheric parameter assumptions for AMF target detection in percentile of the distribution. In the header line, “BG” indicates the detection was performed against the entire background, “AO” indicates the detection was performed against only the class of automobiles, and “CO” indicates the detection was performed against only cars of the same color. Where the “CO” column is empty, there is only one car of that color in our data set. The “Stddev” column shows the standard deviation of the $P_d$ and AUC values for each auto color. . . . .	76

## List of Symbols

Symbol		Page
$c$	Speed of Light . . . . .	15
$h$	Planck's Constant . . . . .	15
$k_B$	Boltzmann's Constant . . . . .	15
$T$	Temperature . . . . .	15
$\lambda$	Wavelength . . . . .	15
$S(\lambda)$	Planck's Formula . . . . .	26
$I$	Irradiance . . . . .	27
$s_1$	Atmosphere Height . . . . .	27
$s_2$	Target Height . . . . .	27
$\tau$	Optical Depth . . . . .	27
$\beta_e$	Extinction Coefficient . . . . .	27
$\beta_a$	Absorption Coefficient . . . . .	27
$\beta_s$	Scattering Coefficient . . . . .	27
$\sigma_e$	Extinction Cross-Section . . . . .	28
$N$	Particle volume density . . . . .	28
$k_a$	Mass Extinction Coefficient . . . . .	28
$\rho$	Atmospheric Density . . . . .	28
$r_m$	Particle Radius . . . . .	28
$\sigma$	Particle Standard Deviation . . . . .	28
$Q_e(m, \lambda, r)$	Extinction Efficiency . . . . .	28
$m$	Particle Mass . . . . .	28
$n$	Water Refractive Index . . . . .	29
$n_0$	Dry Particle Refractive Index . . . . .	29
$r_o$	Dry Particle Radius . . . . .	29
$r(a_w)$	Particle Radius at Given Humidity . . . . .	29

Symbol		Page
$p$	Pressure . . . . .	30
$\nu_0$	Absorption Line Frequency . . . . .	30
$\nu$	Frequency . . . . .	30
$\sigma_\nu$	Absorption Cross-Section per Unit Mass . . . . .	30
$S$	Line Strength . . . . .	30
$w_1$	Constituent Mixing Ratio . . . . .	31
$k_a$	Mass Absorption Coefficient . . . . .	31
$\rho_0$	Atmospheric Density at Sea Level . . . . .	31
$H$	Scale Height . . . . .	31

## *List of Abbreviations*

Abbreviation		Page
BDA	Battle Damage Assessment . . . . .	2
AMF	Adaptive Matched Filter . . . . .	3
HSI	Hyperspectral Imagery . . . . .	6
ARTEMIS	Advanced Responsive Tactically Effective Military Imaging Spectrometer . . . . .	6
MODTRAN	Moderate Resolution Atmospheric Transmission Model . . . . .	6
FLAASH	Fast Line-of-sight Atmospheric Analysis of Spectral Hypercubes . . . . .	6
AUC	Area Under the ROC Curve . . . . .	7
ROC	Receiver Operating Characteristic . . . . .	7
LLRT	Log-Likelihood Ratio Test . . . . .	9
$P_d$	Probability of Detection . . . . .	11
$P_{fa}$	Probability of False Alarm . . . . .	11
ACE	adaptive cosine estimator . . . . .	11
AVIRIS	Airborne Visible/Infrared Imaging Spectrometer . . . . .	12
5S	Satellite Signal in the Solar Spectrum . . . . .	12
LOWTRAN	Low Resolution Atmospheric Transmission Mode . . . . .	13
LRT	Likelihood Ratio Test . . . . .	17
SAM	Spectral Angle Mapper . . . . .	17
HYDICE	Hyperspectral Digital Imagery Collection Experiment . . . . .	18
ISAC	In Scene Atmospheric Correction . . . . .	19
TIR	Thermal Infrared . . . . .	19
VIS-SWIR	Visible-Shortwave Infrared . . . . .	19
CCA	Canonical Correlation Analysis . . . . .	20
SMACC	Sequential Maximum Angle Convex Cone . . . . .	21
NOAA	National Oceanographic and Atmospheric Administration	21

Abbreviation		Page
FSL	Forecast System's Laboratory . . . . .	21
ASTER	Advanced Spaceborne Thermal Emission and Reflection Radiometer . . . . .	22
NASA	National Air and Space Administration . . . . .	22
JPL	Jet Propulsion Laboratory . . . . .	22
ELC	empirical line correction . . . . .	22
BC	Bhattacharyya Coefficient . . . . .	41
PMF	Probability Mass Function . . . . .	41
LDF	Linear Discriminant Functions . . . . .	46
LEEDR	Laser Environmental Effects Distribution Reference . . . . .	50
DIRSIG	Digital Imaging and Remote Sensing Image Generation Model . . . . .	50
AFIT	Air Force Institute of Technology . . . . .	51
HEL JTO	High Energy Laser Joint Technology Office . . . . .	51
HELEEOS	High Energy Laser End to End Operational Simulation . . . . .	52
AFRL	Air Force Research Lab . . . . .	52
PLEXUS	Phillips Laboratory EXpert User Software . . . . .	52
BRDF	Bidirectional Reflection Distribution Function . . . . .	53
RGB	Red, Green, Blue . . . . .	55
SNR	Signal to Noise Ratio . . . . .	76
AGL	Above Ground Level . . . . .	78
MSL	Mean Sea Level . . . . .	78

# HYPERSPECTRAL-BASED ADAPTIVE MATCHED FILTER DETECTOR ERROR AS A FUNCTION OF ATMOSPHERIC PROFILE ESTIMATION

## I. Introduction

### 1.1 Motivation

While the human eye is capable of perceiving radiation in only three broad bands in the visible frequency range, hyperspectral imagers are capable of detecting radiation in hundreds of frequency bands in the visible and near-infrared, nominally 400 - 2500nm. Thus, hyperspectral images can be thought of as a set of co-registered images, where each image measures the radiation intensity at a specific wavelength. If we examine a single pixel, we can collect the measurements at the different wavelengths into an  $n$ -dimensional vector, thus creating an image cube (Fig. 1).

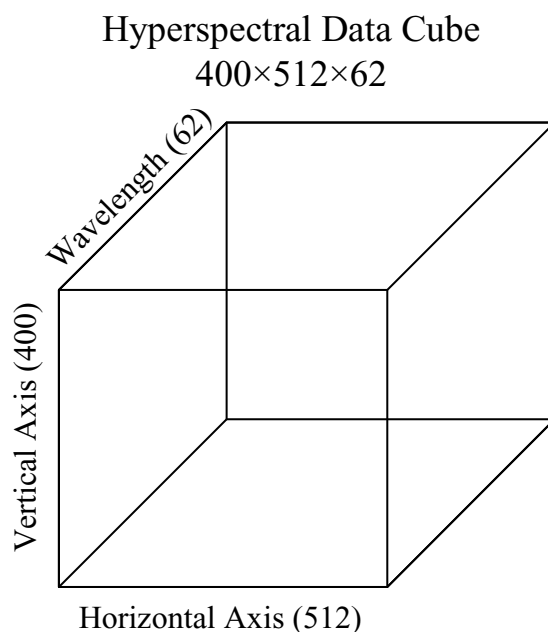


Figure 1: An example of a hyperspectral imagery (HSI) data cube shown as a three-dimensional matrix.

In contrast to traditional imagery collected in the visible wavelengths, which require intensive human analyst examination to exploit, the  $n$ -dimensional vectors obtained from hyperspectral images (as illustrated in Fig. 1) are subject to analysis by highly automated statistical methods. Using these, a wide range of materials can be distinguished from each other in hyperspectral images, even though their “colors” appear identical. This capability has led to the deployment of hyperspectral sensors in biological and geological studies [9], hazard mapping [36], astronomical observations [26], fire fuel mapping [31], and forestry applications [20].

The military has also found many applications of hyperspectral imagery, particularly in reconnaissance and intelligence gathering. The results of target detection and exploitation have a long history in battle damage assessment (BDA), threat identification, and deployment planning. They also have been used in terrain mapping, particularly in quickly identifying locations suitable as aircraft landing zones and special forces insertion. Again, the highly automated nature of hyperspectral imagery exploitation is its most salient advantage over traditional imagery in producing usable intelligence in near-real-time. Mendenhall [35] gives several specific examples of this superiority:

- The effectiveness of traditional imagery is highly dependant on its resolution; this, in turn, is a function of the altitude at which an image is collected. In order to accurately identify a target with traditional imagery, a sufficient number of pixels must be collected to discern shape, structure, and size. In contrast, with hyperspectral imagery, a single pixel, imaged over hundreds of frequency bands, can be sufficient to determine the material type of a target.
- The material type is often the desired datum. This is especially true in detecting the presence of detonated chemical weapons in an area military planners are contemplating troop deployments.

- Surface composition is an inherent feature of hyperspectral imagery, and is useful in identifying trafficable regions for troop deployments and suitable aircraft landing zones.

### 1.2 Problem

The purpose of this work is to gain a better understanding of how a “best guess” on atmospheric parameter estimation affects the ability to do hyperspectral-based target detection using the adaptive matched filter (AMF). As illustrated in Fig. 2, the sun emits energy that is transmitted through the earth’s atmosphere where it is absorbed, scattered, and transmitted to the earth’s surface. Some amount of energy is reflected off of the earth’s surface and transmitted once again through some portion

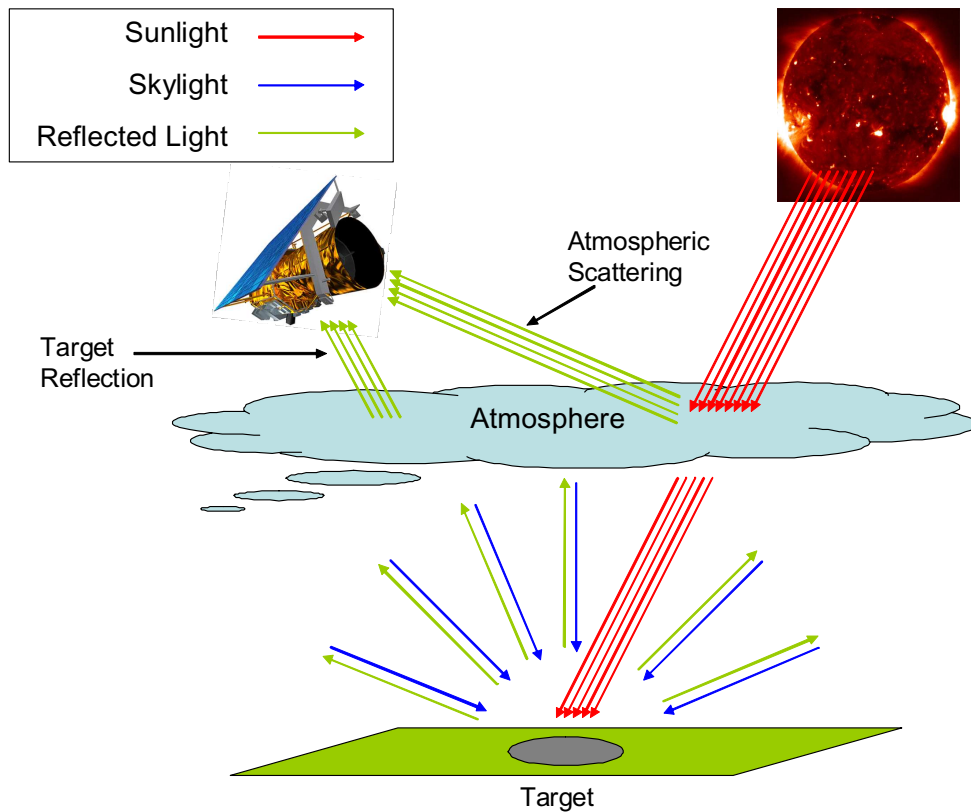


Figure 2: Sunlight and skylight incident on a target. Some of the reflected energy is directed toward the sensor.

of the earth's atmosphere to the sensor, along with some energy scattered by the atmosphere directly to the sensor without having reached the surface.

Consider, for example, the spectral signatures of four different colored panels as shown in Fig. 3(a). These signatures are in units of reflectance as a function of the wavelength of the incident light and were collected with a field spectrometer under laboratory conditions. They reasonably measure the targets' "true" reflectance properties.

Compare with them the signatures in Fig. 3(b). These measurements, in units of  $W/m^2/str$ , were taken from a hyperspectral image as acquired with a hyperspectral camera. The image is of the four panels placed several hundred yards away against a natural background under uniform solar illumination conditions. We can see, in this comparison, that while the spectral signatures of the panels are vaguely recog-

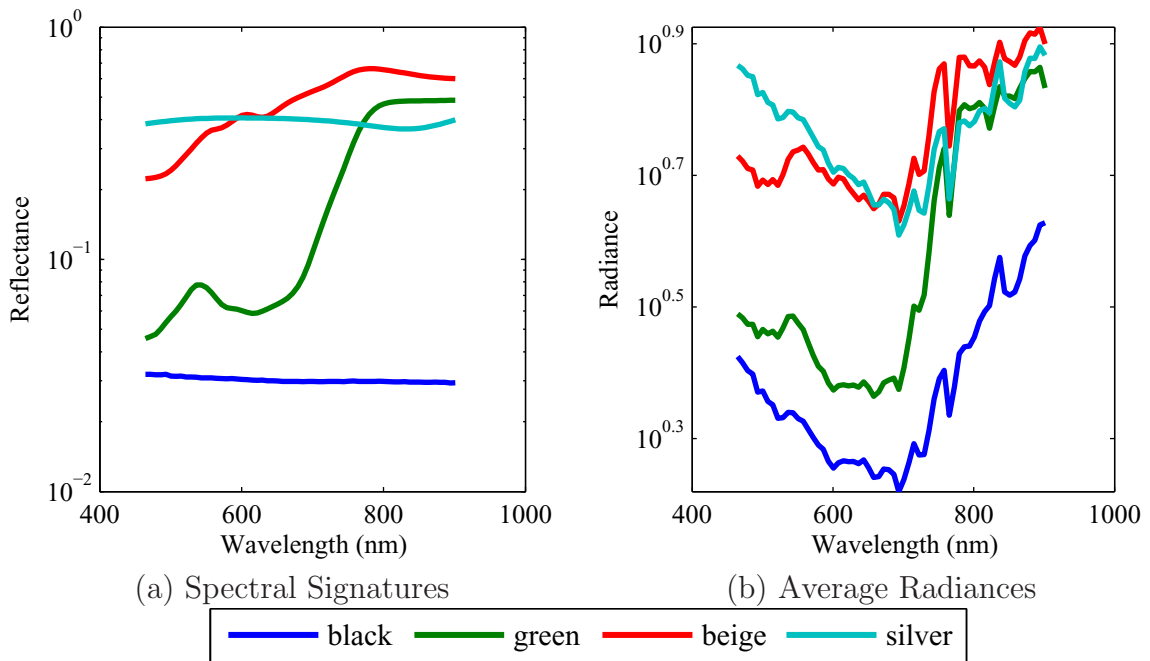


Figure 3: Plots of (a) the spectral signatures and (b) the average radiance by wavelength (feature) for four colored panels. The spectral signatures were collected using a field spectrometer, and serve as the "truth data" against which the radiances from the hyperspectral image are compared. Notice the radiance intensity fadeout in the middle wavelengths, as well as the higher overall variability compared to the spectral signatures.

nizable with respect to to each other in comparison with those in Fig. 3(a), there is significant variation between the two. Safely assuming that the true reflectance of the panels remains unchanged, it is apparent that the incident radiation (atmospherically distorted sunlight) on the panels in Fig. 3(b) is far from uniform as a function of wavelength.

One may consider a block diagram as depicted in Fig. 4 as the end-to-end acquisition of a hyperspectral image. Based on this end to end process, after an image is acquired, it is common to back-out the signal attenuation of the earth’s atmosphere (manifest in the panel spectra shown in Fig. 3(b)) to obtain image spectra that better approximates the reflective properties of the actual scene (as shown in the panel

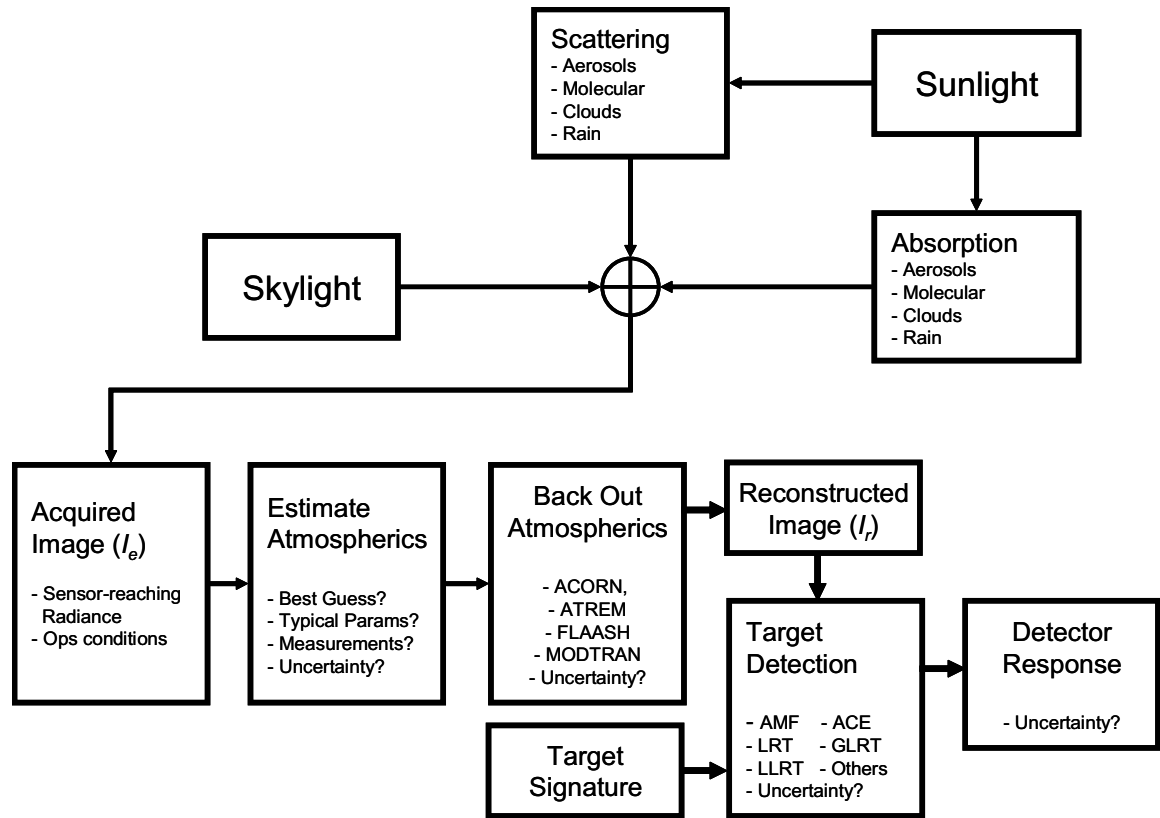


Figure 4: Acquisition through detector response flow. Uncertainty propagates through the process flow and culminates at the detector response. This uncertainty is a function of the uncertainty in the atmospheric parameter estimation, the uncertainty in the atmospheric compensation method, and the inherent uncertainty in the target detection algorithm due to its underlying assumptions.

spectra of Fig. 3(a)). This process, called *atmospheric correction*, is commonly done using a highly generalized set of atmospheric parameters. However, the problem with this generalization is that these parameters themselves vary with local conditions, and that this variation creates error in the atmospherically corrected estimate of the target reflective properties. While this error itself is inevitable given limited knowledge of the actual conditions, hyperspectral imagery (HSI) analysts presently have no estimates of what that error is most likely to be. Furthermore, a typical operational environment contains little *a priori* knowledge about the location in the image of specific targets or the specific atmospheric conditions under which the image is acquired. Based on work developed by atmospheric physicists, we incorporate distributions of atmospheric conditions in order to simulate HSI imagery under that distribution and understand how it affects the output of the target detection algorithm, as depicted in the lower right hand block of Fig. 4. Specifically, we develop a distribution of the error associated with the use of the AMF as a function of the distribution of atmospheric profiles as measured by radiosonde data collected at a real-world location.

### 1.3 Scope

Our intention is to limit discussion to that of the specific atmospheric correction methodologies as used by Raytheon's Advanced Responsive Tactically Effective Military Imaging Spectrometer (ARTEMIS) system: the Moderate Resolution Atmospheric Transmission Model (MODTRAN) as implemented in the Fast Line-of-sight Atmospheric Analysis of Spectral Hypercubes (FLAASH) and a specific target detection algorithm (the AMF). As part of the analysis, we define an upper bound to our system performance that assumes the ability to perfectly correct the atmospheric effects illustrated in Fig. 3. This serves as the "best case" performance base-line to which one may compare subsequent detector results.

## 1.4 *Research Question*

The previous sections lead to the following critical research question: “Can we characterize the detection error as a function of the distribution of atmospheric parameters?” Simulated imagery shows that variation in the atmospheric profile produces variation in the detection error as predicted by the L2 norm between the resulting target spectra and measured by both the Bhattacharyya coefficient between the resulting AMF output and the area under the curve (AUC) of the detection Receiver Operating Characteristic (ROC) curve [14].

## 1.5 *Overview*

The balance of the dissertation is organized as follows. Chapter II discusses the technical background to the research. It describes the mathematics behind the AMF, empirical line correction, and radiative transfer. It reviews the published literature on the various methods of atmospheric correction, including in-scene methods, statistical methods, and modeling methods (specifically MODTRAN). Chapter III provides an analysis of the AMF output based on the relative changes of the PDF across different atmospheric profiles, which gives way to the approach defined in this dissertation. It discusses the software applications we use and their purpose. It also describes the metrics we use to evaluate the AMF output. Chapter IV describes the design of the final experiment and results thereof. Chapter V summarizes the results and suggests directions for future research.

As described in detail in Section 3.4.3, we begin by creating a series of well-validated simulated hyperspectral images (HSI) of a suburban neighborhood in the vicinity of the main campus of the Rochester Institute of Technology. These images are simulated under a variety of atmospheric profiles obtained from an extensive database described in Section 3.4.1.

We then perform target detection using the AMF against known target spectra. As described in Chapter IV, we obtain the reflectance spectra of all pixels from the

image radiance spectra and then perform the detection in reflectance space. We use the application described in Section 3.4.2 for this purpose.

Finally, by studying the effect of the different atmospheric profiles on the ROC curves generated by the AMF, AUC's, and Bhattacharyya coefficients, we are able to measure the effects on target detection of the atmospheric variability.

## II. Background

Our work uses long-standing mathematical techniques for hyperspectral imagery (HSI) detection and atmospheric correction. These methods continue to be used in research today. This chapter covers the following topics in some detail in order for the reader to fully understand the research methodology: adaptive matched filter, empirical line correction, and radiative transfer.

### 2.1 Adaptive Matched Filter

As described by Manolakis and Shaw [34], the Adaptive Matched Filter (AMF) is a modified version of the log-likelihood ratio test (LLRT), where the LLRT is expressed as follows:

$$\begin{aligned} \ln \Lambda(X) &= \ln \frac{p_1(X)}{p_0(X)} \\ &= (\mu_0 - X)^T \cdot \Sigma_0^{-1} \cdot (\mu_0 - X) - (\mu_1 - X)^T \cdot \Sigma_1^{-1} \cdot (\mu_1 - X) \dots \\ &\quad + 0.5 \ln \det \Sigma_0 - 0.5 \ln \det \Sigma_1 \end{aligned} \quad (1)$$

The parameters  $\mu_1$  and  $\Sigma_1$  are the means vector and covariance matrix, respectively, of the PDF  $p_1(X)$  for the “target present” hypothesis  $H_1$ . Ideally, these parameters have been collected and stored in a spectral library. The parameters  $\mu_0$  and  $\Sigma_0$  are the mean and covariance of the background PDF  $p_0(X)$  under the “target absent” hypothesis  $H_0$ , and can be calculated directly from the image data. The theoretically appropriate threshold  $\gamma$  for this detector is

$$\gamma = + \ln \eta, \quad \eta = \frac{P_0(C_{10} - C_{00})}{P_1(C_{01} - C_{11})}, \quad (2)$$

where  $P_0$  and  $P_1$  are the prior probabilities of the hypotheses  $H_0$  and  $H_1$ , the  $C_{xx}$  variables are penalties defined in Table 1, and “det” is the matrix determinant.

Table 1: LLRT Cost Function Definitions

$C_{10}$	Cost of guessing $H_1$ when $H_0$ is true
$C_{00}$	Cost of guessing $H_0$ when $H_0$ is true
$C_{01}$	Cost of guessing $H_0$ when $H_1$ is true
$C_{11}$	Cost of guessing $H_1$ when $H_1$ is true

Consider an experiment where each frame contains about 140 target pixels against a total of 204,800 pixels. Assuming  $C_{10} - C_{00} = C_{01} - C_{11}$ , one could compute the ideal threshold as:

$$\ln \eta = \frac{P_0}{P_1} = \ln \frac{204800 - 140}{140} = 7.3. \quad (3)$$

It may be that we do not know the prior probabilities, in which case there are a number of approaches. We can assume equal priors and the previously defined costs, in which case  $\eta = 1$ . This can be a viable approach even when the assumptions are incorrect. In general, the value of finding a particular target rises inversely with its density, so the incorrect assumptions tend to cancel each other out.

A possible limitation of the LLRT Detector is that the target covariance matrix might not be known, or the target data may not have sufficient variation and/or samples to produce an invertible estimate of the covariance matrix. In this event, we can develop the AMF detector by making several assumptions on the LLRT [41]. First, we assume the target covariance matrix is equal to the background covariance matrix, i.e.  $\Sigma_1 = \Sigma_0 = \Sigma$ , and obtain:

$$\ln \Lambda(X) = \ln \frac{p_0(X)}{p_1(X)} = (\mu_1 - \mu_0)^T \cdot \Sigma^{-1} \cdot X, \quad (4)$$

where  $X$  is the data (each sample a row vector) and  $\mu_1$  and  $\mu_0$  are the means of the probability density functions (column vectors) for hypotheses  $H_1$  and  $H_0$ , respectively. Note that Eqn (4) is linear in  $X$  and therefore generates linear discriminant functions [24]. Second, we assume that the background mean,  $\mu_0 = 0$ , and that  $\mu_1$

is some multiple  $b$  of the spectral signature  $s$  in a library of target reflectance, i.e.  $\mu_1 = bs$ . We can obtain the maximum likelihood estimate of  $b$  as:

$$\hat{b}_{ML} = \arg \max_b p_1(X|bs, \Sigma) = (s^T \cdot \Sigma^{-1} \cdot s)^{-1} \quad (5)$$

Thus, if  $H_1$  is presence of a target and  $H_0$  is its absence,

$$\ln \Lambda(X) = \left( \frac{s}{s^T \cdot \Sigma^{-1} \cdot s} \right)^T \cdot \Sigma^{-1} \cdot X \quad (6)$$

becomes an assessment of the presence of a target with spectral signature  $s$  in the pixel represented by sample  $X$  [34].

Therefore, for some subset of features in  $s$  and  $X$ , we calculate the covariance matrix  $\Sigma$  of the training data  $X_{train}$  and then apply Eqn (6) to  $X_{test}$ , the testing data. Then,  $\ln \Lambda(X_{test})$  is compared to a threshold to classify the data as either belonging to the class of spectral signature  $s$  or not. By comparing these classifications to the pixel's known class membership, we determine a probability of detection ( $P_d$ ) and a probability of false alarm ( $P_{fa}$ ) for that threshold. We obtain the ROC curve for that class by varying the threshold from the maximum value of  $\ln \Lambda(X_{test})$  to its minimum value. In the ideal case, when  $X$  is equal to  $s$ ,  $\ln \Lambda(X) = 1$ .

Landgrebe [33] considers the issue of the optimum detection threshold for Eqn (4). Because the output of Eqn (4) is  $\chi^2$  distributed, we can calculate a threshold from the detection parameters and an arbitrary  $P_d$ . For instance, if we fix  $P_d = 0.95$ , then the threshold  $T_i$  for class  $i$  would be:

$$T_i = -4.744 + \ln P_i - 0.5 \cdot \ln \det \Sigma_i \quad (7)$$

There are other detectors one may consider [3] [40] [46], such as the adaptive cosine estimator (ACE) [34], the correlation coefficient, and the spectral correlation mapper [10]. However, we choose the AMF because of its popularity and performance.

## 2.2 A Survey of Atmospheric Correction

Research into atmospheric correction falls broadly into three categories: radiative transfer, mathematical models, and in-scene correction. Here we cover the general topic of atmospheric correction that falls under the three categories described in Section 2.3. All these methods described here and in Section 2.3 introduce uncertainty into the calculation of atmospheric effects; there is no method in which uncertainty is eliminated.

*2.2.1 Radiative Transfer.* After the atmosphere has done its work on the sun's radiation and the light has reflected from the target, we measure that light by acquiring an image with our hyperspectral camera in units of radiance. In the radiative transfer methodology, we must then make an estimate of the atmospheric parameters and then use these parameters to back out the effects of the illuminating source using mathematical models of atmospheric properties. We then reconstruct our image in terms of reflectance. It is on this reconstructed image that we perform target detection.

One example of applying radiative transfer methods to atmospheric correction is described in [18], in which Gao et al. seek to recover reflectances from NASA/JPL [10] AVIRIS data using atmospheric correction. Their method is well-suited to well-lit Lambertian targets imaged on clear days.

Of the approximately thirty gases present in the atmosphere, only seven affect the spectral signatures of transmitted radiation; of these, water vapor ( $H_2O$ ) is the most variable. These gases are non-uniformly distributed vertically from the earth's surface. The work in [18] considers the radiative transfer method of estimating atmospheric effects as implemented in the Satellite Signal in the Solar Spectrum (5S) code [18]. This method uses the total atmospheric transmittance in its calculation, which in turn uses the atmospheric reflectance (i.e., light that never reaches the target, but is reflected to the sensor). The authors in [18] point out that radiation is both scattered in different directions and absorbed by the molecules.

At the time of the paper's writing, Gao et al. [18] state that the standard atmospheric correction model, such as LOWTRAN, relied on assuming that the distribution of water vapor throughout a column of atmosphere is uniform. Gao et al. seek to undo this assumption by calculating the water vapor content from the 0.94 and  $1.14\mu m$  wavelengths and applying an absorption curve based on that content to the entire signature in the 0.4 to  $2.5\mu m$  region. They rely on two assumptions. First, that the relationship between wavelength and the reflectance at that wavelength at the water vapor absorption bands (here taken to be 1.38 and  $1.88\mu m$ ) is linear. Second, that the transmittance from 0.94 and  $1.14\mu m$  varies with water vapor.

In [19], Gao et al. develop an atmospheric correction algorithm for ocean scenes. In particular, they attempt to retrieve the "water leaving radiances," or the amount of the illumination that reflects toward the imager from below the surface of the water. Previous algorithms estimate the atmospheric aerosol content from portions of the spectrum (between 0.66 and  $0.87\mu m$ ) where the water leaving radiance is zero; however, suspended particles in turbid coastal waters often produce non-zero values for these radiances even within this spectral range. Gao et al. employ a method of estimating atmospheric conditions using spectral matching with data generated by a radiative transfer algorithm. This is necessary for obtaining accurate water-leaving reflectances, i.e. ocean color from remotely sensed data.

Gao et al. [19] review the radiative transfer algorithm for expressing the observed radiance of the sensor in terms of three factors: the atmospheric radiance, i.e. illumination reflected by the atmosphere before ever reaching the surface; the radiance reflected from the surface; and the radiance reflected from below the surface. It is this last radiance that is of particular interest to ocean scientists in determining ocean color. They solve this relationship for the ocean leaving reflectance in terms of the atmospheric transmittances, the atmosphere and surface reflectances.

Gao et al. [19] use radiative transfer code published by Ahmad and Fraser in 1982 [4] to develop a lookup table that they use for the spectral matching. They

assume a U.S. Standard Model Atmosphere for the temperature and pressure profile. They used the code to generate estimates of the atmospheric reflectances and transmittances for 20 aerosol models, various scene geometries, and 10 optical depths for 14 wavelengths.

Scene geometry is recovered easily enough from the image time-of-day and the known imager position. Transmittances are calculated for a range of water vapor amounts and stored in a lookup table. The overall scene reflectance (including atmospheric effects) is calculated based on the known solar spectrum. Gao et al. estimate true water vapor content from the 3-channel ratioing technique described in [18], and match it to an atmospheric transmittance in the lookup table. The method then removes the atmospheric transmittance effect by dividing the observed reflectance by the transmittance. This ratio is then matched across the 14 values in the lookup table generated by the radiative transfer code, and the matching parameters are then plugged into the formula for calculating the water leaving reflectance.

The spectral matching method employed by Gao, et al. is very similar in overall intent to the method employed by Healy and Slater in [25] (described in Section 2.2.2).

*2.2.2 Mathematical Methods.* The second general approach to atmospheric correction researched is to develop high-dimensional manifolds over a range of atmospheric parameters for a particular spectral signature or set of signatures and “match” a candidate radiance spectrum to one of those manifolds.

In [5], Borel et al. attempt to obtain atmospheric parameters, specifically temperature and transmittance, by varying atmospheric quantities over a range of estimates and selecting the parameters that provide the smoothest estimate of the emissivity. Emissivity is the ratio of the radiance of a target pixel to a “black body” pixel at the same temperature. A black body is a target with zero reflectance and transmittance, i.e. it absorbs all radiation incident on it [12]. As such, its emissivity is therefore one, emitting thermal energy in units of radiance ( $W/m^2/str/m$ ) according to Planck’s equation:

$$S(\lambda) = \frac{2hc^2}{\lambda^5} \frac{1}{e^{ch/\lambda k_B T} - 1}, \quad (8)$$

where  $c$  is the speed of light ( $3 \times 10^8 m/s$ ),  $h$  is Planck's constant ( $6.63 \times 10^{-34} J \cdot s$ ),  $k_B$  is Boltzmann's constant ( $1.38 \times 10^{-23} J/^\circ K$ ),  $T$  is the substance's temperature in Kelvin ( $K$ ), and  $\lambda$  is the wavelength in meters ( $m$ ). Other targets, called "gray bodies" have emissivities less than one [12].

As a measure of smoothness, Borel et al. [5] choose the autocorrelation across a variable window. They then sum and normalize those autocorrelations to obtain an average de-correlation wavenumber as a function of the atmospheric transmittance. By applying a "boxcar window" smoothing function to the emissivity and then plotting the de-correlation wavenumbers against the width of this window, they determine that a resolution of  $20cm^{-1}$  is necessary to distinguish atmospheric affects, which we wish to remove, from emissivity features, which we wish to keep.

The method they use begins by picking a typical emissivity of 0.95 and a "standard atmosphere" transmittance. These values are applied to a radiative transfer equation for the radiance at the ground, from which a surface temperature is calculated using the Planck function. The radiative transfer equation is then solved for a better estimate of the emissivity under the estimated conditions. When this optimization process is complete, they compare the smoothness of the resulting curves as described above. Their approach results in true surface temperature estimates of ground objects within  $0.021 \text{ deg } K$ .

In [25], Healy and Slater propose a method of atmospheric correction that is independent of illumination, atmospheric conditions, and the angle at which the image is acquired. It does this by deriving and applying a least-squares estimate of the basis for the vector subspace in which the radiance spectrum for a particular material is thought to reside, calculating maximum-likelihood estimates of the coefficients of those basis vectors for a particular target given a set of possible class memberships, and then applying a likelihood ratio test to determine the class membership. If

classification can be performed without an estimate of the atmospheric conditions, then target detection methodologies are freed from the errors associated with such estimates. The only error would be any persistent bias in MODTRAN's estimate of a material's sensor radiance under any atmospheric condition.

The paper documents an experiment in which an image taken with the HYDICE sensor of a green cloth in direct sunlight is compared to an image of the same green cloth illuminated only by skylight that shines through, or reflects from, ambient tree cover. According to [25], even the normalized radiances of these two images show differences that can make detection difficult.

Healy and Slater [25] present a model of the received radiance as the sum of reflected sunlight, reflected skylight, and the "path radiance," or the illumination that is reflected to the sensor by the atmosphere before ever reaching the image target. The first two of these factors is dependent on the reflectance of the material under consideration.

They use MODTRAN v3.5 and sets of values for ten atmospheric and scene-geometry parameters to assemble a set of 17,920 possible illumination vectors with which to multiply the material reflectance. These illumination functions are then approximated by a linear combination of a much smaller number (3 - 12) of basis vectors using the least-squares method. The paper estimates that the error associated by this linear approximation rapidly drops as the number of basis vectors approaches nine. Healy and Slater infer from this that the spectral-radiance vectors of the reflecting material, each with 210 dimensions (frequencies) actually lie in a low-dimensional subspace. In other words, for a particular material imaged at  $W$  frequencies, not all possible radiance vectors are equally likely, regardless of the illumination and atmospheric conditions, and that the likely radiance vectors have a mathematical relationship between each other that can be defined as a linear combination of  $N$  basis vectors where  $N \ll W$ .

The possible sensor radiances for a given material can be thought to lie in an  $N$  dimensional subspace of  $\mathbb{R}^W$ . Each target material occupies a different subspace, however, and classification becomes not a matter of determining the true reflectance vector of a given target, but rather applying an LRT to a particular set of basis vectors defining the target's true subspace. This can be accomplished without reference to any of the illumination or atmospheric conditions. They first attempted to discriminate among 100 different materials, applying to each of the materials the 17920 illumination vectors generated by MODTRAN. They did so successfully 97.9% of the time. Furthermore, they compared the performance of their invariant algorithm with the spectral angle mapper (SAM) algorithm for HYDICE images of several shades of green fabric in a mixed-vegetation scene under different lighting conditions. The SAM algorithm, which evaluates the difference between the reference vector  $L_\gamma$  and the sensor radiance  $L'(x, y)$  as

$$\arccos \left( \frac{L_\gamma \cdot L'(x, y)}{\|L_\gamma\| \cdot \|L'(x, y)\|} \right) \quad (9)$$

does not depend for its effectiveness on any multiplicative factor that might arise from lighting conditions. In this case, the SAM reference vectors were determined in-scene, while the invariant algorithm relied only on the MODTRAN estimates. While the SAM performed better in direct sunlight (in other words, when the reference spectra and the target spectra were the result of identical lighting conditions), the invariant method performed better in the shade. While the SAM method appears to have degraded performance in the shade, the paper does not provide the ROC curve beyond a probability of false alarm ( $P_{fa}$ ) of  $5 \times 10^{-4}$ , instead showing the results of the detection threshold overlaid on a photograph of the scene.

To further evaluate the invariant method, it would be worthwhile to compare the results of the invariant method against other detection algorithms, such as the LLRT, the AMF and the ACE. These other methods rely on atmospheric correction, of course, and if there are in-scene references then MODTRAN should be able to

generate some parameter estimation. Our expectation is that the invariant method is superior in circumstances in which no in-scene references are available. The method described does not appear to lend itself very easily to dimensionality reduction. Since the data must be compared to some subspace that itself represents a feature transformation/reduction, but the transformation is different for every different material, then we would have to keep all the data to maintain flexibility.

Suen et al. [43] expand on the work by Healy and Slater [25] by applying the invariant method to discrimination among 237 materials from the United States Geological Survey spectral library. The primary variable under consideration was off-nadir viewing: the elevation of the solar illumination, the elevation of the sensor, and the azimuth difference between the two. The experiment again used MODTRAN to apply the solar illumination under 48 sets of atmospheric conditions and 234 solar/sensor configurations to the spectral reflectances of the 237 materials. Selecting invariant subspaces of 9 dimensions from the 210-dimension HYDICE spectral signatures, Suen et al. first used the invariant method to classify the 237 materials under these different conditions with perfect accuracy. They then simulated typical additive HYDICE sensor noise after the basis vectors had been calculated, where the magnitude of the noise variance was a multiplier of the intensity. In all configurations, the error was less than 1%.

Suen et al. applied their method to HYDICE images with synthesized off-nadir viewing angles. They used the empirical line correction method to estimate the reflectance of each pixel in the image; this data was then fed to MODTRAN to estimate the sensor radiance for various viewing angles. (No detail is provided on which set of atmospheric parameters were used in MODTRAN.) Seeking targets composed of green and tan cloth, again the method detected all pixels of all targets before any false alarms were generated. They conclude that real off-nadir data would be useful to validate their estimates.

*2.2.3 In-Scene Correction.* In [6], Borel expands on earlier work in choosing among parameter sets based on their calculated smoothness. He introduces a method they call In Scene Atmospheric Correction (ISAC), in which a wavelength with low path radiance and high atmospheric transmission is selected. As before, the assumption that a constant emissivity of 0.95 is used. Based on this assumption, a surface temperature is computed using the inverse Planck function. At a second wavelength, the radiance is measured. These two values are plotted against each other for each pixel. The highest values of the measured radiance for each calculated radiance correspond to those pixels with the highest blackbody properties. These points are linear. If we draw a line through those points at the top of each bin, we discover that the slope of that line is proportional to the atmospheric transmission and the intercept is proportional to the path radiance. The emissivity spectrum can then be calculated from these values. This method, however, only works if the scene has a wide variety of color temperatures represented, and sufficient blackbody pixels.

Borel also reviews the emissivity selection criterion of smoothness. They estimate the ground temperature of the target and pick a wavelength with high atmospheric transmittance. They calculated emissivity spectra for a range of temperatures around this estimate, and pick the smoothest one, inferring that its temperature is the most correct. However, they realize that there are, in fact, multiple atmospheres for which a particular spectrum might be sufficiently smooth, so the initial parameter estimates must be accurate in order to get an accurate temperature calculation.

To improve this estimate, Borel substitutes the one-layer atmospheric model used in [5] with estimates calculated by MODTRAN. Borel uses the ISAC method to find a number of likely atmospheric profiles, and these are tested against each other to discover which atmosphere generates the smoothest emissivity.

In [22], Gruninger, et al. suggest that the registration of thermal infrared (TIR) and visible and shortwave infrared (VIS-SWIR) images can reduce the image ambiguities in TIR data. They begin with a discussion of several atmospheric correction

measures and their limitations. For example, ISAC [29] requires the presence of black-body targets in scene over a range of temperatures in order to get good slope-intercept calculations, but these are not always present. Borel's smoothness evaluations [7] require (evidently) resolutions that are not always available, especially in TIR with its longer wavelengths. Canonical correlation analysis (CCA), which "correlates a basis of atmospheric transmittance, path radiance and downwelling radiance to the scene radiances to select an atmosphere" [22] generates different sets of coefficients for each for each of these quantities, yielding inconsistent atmospheric profile predictions. An oblique projection technique called "OPRA" uses MODTRAN to create "two oblique subspace projections to estimate the atmospheric path radiance and transmittance separately" [22], but this yields different atmospheric profiles for different regions of the subspace. Healy and Slater's method (discussed) provides no atmospheric information.

Gruninger, et al. propose a modification to Healy and Slater's method that is different in at least two respects. First, it appears to estimate reflectances as a linear combination of a set of in-scene basis spectra, and that this estimation occurs simultaneously with the use of bases to describe atmospheric conditions. Second, they calculate the radiance basis from a simple equation rather than using MODTRAN to generate the results of all possible parameter combinations.

After a discussion of the effect of emissivity on radiance, Gruninger et al. propose what they call a "triple expansion" wherein they create a basis for temperature, emissivities, and radiance. The radiance basis is calculated from a range of values for atmospheric transmittance, and upwelling and downwelling radiances. A given radiance can be expressed as a weighted sum of these basis vectors, the coefficients of which break out the atmospheric parameters; however, this equation is underdetermined.

The paper then applies singular value decomposition to the radiance basis; the left singular vectors of this operation, in turn, form the basis spectra from which a new

set of coefficients is determined using the least squares method. This new equation is “fully determined,” and the resulting coefficients are then back-transformed to recover the first set of coefficients. These coefficients are used to find the atmospheric and material quantities.

The method is tested on both synthesized and experimental data. An “end member” code called sequential maximum angle convex cone (SMACC) was used to obtain the basis set for the atmospheric parameters (transmittance, upwelling and downwelling radiance).

Gruninger et al. provide graphs showing the true values for transmittance, upwelling radiance, downwelling flux, and emissivity, all as functions of wavelength, plotted against the values estimated by their method. While the spectra are broadly similar, they appear to me to have substantial differences. The paper does not give spectra of estimated and true reflectance signatures for the particular materials; however, we know from experience that the estimates must be very accurate for some of the detection methods we have examined. If what they provide is representative, then the method is not especially superior as a way of estimating reflectance.

*2.2.4 Conclusion.* As the research cited above indicates, the methods of atmospheric correction in active use today rely on either assumptions about the atmospheric composition over the target or removing the need for such assumptions by the use of in-scene target samples or statistical methods.

One of the few studies that specifically examines the effect of atmospheric variability to target detection is documented in [30]. Here Kacenjar, et al. study atmospheric variability and its effect on detection of igneous rock classes on the Hawaiian land mass.

Kacenjar, et al. estimated the atmospheric variability of Hawaii’s climate from the National Oceanographic and Atmospheric Administration (NOAA) Forecast System’s Laboratory (FSL) [38] database of daily radiosonde collections. They then used MODTRAN to simulate the effect of these different profiles on igneous rock reflectance

spectra from the Advanced Spaceborne Thermal Emission and Reflection Radiometer (ASTER) [37] spectral library published by National Air and Space Administration's (NASA) Jet Propulsion Laboratory (JPL).

Kacenjjar, et al. then use the Spectral Angle Mapper (SAM) detection algorithm [34] to calculate the spectral angle between the mean spectrum of the picrite igneous rock class with the radiosonde-adjusted spectra for both picrite and five other igneous rock classes. By graphing the daily values of these angles over the course of a year, they show that, first, there is little variation in the angles over the year they examined, and second, that the angle values are well-separated, with the same-class comparison consistently showing the smallest difference.

Significantly, Kacenjjar, et al. only compare spectral angles among a discrete set of rock classes. They do not perform target detection against a realistic background. Further, the climate associated with their radiosonde data is famously invariant. For these reasons, there is room for further investigation of atmospheric variation effects on target detection under operationally relevant conditions.

### 2.3 Empirical Line Correction (An In-scene Methodology)

One way of correcting for atmospheric distortion is called empirical line correction (ELC). ELC picks at least two field samples  $\bar{x}_1$  and  $\bar{x}_2$ , where  $\bar{x}_i = [x_{i,1} \ x_{i,2} \ \dots \ x_{i,N}]$  with  $N$  spectral features whose class memberships are already known and for which we possess spectral signatures  $\bar{s}_1$  and  $\bar{s}_2$  in our spectral library. Alternatively, a "dark" and a "light" Lambertian surfaces can be matched to uniform reflectance spectra of zero and one, respectively. However, such surfaces must be chosen very carefully to prevent errors. Once the surfaces are chosen, we can plot a linear regression for each feature  $j = 1 \dots N$  matching the image radiances to

$$w = \frac{\phi^T \cdot S}{\phi^T \cdot \phi}, \quad \phi = \begin{bmatrix} 1 & x_{1,j} \\ 1 & x_{2,j} \end{bmatrix}, \quad S = \begin{bmatrix} s_{1,j} \\ s_{2,j} \end{bmatrix} \quad (10)$$

where  $w$  is a vector containing the regression weights. We then use these weights to regress the entire data set of  $M$  pixels  $X$  into a transformed data set  $\tilde{X}$  more closely matching the various classes' ideal reflectance values for each feature  $j$ , as:

$$\tilde{X} = X \cdot w, \quad X = \begin{bmatrix} 1 & x_{1,j} \\ 1 & x_{2,j} \\ \vdots & \vdots \\ 1 & x_{M,j} \end{bmatrix} \quad (11)$$

Conventionally, ELC is a simple way of translating the radiance values in an image to the reflectance values as in the spectral library. Given uniform illumination across an image, the relationship between radiance and reflectance is largely linear, and is therefore a candidate for linear regression. However, ELC requires prior knowledge of two points in the image for which we know the actual reflectance; all other points can then be regressed to the line between them.

Consider Fig. 5, a plot of the mean radiance of the four target panels as they appear in the image versus their known reflectance from the spectral library. This plot is of the values for the single dimension corresponding to a wavelength of  $522nm$ , broadly representative of the other dimensions. We see the linear relationship between the points, as illustrated by the dotted line drawn between the points representing the black and silver panels. Again, this assumes that we have in advance one sample from each of two known classes, and that the illumination conditions across all targets in the image are uniform. Even then, we can observe from the distance between the point representing the green panel and the regression line that the method is not without error.

We now consider an alternative to this prior knowledge. The black dotted line in Fig. 5 is the regression line between two points mapping the dimmest radiance in the frame to a reflectance of zero and the brightest radiance to a reflectance of one. As we can see, this is a poor estimate of the relationship among the targets, which suggests

that the relationship may not be linear. The normalized mean-squared error of the four target classes at this wavelength is 40% for this light-dark regression, compared to 0.3% for the black-silver regression. A close inspection of the image shows that there are a handful of pixels that are disproportionately bright, and in fact these pixels have a radiance of around  $33DN$ , compared to a radiance of  $8DN$  for the silver panel. These pixels represent highly specular (in contrast to our Lambertian assumption) reflection from some shiny reflective object in the scene. Unfortunately, we cannot rule out *a priori* the possibility of such anomalous reflections in our scenes.

Consider Fig. 6, where we present the first two principal components of all pixels in the image, plotted by their magnitude along the  $x$  and  $y$  axes, and color-coded by

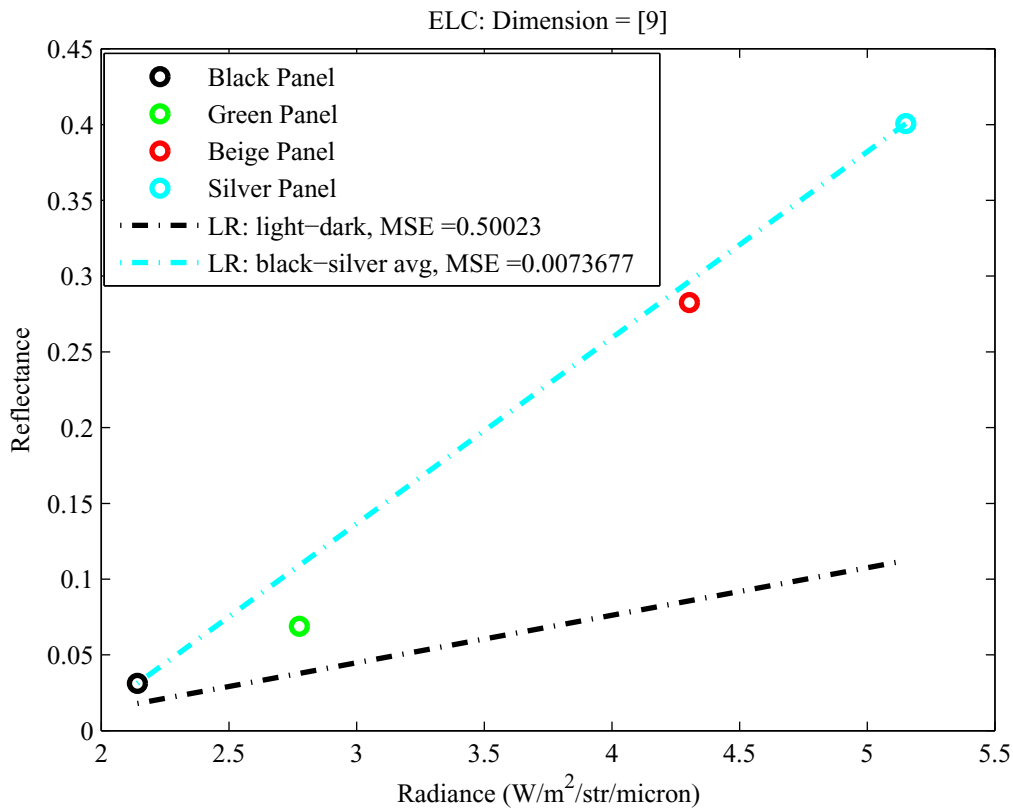


Figure 5: Plot of the laboratory-measured reflectance vs. image radiance for dimension 9 ( $\lambda = 522nm$ ) of four colored panels and the normalized mean-squared error for both the regression between the black and silver pixels and the regression between the lightest and darkest pixels. Note that the “Green” pixel visibly departs from the black-silver regression model.

their class memberships. These pixels have been “atmospherically corrected” to their reflectances as estimated by the ELC method.

Overlaying these pixels are larger markers corresponding to the expected output of a log-likelihood ratio test (LLRT) detector for pixels of that spectral value given the true mean and variance of the target panels as measured by a field spectrometer. As we can see, for the black and silver panels, the peak return of the detector corresponds to the approximate modal pixel value. This is as expected, since the regression mapped the mean pixels directly on to their known library reflectances. However, we can also see considerable error associated with the values for the green panel and especially the

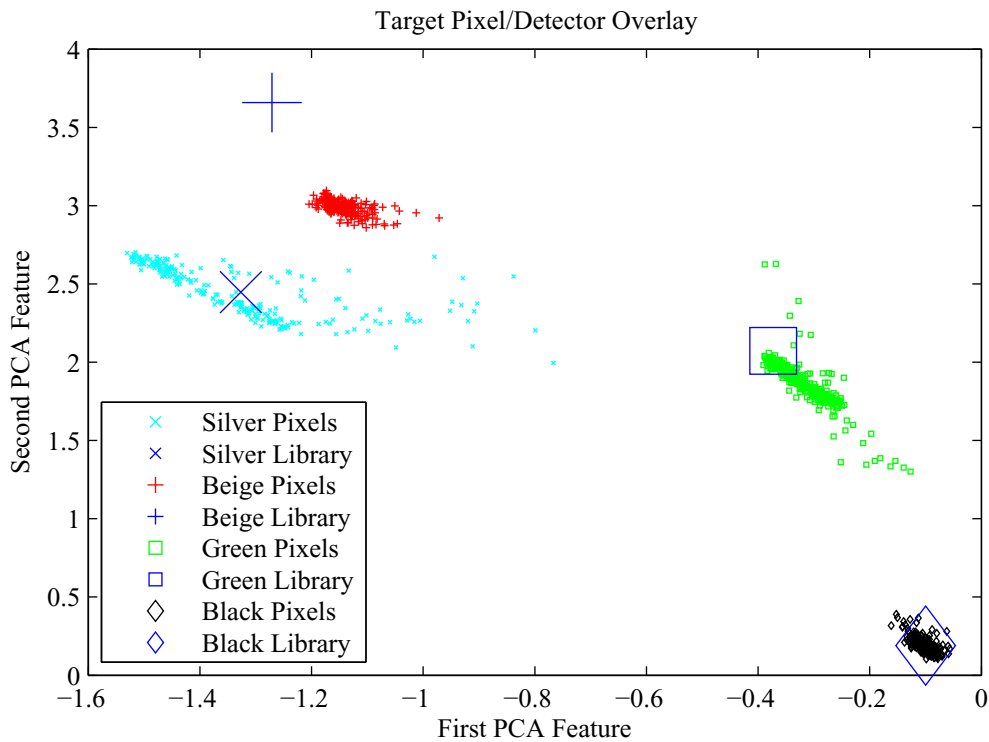


Figure 6: Plot of the first two principal components for four colored panels as corrected by the ELC method, overlaid with the same features from the spectral library signatures. The ELC method anchored the regression between the “black” target and the “silver” (represented by cyan) target; as expected, the signatures precisely match the pixels for these panels. Note, however, the error associated with the green and beige pixels and the normalized mean-squared error for both the green and beige (represented by red) pixels.

beige panel. Clearly, even the application of a highly optimized ELC method is prone to measurable error in correcting radiances to reflectances for targets in which we have no known in-scene examples. This illustrates the effect of atmospheric misestimation and motivates the need to evaluate the effect of this error on spectral target detectors.

## 2.4 Radiative Transfer

The fundamentals of radiative transfer are detailed in multiple references. The presentation here follows from Petty in [39].

As the electrons of an atom change energy levels as a result of collisions with other atoms, the substance of which it is a part emits photons of radiation whose spectral signature is dependent on the temperature of that substance. The spectral signature  $S(\lambda)$  in units of radiance ( $W/m^2/str/m$ ) is given by Planck's formula as:

$$S(\lambda) = \frac{2hc^2}{\lambda^5} \frac{1}{e^{ch/\lambda kT} - 1}, \quad (12)$$

where  $c$  is the speed of light ( $3 \times 10^8 m/s$ ),  $h$  is Planck's constant ( $6.63 \times 10^{-34} J \cdot s$ ),  $k$  is Boltzmann's constant ( $1.38 \times 10^{-23} J/^\circ K$ ),  $T$  is the substance's temperature in Kelvin ( $K$ ), and  $\lambda$  is the wavelength in meters ( $m$ ). Planck's formula applies to any substance with a uniform emissivity of one.

Most objects, however, do not have emissivities uniformly equal to one. As a function of wavelength, they emit only some of the incident radiation. The rest of the radiation is reflected at its incident frequency. Under thermodynamic equilibrium, the relationship is therefore  $\epsilon(\lambda) + r(\lambda) = 1$ , where  $\epsilon$  is the *emissivity* (the percentage of  $S$  that is emitted at a given wavelength) and  $r$  is the *reflectance* (the percentage of incident radiation that is reflected at a given wavelength) [12].

While the surface of the earth's sun can rightly be described as having uniform emissivity (known as a *blackbody*), the molecules of the earth's atmosphere reflect (scatter) and emit (absorb) the sun's radiation on its way to targets on the earth's surface, and also absorb and emit radiation along the path from the target to the

sensor. The effort to quantify these affects is known as *radiative transfer*. This process is described in a number of references; the following explanation comes from [16].

The basic equation for the propagation of radiation through the atmosphere is Beer's Law:

$$I_{\lambda}(s_2) = I_{\lambda}(s_1) \exp(-\tau(s_1, s_2)), \quad (13)$$

where  $I$  is in units of irradiance ( $Watts/m^2$ ),  $s_1$  is the height at the top of the atmosphere,  $s_2$  is the height of the surface target, and  $\tau$  is the *optical depth*. The optical depth is defined as:

$$\tau(s_1, s_2) = \int_{s_1}^{s_2} \beta_e(s) ds, \quad \beta_e = \beta_a + \beta_s \quad (14)$$

where  $\beta_e$  is the *extinction coefficient*,  $\beta_a$  is the *absorption coefficient*, and  $\beta_s$  is the *scattering coefficient*.

The absorption coefficient is determined from the equation

$$\beta_s = \frac{4\pi n_i \lambda}{3} \quad (15)$$

where  $n_i$  is the imaginary component of the index of refraction (determined experimentally and stored in the HITRAN database) and  $\lambda$  is the wavelength of the incident radiation.

The scattering coefficient in the visible and ultraviolet wavelengths comes from Rayleigh scattering from the equation

$$\beta_s = f \frac{32\pi^3 W + m\rho}{3\rho_0^2 N_A \lambda^4} (n_0 - 1)^2 \quad (16)$$

where  $W_m$  is the molecular weight of dry air ( $28.966kg/kmol$ ),  $n_0 = 1.0003$  is the real index of refraction for dry air at sea level,  $\rho$  is atmospheric density,  $\rho_0$  is the density

of air at sea level,  $N_A$  is Avogadro's number ( $6.02210^{23}/mol$ ) [32], and  $f = 1.061$  corrects for anisotropic properties of air molecules.

This work considers humidity variation only in the non-aerosol case, and thus concerns itself with the effect of molecular scattering. However, as recommended in Chapter V, future work should consider the effect of aerosols and thus the effect that larger particles have on atmospheric extinction.

The extinction coefficient is related to the *extinction cross-section*  $\sigma_e$  by

$$\beta_e = \sigma_e N, \quad (17)$$

where  $N$  is the number of microscopic particles in a unit volume. (The term  $\beta_e$  can also be calculated from the mass extinction coefficient  $k_a$  and the atmospheric density  $\rho$ , which is an exponential function of height.) The particles are normally distributed by size as measured by radius  $r$ , with a median radius  $r_m$  and a standard deviation  $\sigma$ . (Do not confuse this standard deviation  $\sigma$  with the extinction cross-section  $\sigma_e$ .) Thus:

$$\frac{dN(r)}{d(\log r)} = \frac{N}{(2\pi)^{1/2} \log(\sigma)} \exp \left[ -\frac{(\log r - \log r_m)^2}{2(\log \sigma)^2} \right] \quad (18)$$

We can relate the extinction cross-section  $\sigma_e$  to the *extinction efficiency*  $Q_e(m, \lambda, r)$  by

$$\sigma_e(\lambda) = \int_1^2 Q_e(m, \lambda, r) \pi r^2 \frac{dN(r)}{r \ln 10 d(\log r)} dr, \quad (19)$$

where  $m$  is the mass per particle.

The extinction efficiency,  $Q_e$ , is a quantity which depends on *absorption*, a measure of the percentage of the energy absorbed by the atmosphere, and *scattering*, a measure of the percentage that is reflected away from the target, including back into the sensor.

The relative humidity causes the aerosol particles to grow in size. There are several methods for calculating the humidity-specific mean radius and standard deviation of the particle size, as in [11]. This growth is reflected in Eqn (20). The computer program known as the Laser Environmental Effects Distribution Reference (LEEDR) [15] first calculates the number density  $N$  using the dry aerosol mean radius and standard deviation. This number is then used to calculate the humidity altered radius value from Eqn (18) as:

$$\log r(a_w) = \pm \left[ -\ln(ND\sqrt{2\pi}\log\sigma)2(\log\sigma)^2 \right]^{1/2} + \log r_m, \quad (20)$$

where  $ND = dN/d(\log r)$ . The relative humidity not only changes the radius of the aerosol particles, it also changes the index of refraction of the particles:

$$n = n_w + (n_o - n_w) \left( \frac{r_o}{r(a_w)} \right)^3, \quad (21)$$

where  $n$  is the complex refractive index for liquid water,  $n_0$  is the refractive index for the dry particles,  $r_o$  is the radius of the dry particles and  $r(a_w)$  is the radius of the particle at the given relative humidity as described in Eqn (20).

The calculation of the extinction efficiency is complex and relies on many factors. Wiscombe [47] describes an efficient computation method for this value that relies on the refractive index of the aerosols.

There are several ways in which atmospheric variables influence the effect that humidity has on atmospheric transmission. Of these, the most significant are pressure broadening, doppler broadening, and the density effect.

*2.4.1 Pressure Broadening.* In the relatively dense atmosphere close to the earth's surface, the frequent molecular collisions change both the emission and absorption frequencies of the photons. At the molecular level, absorption occurs at very specific frequencies, called *lines*, depending on the molecule type. However,

the effect of these collisions is to “broaden” these lines into distributions. Pressure broadening is described as:

$$\alpha_L = \alpha_0 \left( \frac{p}{p_0} \right) \left( \frac{T_0}{T} \right)^n,$$

where  $p$  is pressure,  $T$  is temperature, and  $n$  is an empirically determined constant.

The  $\alpha_L$  term, in turn, helps determine the shape of the absorption distribution as a function of frequency. This shape is known as the *Lorentz line shape* and is defined as

$$f(\nu - \nu_0) = \frac{\alpha_L}{\pi [(\nu - \nu_0)^2 + \alpha_L^2]},$$

where  $\nu_0$  is the discrete absorption line frequency and  $\nu$  is the frequency of the radiation.

The absorption cross-section per unit mass,  $\sigma_\nu$ , is calculated as

$$\sigma_\nu = S \cdot f(\nu - \nu_0), \quad (22)$$

where  $S$  is an empirically determined constant known as the *line strength*.

*2.4.2 Doppler Broadening.* At higher altitudes, collisions are infrequent; however, the relative motion of the atmospheric particles induce doppler shifts in the frequencies of the absorbed and emitted radiation. These doppler shifts also have the effect of broadening the distribution of the absorption lines. Because the motion of atmospheric particles is distributed, on average, in well-defined ways, we can eliminate the need for any specific knowledge of the particle velocities and describe the line shape equation for doppler broadening as:

$$f_D(\nu - \nu_0) = \frac{1}{\alpha_D \sqrt{\pi}} \exp \left[ -\frac{(\nu - \nu_0)^2}{\alpha_D^2} \right],$$

$$\alpha_D = \nu_0 \sqrt{\frac{2k_B T}{mc^2}},$$

where  $k_B$  is the Boltzmann constant. The line shape affects the calculation of the absorption cross-section as in Eqn (22).

*2.4.3 Density Effect.* Independent of any particular spectral line, the atmosphere attenuates all radiation passing through it as a function of the distance through which the radiation must travel. This is known as the *density effect*. We can solve for the transmittance  $t$ , or the ratio of the radiation reaching the target to the radiation incident on the top of the atmosphere, as a function of the target altitude  $z$ :

$$t(z) = \exp \left[ -\frac{k_a w_1 \rho_0 H}{\mu} \exp\left(-\frac{z}{H}\right) \right], \quad (23)$$

where  $w_1$  is the constituent mixing ratio,  $k_a$  is the mass absorption coefficient,  $\rho_0$  is the maximum density at sea level, and  $H$  is the scale height (around  $8km$ , the altitude at which the density is  $e^{-1} = 36\%$  of its value at sea level).

### III. Methodology

The objective of this research is to measure the effects of the variation of atmospheric composition, specifically the variation of atmospheric water vapor and temperature, on the detection of known signatures against a realistic background using the adaptive matched filter (AMF). To that end, our methodology models the imaging conditions and measures how much those conditions are different between profiles under consideration. Our methodology employs several applications that will simulate these effects, including simulated imagery and radiative transfer, with which we use radiosonde data collected at the target location. We deploy a method of target detection: here, the AMF, but it could be the adaptive cosine estimator (ACE), the log-likelihood estimator (LLRT), or the generalized likelihood ratio test (GRLT), for example. We evaluate the results of that detection using several metrics, including the receiver operating characteristic (ROC) curve and the area under the ROC (AUC). This process allows us to observe and measure the effect on target detection of whatever changes we make to the atmospheric profile and identifies the optimum atmospheric assumptions to make for target detection, given uncertainty about the true parameter values.

#### 3.1 *Distances Between Atmospheres*

The process developed in this research for assessing the error of atmospheric on the AMF output considers the characterization of atmospheric distance: how should the changes in relative humidity between atmospheric profiles be measured? It is currently unknown what the differences between atmospheric profiles really mean and how two distances with the same numerical value may affect the estimated reflectance of a hyperspectral signature. That is to say, different pairs of atmospheric profiles with the same measured distance between them may not have the same effect on the error in their target signature, and therefore the relationship is likely one-to-many and not necessarily one-to-one. As such, one must carefully choose how the input error (input being the atmospheric profile) is represented.

There are two general approaches to defining a distance between atmospheres. A first approach is to measure the distance between two solar irradiance curves defined by a blackbody radiator (the sun) transmitting through an atmospheric profile. A second approach is to consider the difference between the profiles themselves. How are atmospheric profiles characterized? The most significant and widely recognized approach is to characterize the atmosphere by the atmospheric water vapor content. Several measures of water vapor content exist: absolute humidity, water vapor mixing ratio, relative humidity, and others.

*3.1.1 Water Vapor Relationships.* The fundamental measured quantity of atmospheric water vapor content is the *dew-point temperature* ( $T_{DP}$ ): the temperature to which a given parcel of air must be cooled at constant pressure for it to reach saturation. From  $T_{DP}$ , we can calculate the *vapor pressure* ( $e_s$ ) – the partial pressure contribution of water vapor in a volume or parcel of air, measured in hectopascals ( $hPa$ ) – as:

$$e_s(T_{DP}[^{\circ}C]) = 6.122 \exp \left[ \frac{17.67 \cdot T_{DP}}{T_{DP} + 243.5} \right]. \quad (24)$$

The vapor pressure can then be used to calculate both the *mixing ratio* ( $w$ ) – the mass of water vapor per unit mass of dry air in a given parcel – and the *specific humidity* ( $q$ ) – the mass of water vapor per unit mass of the moist air parcel – using the following two closely-related formulas:

$$w = \epsilon \frac{e_s}{P - e_s}, \quad (25)$$

$$q = \epsilon \frac{e_s}{P - (1 - \epsilon)e_s}, \quad (26)$$

where  $P$  is the air pressure in  $hPa$  and  $\epsilon = 0.622$  is the ratio of masses for equal quantities of water vapor and dry air (note that since  $\epsilon < 1$ , water vapor is less dense

than dry air). The specific humidity can be used to calculate the *virtual temperature* ( $T_v$ ) – the temperature to which a parcel of dry air must be heated for it to have the same density as moist air at the same pressure – as:

$$T_v = T \left( \frac{1 + \frac{w}{\epsilon}}{1 + w} \right) \approx T(1 + 0.6w), \quad (27)$$

where  $T$  is the temperature of the moist air parcel. The *air density* ( $\rho$ ) can then be calculated:

$$\rho = \frac{P}{R_d T_v}, \quad (28)$$

where  $R_d = 287 \text{ J/kg/}^\circ\text{K}$ ,  $P$  is in  $\text{N/m}^2$  or pascals ( $\text{Pa}$ ), and  $T_v$  is in  $^\circ\text{K}$ . We can use the air density to find the *vapor density* ( $\rho_v$ ), also known as the *absolute humidity* in  $\text{kg/m}^3$ :

$$\rho_v = \rho q. \quad (29)$$

The transmittance  $t(z)$ , or the ratio of the radiation reaching the target to the radiation incident on the top of the atmosphere as a function of the target altitude  $z$ , depends on both the mixing ratio  $w$  and the density  $\rho$  as follows:

$$t(z) = \exp \left[ -\frac{k_a w \rho H}{\mu} \right], \quad (30)$$

where  $k_a$  is the mass absorption coefficient and  $\mu$  is the cosine of the zenith angle [39].

We observe from these equations that atmospheric transmission depends on both density and pressure; that these are related to each other by dew-point temperature, atmospheric temperature, and pressure; and that they determine the absolute humidity. We also observe from our meteorological measurements (described in detail

in Section 3.4.1) that variations in dew point and temperature are themselves highly correlated with each other.

Because we are examining the relationship between atmospheric water vapor content and spectral transmission, we describe the distance between atmospheres as the Euclidean distance (ED) between the measures of four parameters that describe the profile taken at four altitudes in the boundary layer. In particular, we use the dew-point temperature in  $^{\circ}C$ , water vapor mixing ratio  $w$  (in grams of  $H_2O$  per kilogram of all other gasses as in Eqn. (25)), absolute humidity  $\rho$  (grams of  $H_2O$  per cubic centimeter as in Eqn. (29)), and air density (as in Eqn. (28)) because these measures of water vapor are the most independent. (Relative humidity, for example, is dependent on both atmospheric temperature and dewpoint temperature.) The formula for the ED is shown in Eqn. (31), where  $m$  is the measure of water vapor content as a function of radiosonde layer  $z_i$  and atmospheric profile  $a_j$  and where  $\{a_1, a_2\}$  are the two atmospheric profiles under comparison.

$$d(a_1, a_2) = \sqrt{\sum_{i=1}^4 (m(a_1, z_i) - m(a_2, z_i))^2} \quad (31)$$

$$m \in \{T_{DP}, w, \rho, \rho_v\}$$

$$z_i \in \{0m, 500m, 1000m, 1500m\}$$

We also use the ED to describe the distance between spectral measurements  $m$  taken at 887 frequencies between  $3984 - 27020cm^{-1}$  by transmission ( $t$ ), reflectance ( $r$ ), and sensor reaching radiance ( $R_{sr}$ ) as shown in Eqn. (32).

$$\begin{aligned}
d(a_1, a_2) &= \sqrt{\sum_{i=1}^{887} (m(a_1, z_i) - m(a_2, z_i))^2} & (32) \\
m &\in \{t, r, R_{sr}\} \\
z_i &\in \{3984 - 27020cm^{-1}\}
\end{aligned}$$

*3.1.2 Water Vapor vs. Radiance Euclidean Distance Relationship.* In the following section, we present analysis of the different EDs to assess their relationship to changes in spectral radiance at the sensor. Results are presented in Fig. 7, where the  $x$ -axis is the ED between the atmospheric profile, as defined by four measures of water vapor content, as it appears in the 1<sup>st</sup> percentile (“most dry”) of the distribution and all higher percentiles of that distribution. In the first column, that measure of water vapor content is the dew point temperature in °C; in the second column, the absolute humidity in kilogram of  $H_2O$  per cubic meter; in the third column, the mixing ratio in grams of  $H_2O$  per kilogram of dry air; in the fourth column, the density of the air in kilograms of air per cubic meter ( $kg_{air}/m^3$ ). Note that the  $x$ -axis, with the exception of that for density, is labeled by percentile rather than by the ED values themselves.

In the fourth column, in which the  $x$ -axis shows the ED between the atmospheric profiles as measured by air density, we cannot label the  $x$ -axis with the percentiles because the nominal percentiles do not increase monotonically with the density for all altitudes in the boundary layer. As we discuss in Section 3.4.1, between the 10<sup>th</sup> and 20<sup>th</sup> percentiles of surface relative humidity, the temperatures obtained from the LEEDR database *decrease* even as the humidity increases. This effect is shown in Fig. 16 and affects the density calculation by Eqn. (28).

In the first row of graphs in Fig. 7, the  $y$ -axis is the ED between the total atmospheric transmittance – from the top of the atmosphere to the target to the sensor – as simulated under the 1<sup>st</sup> percentile atmosphere and those simulated under all other percentiles. In the second row of Fig. 7, the  $y$ -axis is the ED between

the “true” target reflectance (again using the 1st percentile of the distribution as the baseline) and its reflectance as estimated under atmospheric profile assumptions based on other percentiles of the distribution. In the third row of Fig. 7, the  $y$ -axis is the ED between the radiance reaching the sensor as reflected by the target as simulated under the 1st percentile and all other percentiles. While our initial examination included varying the choice of the percentile chosen as the baseline, we discovered that the shape and scale of the resulting relationship was largely independent of that choice. Note that the second and third rows also show the effect of targets with non-uniform emissivity. Specifically, they consider the built-in MODTRAN emissivities of “cropland,” “deciduous tree,” “galvanized metal,” and “olive paint” as the target spectra [49].

Several generalizations can be made from these relationships. Controlling for choice of vapor content measure (i.e., dew point, mixing ratio, absolute humidity, and density), the relationship between atmospheric transmission, estimated target reflectance, and sensor reaching radiance is approximately linear. This validates our expectation that the contribution of atmospheric emission to sensor reaching radiance is negligible. Thus, the sensor reaching radiance is approximately the product of the constant solar radiance and the atmospheric transmission for a given target. The target reflectance, in turn, is obtained from the ratio of sensor reaching radiances for the different atmospheres. We also see that the relationship between the absolute humidity and water vapor mixing ratio is also linear; as indicated by Eqn. (29), this is expected for  $q \ll 1$ .

As we can see from Fig. 7, the relationship between the ED of the estimated target reflectances (second row) and sensor reaching radiances (third row) and the various measures of atmospheric distance, while highly linear, are also highly target-dependent for the amount of change in radiance distance a given atmospheric distance will cause. We calculated the spectral energies  $W_s$  of the sensor-reaching radiances for each target as

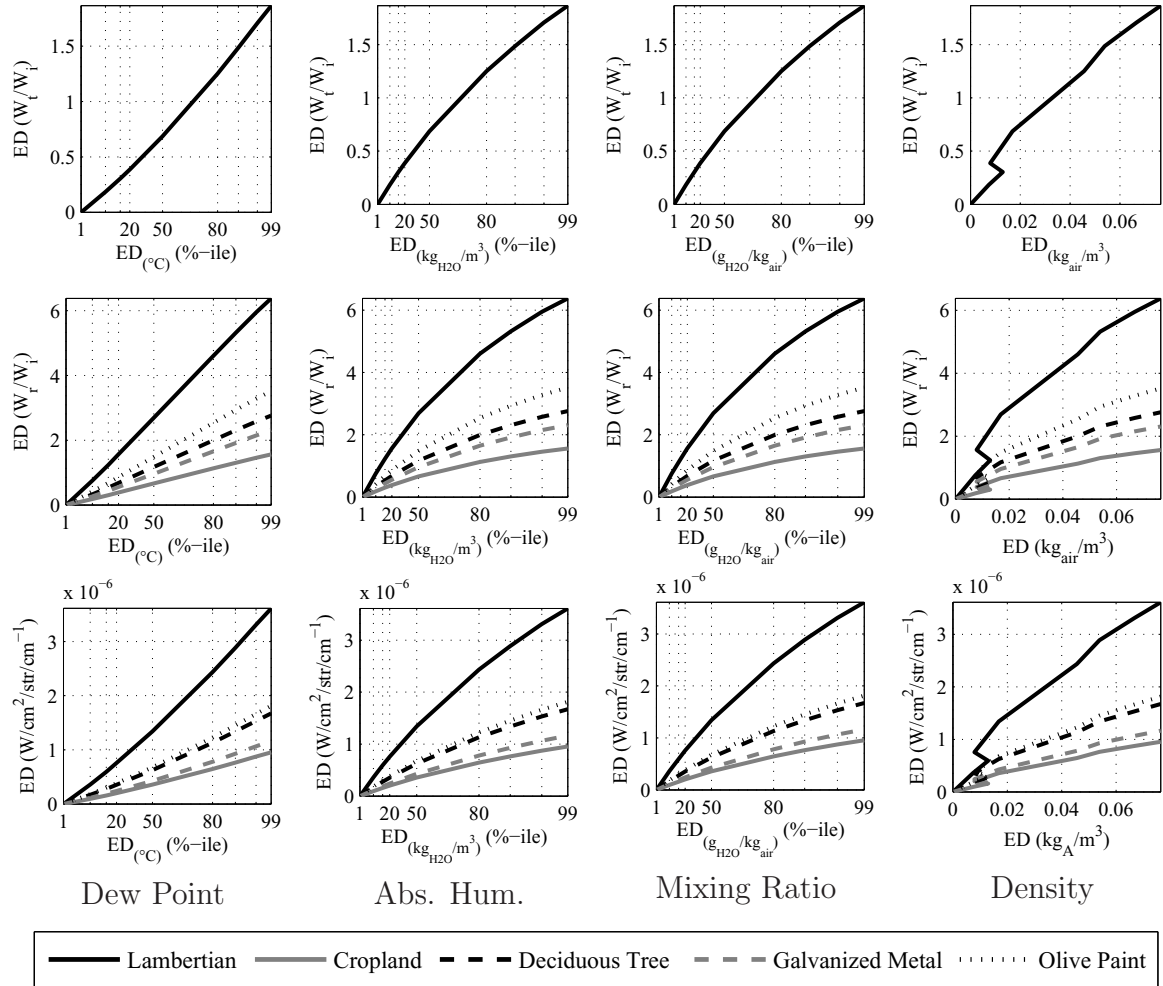


Figure 7: Plot of the ED between atmospheric water vapor content profiles ( $x$ -axis) and the EDs between total atmospheric transmittances, target reflectances, and sensor-reaching radiances as modeled under those profiles ( $y$ -axis).  $W_i$  is the radiance from the sun incident on the top of the atmosphere.  $W_t/W_i$  is the *atmospheric transmittance*, the percent of the solar radiance that propagates through the atmosphere, while  $W_r/W_i$  is the *target reflectance*, the percent of the incident solar radiance reflected.

$$W_s = \sum_{i=1}^N R_i \delta w, \quad (33)$$

where  $N$  is the number of spectral bands,  $R_i$  is the radiance at each band, and  $\delta w$  is the full width half maximum of the band. In general, we can see from Table 2 that the higher the overall radiance energy from a particular target (as measured by the magnitude of the radiance scaled by the spectral resolution), the greater the slope of the plot.

Table 2: Table of spectral energies (magnitude scaled by the spectral resolution) of four targets signatures.

Target	Spectral Energy ( $\mu W/cm^2/str$ )
Cropland	8.3101
Deciduous Tree	14.505
Galvanized Metal	12.392
Olive Paint	14.511

Otherwise, we see that while all relationships are highly correlated, they vary subtly depending on the choice of water vapor measurement. Mixing ratio and absolute humidity show an exponentially diminishing relationship with radiance. To develop an understanding of this, we consider the derivative of Eqn. (30) as a proxy for the Euclidean distance between the transmittances corresponding to different profiles. We begin by substituting Eqn. (27) into Eqn. (30), which yields

$$t = \exp \left[ -\frac{k_a w \rho_0 H}{\mu} \exp \left( -\frac{z}{H} \right) \right] = \exp \left[ -\frac{k_a H w}{\mu} \frac{P}{(1 + 0.6w) R_d T} \exp \left( -\frac{z}{H} \right) \right] \quad (34)$$

Taking the derivative with respect to the mixing ratio  $w$  yields

$$\begin{aligned}
\frac{dt}{dw} &= \left[ \frac{\mu(1 + .6w)R_dT(-k_aHP) - (-k_aHwP)(.6\mu R_dT)}{\mu^2(1 + .6w)^2 R_d^2 T^2} \right] \exp\left(-\frac{z}{H}\right) \cdots \\
&\exp\left[-\frac{k_aHw}{\mu} \frac{P}{(1 + 0.6w)R_dT} \exp\left(-\frac{z}{H}\right)\right] \\
&= \left[ -\frac{k_aHP}{\mu(1 + .6w)^2 R_dT} \exp\left(-\frac{z}{H}\right) \right] \cdot \exp\left[-\frac{k_aHw}{\mu} \frac{P}{(1 + 0.6w)R_dT} \exp\left(-\frac{z}{H}\right)\right]
\end{aligned} \tag{35}$$

We can observe from Eqn. (35) that as the mixing ratio increases, the absolute value of the derivative of the transmittance decreases. Thus, we would expect that at higher humidities, further changes in the humidity would have a diminishing impact on the transmittance.

Likewise, we can consider the derivative of the transmittance with respect to the absolute humidity  $\rho_v = pq \cong \rho w$ :

$$\frac{dt}{d\rho_v} = -\frac{k_aH\rho_v}{\mu} \exp\left(-\frac{z}{H}\right) \exp\left[-\frac{k_a\rho_v H}{\mu} \exp\left(-\frac{z}{H}\right)\right]$$

which again predicts that marginal changes to humidity have less effect at higher absolute humidity.

Further, Fig. 7 shows that dew point has a near perfect linear relationship. Density shows a noticeable discontinuity between the 10<sup>th</sup> and 20<sup>th</sup> percentiles; this reflects the decrease in the recorded temperature data corresponding to these percentiles in what is otherwise a positive correlation with relative humidity.

### 3.2 Target Detection with the AMF

After we use the atmospheric profiles to simulate a hyperspectral image cube, we then use the target signatures in the spectral library to detect those targets in the image. As discussed, there are many detectors available. We have chosen the AMF because of its popularity in the hyperspectral community. Validating our results with other detectors remains an objective of future research.

### 3.3 Evaluating Target Detection Error

We observe in Section 3.1.2 that changes in water vapor content in the boundary layer result in changes in the spectral output and that these changes, when measured by the Euclidean distance, bear an approximately linear relationship. We now wish to briefly examine the impact these changes have on the output of the AMF.

*3.3.1 The Bhattacharyya Coefficient.* To begin this evaluation, we choose as our metric the Bhattacharyya coefficient (BC). The Bhattacharyya coefficient measures the separation of two probability mass functions (PMF's) or normalized histograms. The Bhattacharyya coefficient is calculated by dividing the elements of each distribution into an arbitrary number of bins based on their values. It then applies the following formula:

$$BC = \sum_i \sqrt{p_i \cdot q_i},$$

where  $p_i$  and  $q_i$  are the fraction of PMF's  $p$  and  $q$  that fall within the  $i$ th bin. Thus, the values for the coefficient should range between zero (for no overlap between the distributions) to one (for complete overlap). If there are  $N$  atmospheric profiles under consideration, then we generate  $\frac{N(N-1)}{2}$  Bhattacharyya coefficients between them. While the Bhattacharyya coefficient was originally supposed to require that the underlying data be Gaussian [45], it has since been shown that it works for arbitrary distributions [44], and is thus used here.

To evaluate the effect of atmospheric changes using the Bhattacharyya coefficient, we undertake the process shown in Fig. 8. We generate a set of DIRSIG images, each from one of the nine atmospheric profiles corresponding to the nine boundary layer water vapor percentiles. We then pick a new target set, choosing targets with sufficient in-scene spectral variation to usefully model, and use the average of the in-scene target pixels in each distribution to generate the target signatures corresponding to that distribution. Finally we compare the distributions of the outputs of the AMF

for the target classes obtained from each distribution against all other distributions. The results of this comparison are shown in Fig. 9 [50]. Here, the  $y$ -axis shows the value of the Bhattacharyya coefficient, while the  $x$ -axis is scaled to the corresponding Euclidean distance between the dew point temperature profile in the boundary layer (as described in Section 3.1.2) associated with the percentile as labeled on the  $x$ -axis and that of the percentile serving as the baseline.

The results for measuring the Bhattacharyya coefficients between the reference distribution of the AMF output for each target and the distributions obtained under other atmospheric profiles are as expected. The comparison of the AMF output for each target and profile with itself results in a Bhattacharyya coefficient equal to one, representing perfect overlap. While some variation is noted, the generality is that the

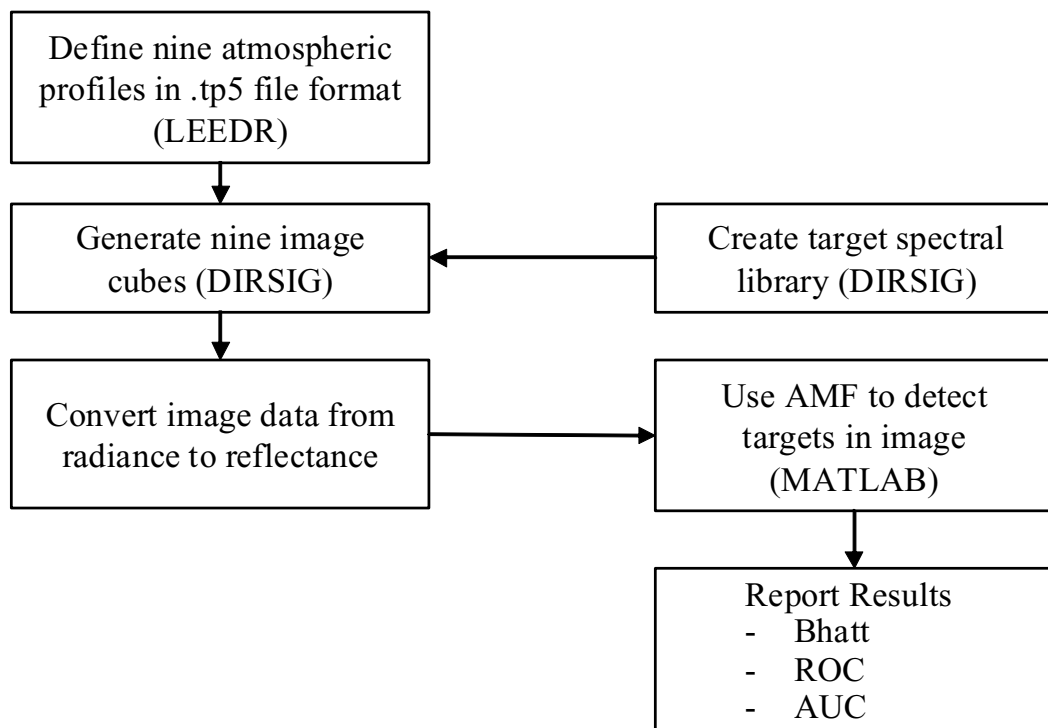


Figure 8: Process flowchart detailing methodology that performed detection in radiance space using target spectra taken from class averages as they appear in the fiftieth percentile DIRSIG image.

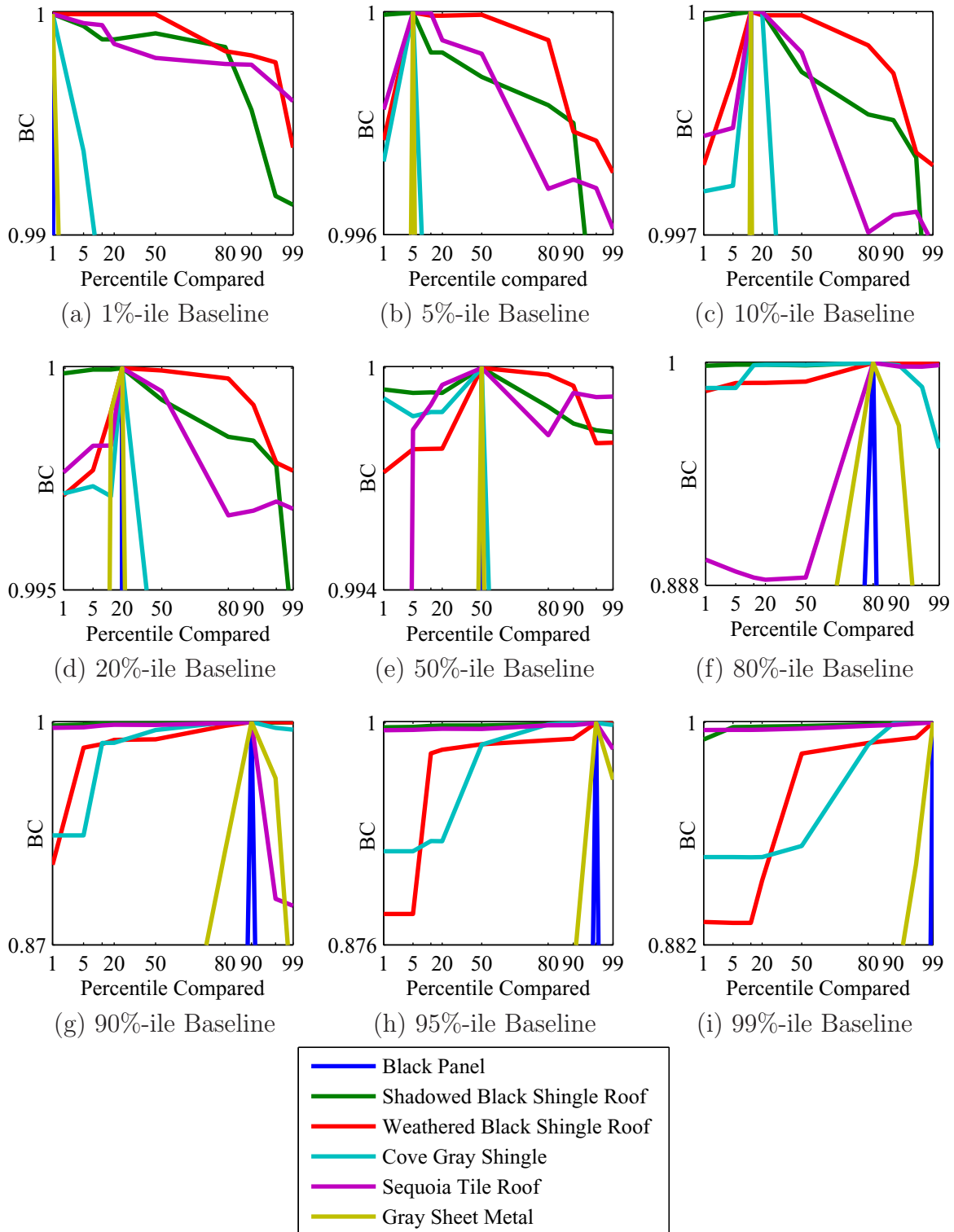


Figure 9: Plots of Bhattacharyya coefficients comparing the AMF output corresponding to the indicated percentile of the distribution of atmospheric water vapor to that corresponding to the other eight percentiles. We observe lower coefficients the greater the percentile separation, and therefore the water vapor content, between the atmospheric profiles.

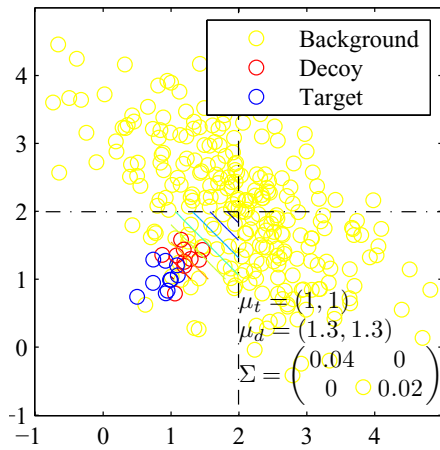
greater the difference in the water vapor content between the atmospheric profiles over the target, the lower the commonality, as measured by the Bhattacharyya coefficient, between their AMF outputs.

However, although the Bhattacharyya coefficient confirms our intuition that changes in the atmospheric water vapor content result in changes to the output of the AMF, it does nothing to estimate the effect on system performance. To understand the effect on detection, we must evaluate the AMF output using the receiver operating characteristic (ROC) curve, or variants thereof (i.e., the AUC).

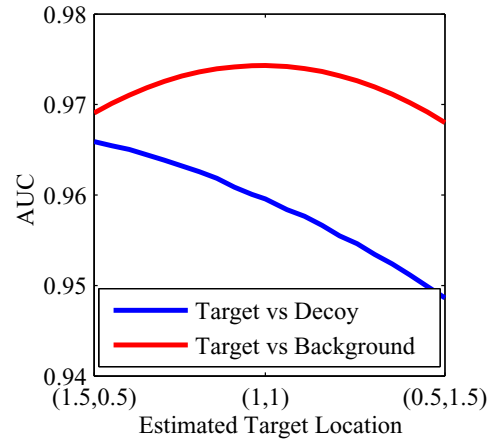
*3.3.2 AMF Detection with Atmospheric Error: a Pedagogical Example.* The problem of mis-estimation of the atmospheric parameters and the consequent incorrect atmospheric correction is one of essentially searching for a target in the wrong hyperspectral space. The precise effect this error has is dependent on a multitude of variables: the relative locations of the target, the overall background, and specific decoys as well as their covariance matrices.

To illustrate the interaction of these dependencies, we apply the AMF to two dimensional sets of Gaussian random variables of known means and covariances. By limiting ourselves to two dimensions (analogous to wavelengths in our actual and simulated hyperspectral images), we can easily visualize the location of all variables in hyperspectral space by use of scatter plots. We then systematically mis-estimate the target location for repeated applications of the AMF and calculate the AUC as a function of that mis-estimation.

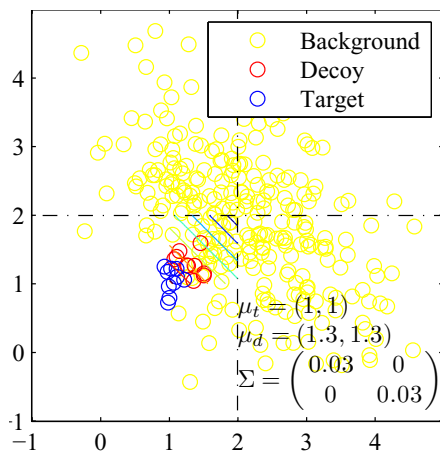
Illustrative of our results is Fig. 10. In Fig. 10(a), we show a scatter plot showing the target with a hyperspectral location of (1, 1) (the blue circles) and a close decoy at (1.3, 1.3) (the red circles) against a background centered at (2, 2) (the yellow circles). The black axes are centered at the background mean. In this example, the dimensions of the background are negatively correlated (henceforth referred to as having a *negative covariance*). We describe the covariance of the target and the decoy as *horizontal* – i.e., showing greater variance along the  $x$ -axis than along the  $y$ -axis



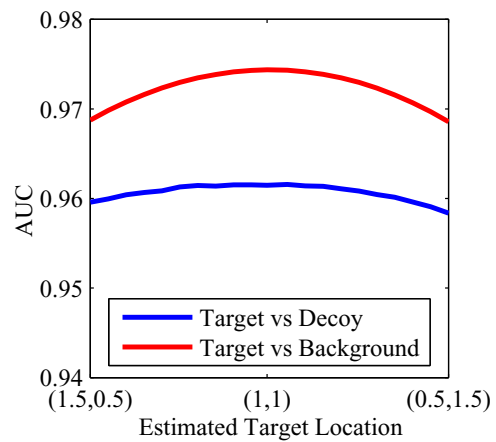
(a) Scatter plot, Horizontal  $\Sigma$



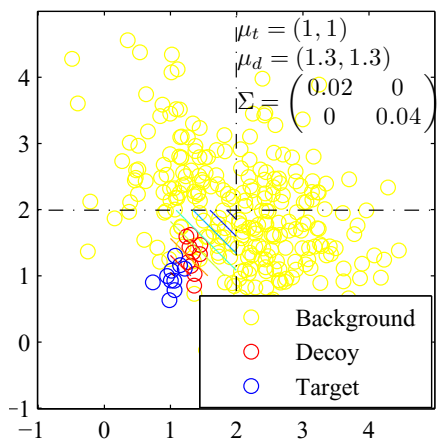
(b) AUC plot, Horizontal  $\Sigma$



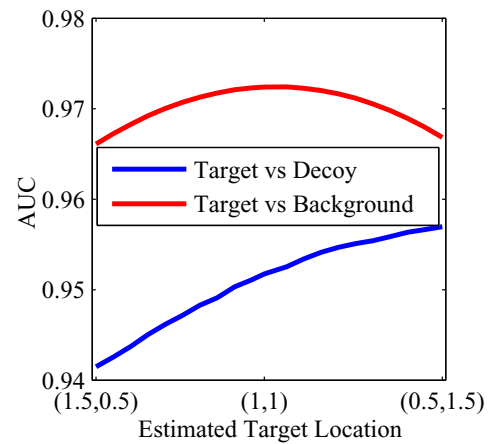
(c) Scatter plot, Circular  $\Sigma$



(d) AUC plot, Circular  $\Sigma$



(e) Scatter plot, Vertical  $\Sigma$



(f) AUC plot, Vertical  $\Sigma$

Figure 10: Scatter plots of targets, decoys, and background in two-dimensional hyperspectral space and the associated AUC plots by estimated target location. The true target ( $\mu_t$ ) and decoy ( $\mu_d$ ) locations, along with their covariance matrix ( $\Sigma$ ) are indicated in the scatter plots. The background covariance is negative.

– but their dimensions are otherwise uncorrelated. Also shown in this figure are the contour lines corresponding to the output of the AMF at each location; these are essentially linear discriminant functions (LDFs) [24] at different detector thresholds under the condition of perfect knowledge of the target location. Thus, the gradient of this contour runs directly from the mean of the background to the mean of the target as adjusted for the background covariance.

We then apply the AMF to a range of estimated target locations running in a straight line between  $(1.5, 0.5)$  and  $(0.5, 1.5)$ . (In all examples, this line is kept orthogonal to the gradient of the LDFs, as it is only along this direction that we would expect changes to the AUC.) Consider first the estimated target location of  $(1.5, 0.5)$ . Spatially, this point lies below and to the right of the true target location. We can easily visualize that an LDF with a gradient in this direction would, at any given threshold, mis-classify the background pixels in the fourth quadrant as target pixels, elevating the  $P_{fa}$  and lowering the AUC. However, because of the horizontal orientation of the target and background covariances, this actually *improves* the LDFs ability to distinguish between them.

In contrast, consider the estimated target location of  $(0.5, 1.5)$ . This point lies above and to the left of the true target mean. Again our LDFs generate an elevated number of false alarms, this time in the second quadrant. But now the horizontal orientation of the target and decoy work against us; they become more difficult to distinguish because their overlap along this gradient is much larger. Thus, the performance of the ROC deteriorates and the AUC shrinks.

These trends are illustrated in Fig. 10(b), where we plot the AUC for the AMF detection of the target against the entire background (the red line) and the decoy pixels only (the blue line). The AUC for detection against the background peaks at the true target location  $(1, 1)$ , and deteriorates as we move away from it. The AUC for detection against only the decoys peaks as we search at  $(1.5, 0.5)$  and troughs at  $(0.5, 1.5)$  as we expected. Note that the AUC for detection against decoys is in all

cases lower than the AUC against the background; this is because the means are much closer and the overlap is much greater.

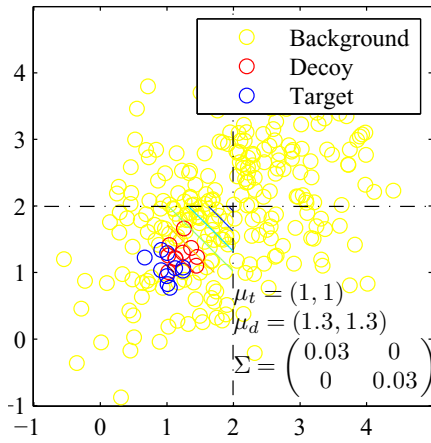
We reverse the orientation of the target and decoy pixels in Fig. 10(e) from horizontal to vertical. As we can see in Fig. 10(f), while the detection results against the background remain largely unchanged, the advantage for detection against the decoy now occurs at the location  $(0.5, 1.5)$  where the AUC peaks. This is consistent with the LDFs being now aligned towards the vertical direction and thus better discriminating between target and decoy pixels.

When the covariance matrices of target and decoy are circular as in Fig. 10(c), there is no advantage to mis-estimating the target location. As we can see in Fig. 10(d), the AUC peaks at the true target location of  $(1, 1)$  for both detection against the background and detection against the decoy.

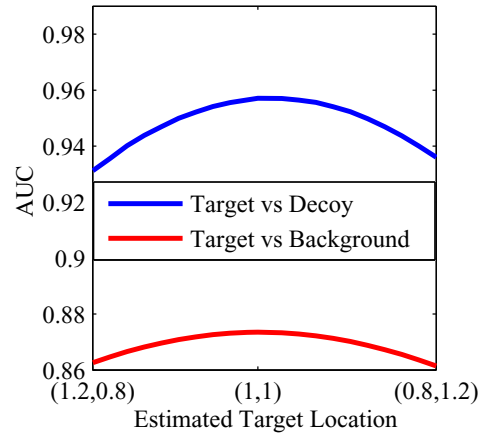
We perform further experiments illustrated in Fig. 11. In Fig. 11(a), we have now reversed the covariance of the background itself from negative to positive. This puts both the target and decoy pixels amidst a much greater number of background pixels – so much greater, in fact, that the background now generates proportionally more false alarms than the decoy. The result is shown in Fig. 11(b), where the AUC curve for the background detection lies below that for the decoy detection.

In Fig. 11(c), we move the target and background pixels to the 2<sup>nd</sup> quadrant while keeping their relative orientation. As we can see from the LDFs, the target and decoy are almost indistinguishable to the AMF. By pointing the AMF away from the true target location to a point below and to the right of it, we can improve the detector performance even though the target and decoy covariances are circular; however, as we can see from Fig. 11(d), the AUC for the decoy is now much lower than it has been in all previous examples.

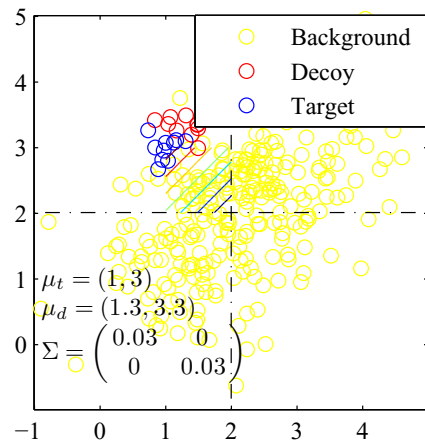
Finally, in Fig. 11(e) we move the target and decoy to the 1st quadrant. Significantly, the decoy is now further away from the background mean than is the target along both dimensions. Thus, as we can see from Fig. 11(f), the AMF consistently



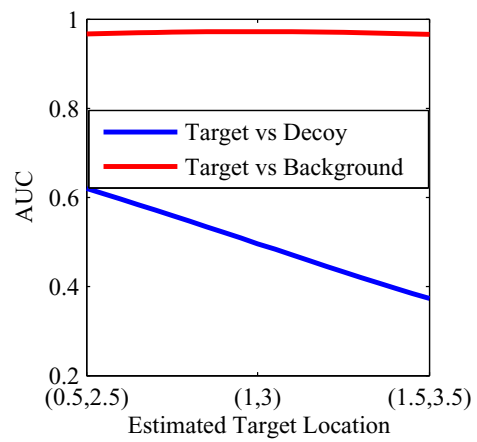
(a) Scatter plot, 3<sup>rd</sup> Quadrant



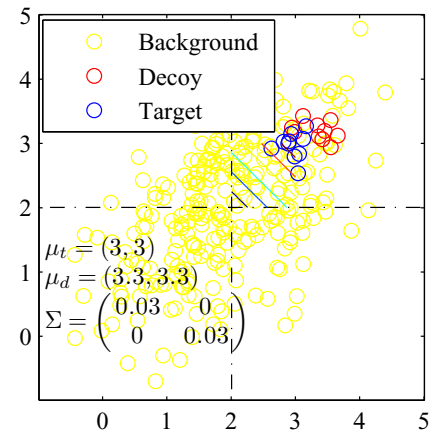
(b) AUC plot, 3<sup>rd</sup> Quadrant



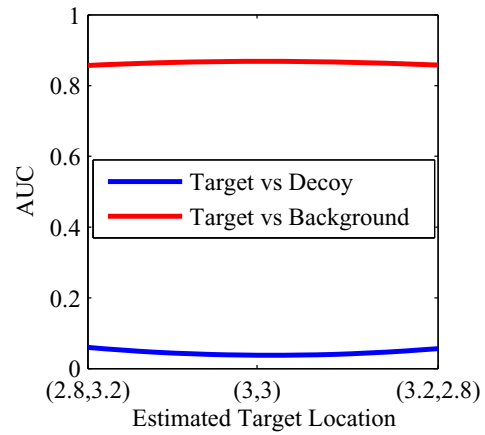
(c) Scatter plot, 2<sup>nd</sup> Quadrant



(d) AUC plot, 2<sup>nd</sup> Quadrant



(e) Scatter plot, 1<sup>st</sup> Quadrant



(f) AUC plot, 1<sup>st</sup> Quadrant

Figure 11: Scatter plots of targets, decoys, and background in two-dimensional hyperspectral space and the associated AUC plots by estimated target location. The true target ( $\mu_t$ ) and decoy ( $\mu_d$ ) locations, along with their covariance matrix ( $\Sigma$ ) are indicated in the scatter plots. The target and decoy covariance matrix is circular. The background covariance is positive.

ranks the decoy higher than the target regardless of the search direction; thus the AUC values for the search against the decoy is below the level of random guessing and troughs at the true target location.

These figures illustrate our premise that the distribution of the target and various decoys in relation to the covariance eigenvectors directly impacts the shape of the resulting ROCs and AUCs for that target. We move on to see that the shapes of ROCs and AUCs for simulated targets against a representative background are similarly variable.

*3.3.3 Determining the Best Atmospheric Assumptions.* Given the uncertainty associated with the true atmospheric conditions in effect at the time of any particular image, our intuition is that the maximum likelihood estimate of those conditions would lie at the middle of their historic distribution. However, this is an intuition only; testing it requires that we consider the AUC for our detector as a function both of the true atmospheric profile and the estimate we make about it. This leads us to the use of contour plots. Further, by summing the AUC outputs across the range of true atmospheres for each estimated atmosphere, we can identify which estimated atmosphere maximizes the detector performance, given our uncertainty. We review the results of this analysis in Chapter IV in their entirety; however, below is an example of what we produce. As we see in Fig. 12(a), the best atmospheric assumptions, as indicated by the vertical dotted line, can conform to our intuition by residing at the 50<sup>th</sup> percentile. However, depending on the target, the optimum assumption can be well away from that percentile, as we see in Fig. 12(b).

### **3.4 Simulation Methodology**

Determining how the relationship between the estimated and true atmospheric profiles affects the performance of the AMF in target detection requires that we simulate imagery acquired under a range of atmospheric conditions. In this section

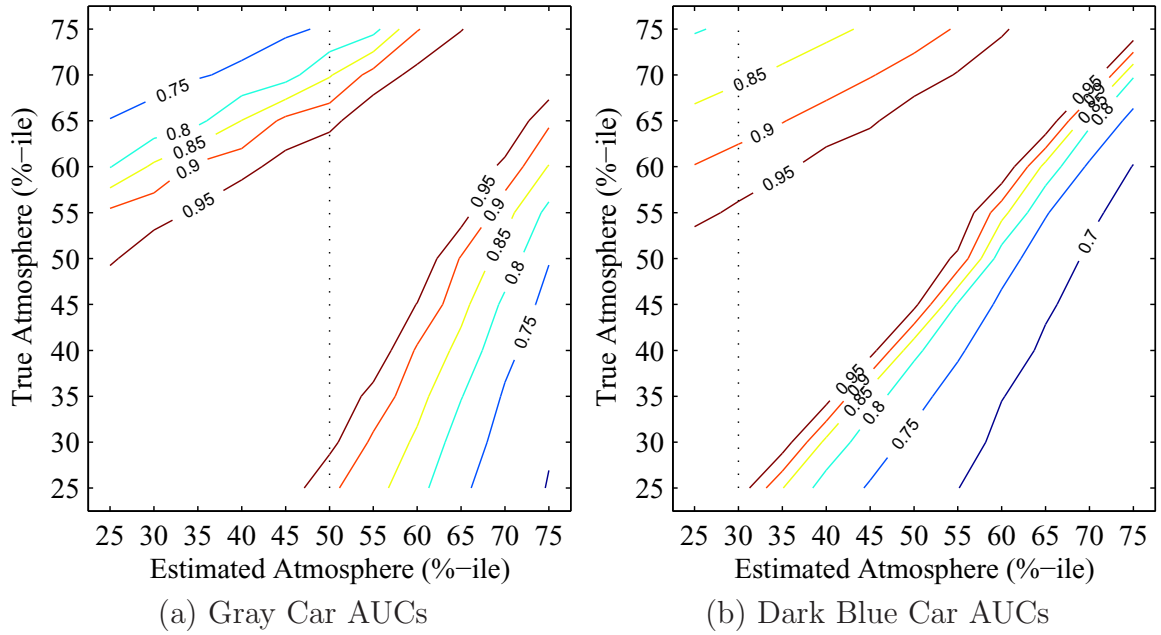


Figure 12: Two examples from Appendix D of contour plots of the AUC for AMF detection of automobiles of the indicated colors as a function of estimated atmospheric profile ( $x$ -axis) and true atmospheric profile ( $y$ -axis), measured in percentiles of their historic distribution of relative humidity.

we provide introductory information on the modeling and simulation environments used to generate the data used in our study and described in Fig. 13.

We begin by using the Laser Environmental Effects Distribution Reference (LEEDR) to generate a set of atmospheric profiles as described in Section 3.4.1. We integrate those profiles into a set of configuration files called “TAPE5” files that MODTRAN uses to calculate the expected radiance spectrum reaching the sensor from a target with a uniform reflectance of one, as described in Section 3.4.2. We then choose the spectrum corresponding to the fiftieth percentile atmospheric profile to generate a hyperspectral image cube from a three-dimensional scene model using the Digital Imaging and Remote Sensing Image Generation Model (DIRSIG) as described in Section 3.4.3. We re-condition this image as if it were simulated under other profiles and convert the image from radiance to reflectance values. Finally, we run the AMF against the designated target set using the reflectance spectra contained in the DIRSIG’s material database, and present our results.

We repeat the process, continuing to use the fiftieth percentile image but using MODTRAN to generate radiance spectra corresponding to each of the other percentiles for which LEEDR can provide atmospheric profile data. By dividing the image by the different radiance spectra, we simulate the error conditions which unknown atmospheric variation create.

*3.4.1 Atmospheric Parameters.* Because our objective is to characterize the uncertainty associated with the estimate of atmospheric parameters on the radiative transfer algorithm, we must have measured atmospheric data showing the historic distribution of those parameters about their accepted median values. One such database was developed by the Air Force Institute of Technology (AFIT) Center for Directed Energy under sponsorship from the High Energy Laser Joint Technology Office (HEL JTO). The program is called High Energy Laser End to End Opera-

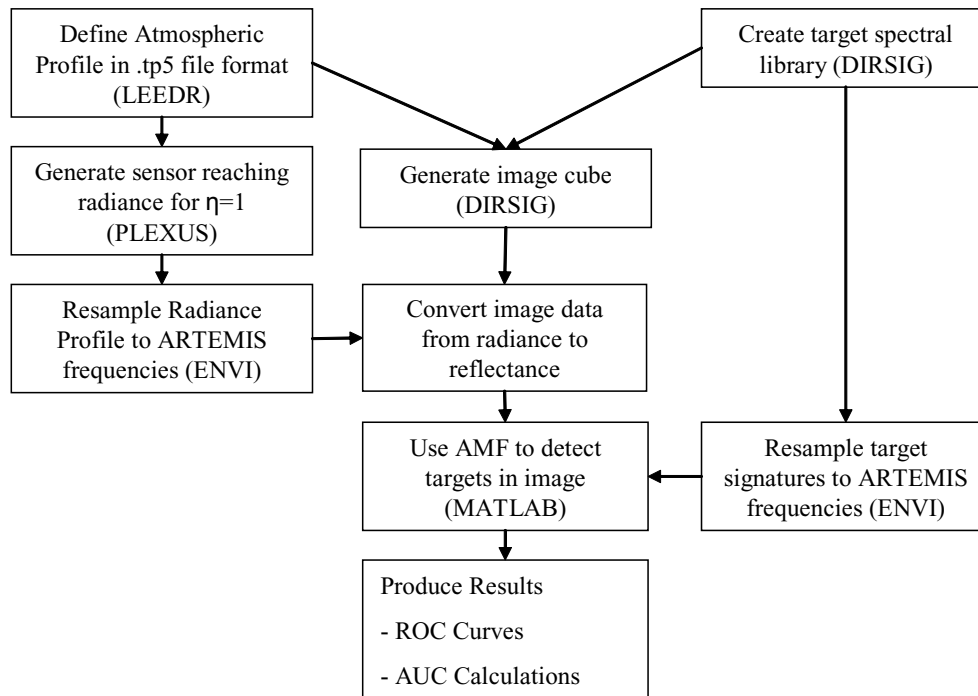


Figure 13: Process flowchart detailing methodology that performed detection in reflectance space using PLEXUS-generated radiance data to convert image data cube to reflectance.

tional Simulation (HELEEOS), which is used to predict atmospheric affects on directed energy weapons [17]. The worldwide atmospheric characterizations employed in HELEEOS are based on the same databases and algorithms used in the LEEDR program. LEEDR was developed by the AFIT Directed Energy Center under the combined sponsorship of HEL JTO and the Air Vehicles and Sensors Directorates of the Air Force Research Lab (AFRL). The associated parameters are obtained for eight different time-of-day ranges, on a particular month of the year, and expressed at nine different percentiles: 1%, 5%, 10%, 20%, 50%, 80%, 90%, 95% and 99%.

These atmospheric profiles express both temperature and dew point at various pressure altitudes. Other parameters are available; however, these are calculated from mathematical models of these first three parameters (temperature, dewpoint, and pressure).

*3.4.2 PLEXUS.* With atmospheric profile information provided by HELEEOS and LEEDR, it is possible to apply MODTRAN to a specific target and scene geometry to obtain the sensor reaching radiance. This is accomplished with the Phillips Laboratory EXpert User Software (PLEXUS). PLEXUS applies a radiative transfer model (specifically MODTRAN) to an atmospheric profile, various other weather conditions, and scene geometry to generate a sensor reaching radiance. This radiance, when multiplied by a target reflectance spectrum, yields the spectrum of a particular target as seen by the sensor under the particular conditions.

In our experience, PLEXUS showed itself to be too cumbersome and unstable an operating environment for producing multiple spectra under different user-defined atmospheric profiles. However, PLEXUS was able to render correctly the scene geometry and other settings in the TAPE5 format, which we successfully fed as inputs to MODTRAN.

*3.4.3 Image Simulation.* Image data are simulated using a program developed by a team from Rochester Institute of Technology called DIRSIG [42]. This sim-

ulation environment allows three-dimensional scene construction including the size, shape, and placement of objects in relation to other objects. It allows the simulation of a variety of imaging devices, platforms and mission profiles. Its output takes into consideration not only atmospheric conditions, location, and solar illumination, but adjacency effects and the Bidirectional Reflection Distribution Function (BRDF) as well. We use DIRSIG to simulate a single-capture data cube as collected from the AVIRIS platform [21]. The MODTRAN module of DIRSIG allows the user to simulate the images as they would be collected under user-defined atmospheric profiles. By varying these profiles according to their distribution at the target location, we develop a set of images corresponding to those distributions.

## IV. Results

### 4.1 Data

4.1.1 *DIRSIG-Generated Imagery.* The DIRSIG image cube is generated using the assumption of standard atmospheric conditions corresponding to a clear, mid-latitude summer day. We use the Megascene, RIT's model of northwest suburban Rochester [28]. The Megascene came with a reflectance library of 47 spectrally distinct material types. To these we add additional material types spectrally representative of 41 different automobiles. These materials are mixed in various proportions, in increments of one ninth, for each pixel. We then simulate an image cube as collected by the AVIRIS sensor [21] imaged at nadir (zenith =  $180^\circ$ ) from 10,000 feet AGL on



Figure 14: The RGB representation of the simulated hyperspectral image of DIRSIG's "Megascene" RIT's by-element construction of a Rochester NY suburb [28].

1 June 2001 at 1300L. The elevation of the scene is simulated at 300m and its location at 43° latitude and 77° longitude. A red, green, and blue (RGB) color component representation of the hyperspectral data cube is shown in Fig. 14. Our detections are run on square panels composed of the 41 vehicle types inserted into the model.

The nearest LEEDR site to the city of Rochester, the site of our DIRSIG image, is Griffiss AFB in Rome, New York [2]. Since our image is simulated as taken at 1300L on 1 June 2001, we generate our nine atmospheric profiles for Griffiss AFB in June between 1200L - 1500L.

Table 3: List of car colors and their material identification numbers that appear in the “megascene” image. Each material ID indicates a specific automobile. Note that there are often more than one car of the same color.

Automobile Color	Material IDs
black	20102, 20104, 20118, 20122, 20124, 20126, 20127, 20130, 20135
blue	20107, 20137
blue w/black top	20133
brown	20125
charcoal gray	20140
cranberry	20136
dark blue	20106
gold	20108, 20110, 20116, 20139
gray	20141
gray w/black top	20120
green	20123, 20132
light gold	20115
maroon	20105, 20128
red	20111, 20117, 20131
red/silver	20138
silver	20109, 20112, 20114, 20119, 20121, 20129, 20134
sterling	20113
white	20101, 20103

The spectral library contains multiple spectra for each material type based on different assumptions made about the illumination conditions. The number and resolution of these spectra differ between material types. Unfortunately, there is presently no way in DIRSIG for the user to know which of these spectra was used to make the final radiance calculation. This problem is overcome by averaging the spectra together to form the target signature.

*4.1.2 Target Set.* We insert 41 panels into Megascene, where the panels have spectral properties derived from measurements taken from 41 automobiles [1]. The reflectance spectrum for each vehicle was taken multiple times to ensure that the simulated image contained the natural variation of the automobile in question. The automobiles came in 18 different colors as listed in Table 3. Next to each of these colors is listed the material identification number(s) of the panels bearing that color, each panel corresponding to a specific automobile. For instance, nine of the automobiles were judged to be the color “black” in the judgment of the data collection team.

In Fig. 15, we show the reflectance spectra for four automobiles. (The reflectance spectra for all other automobiles are shown in Appendix A.) The black dotted lines represent the spectra as they are taken from the spectra library; it is these spectra the AMF uses as a signature database. The colored spectra are as they appear in the simulated DIRSIG image after atmospheric correction using the percentile indicated. We can see that adjacency and mixed pixel effects introduce a bias to the target spectra apart from the atmospheric effects, which are most salient at the  $0.97\mu m$ ,  $1.2\mu m$ ,  $1.4\mu m$  and  $1.9\mu m$  water vapor absorption bands. Following common hyperspectral image processing protocols, we remove the water vapor absorption bands from consideration; however, there is still considerable effect at the periphery of those bands, plus smaller effects in all bands not readily visible at this figure scale.

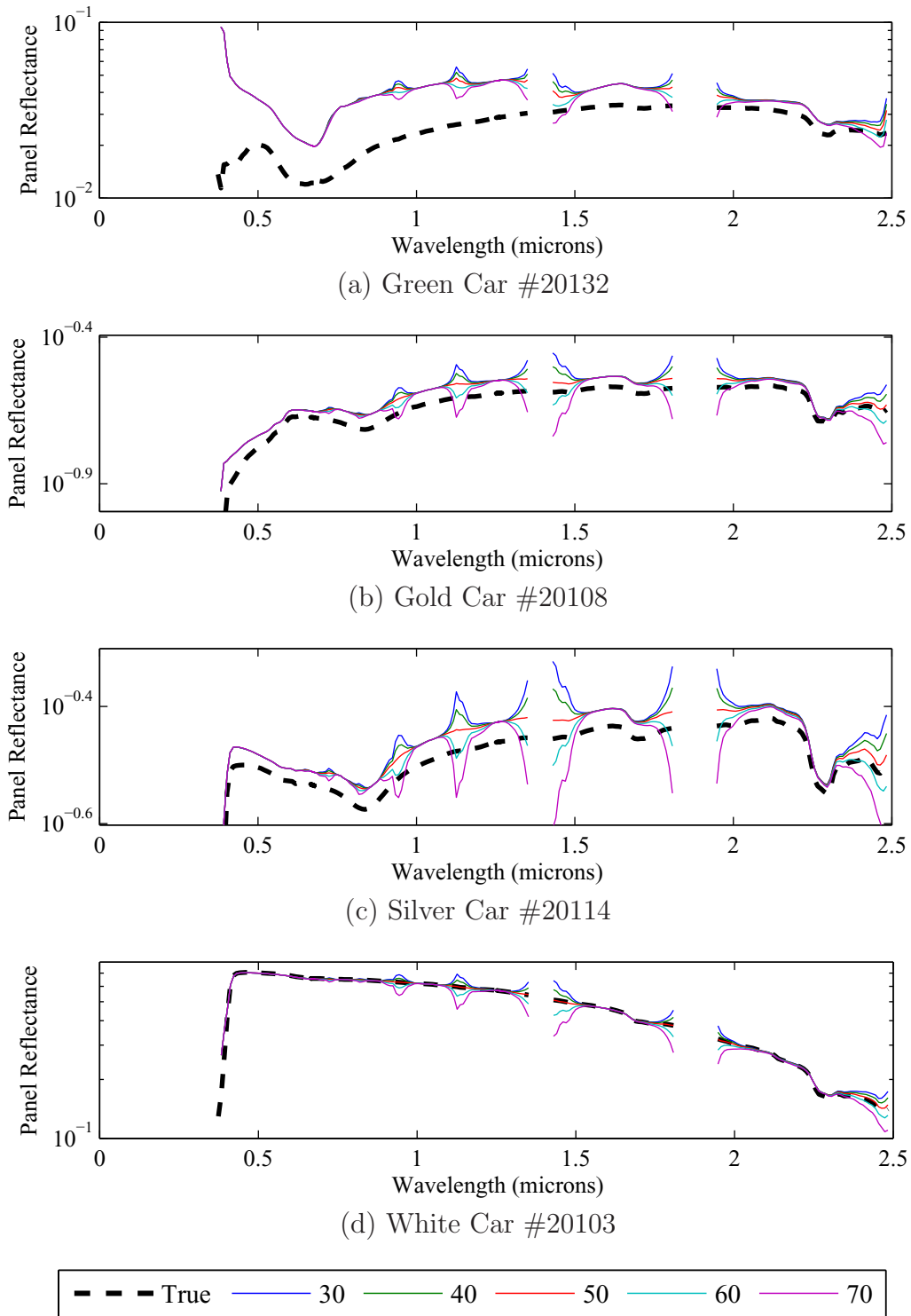


Figure 15: Reflectance spectra for the automobiles indicated. The “true” spectra (heavy black dashed line) are taken from the spectral library and were calculated as the average of all the truth measurements of the specific automobile. The estimated spectra, indicated by the atmospheric percentiles used for the estimation, represent the average of the image pixels bearing the specific material ID.

4.1.3 *Atmospheric Data.* We show the distribution of the dew points and temperature in Fig. 16 at four altitudes inside the boundary layer as a function of percentile. (LEEDR does not vary the atmospheric parameters by percentile above the boundary layer, but rather assigns each layer its regional average, i.e. “mid-latitude north summer” in this case.)

As mentioned in Section 3.1.2, we note the non-monotonic nature of the temperature profile, in particular the drop in atmospheric temperatures between the 10<sup>th</sup> and 20<sup>th</sup> percentiles of surface relative humidity, causing the “kink” in the Euclidean distance relationships involving density in Fig. 7. Future research should obtain access to the LEEDR data set and separate these two factors into a genuinely two-dimensional probability distribution of the parameters. For this work, however, we take the tem-

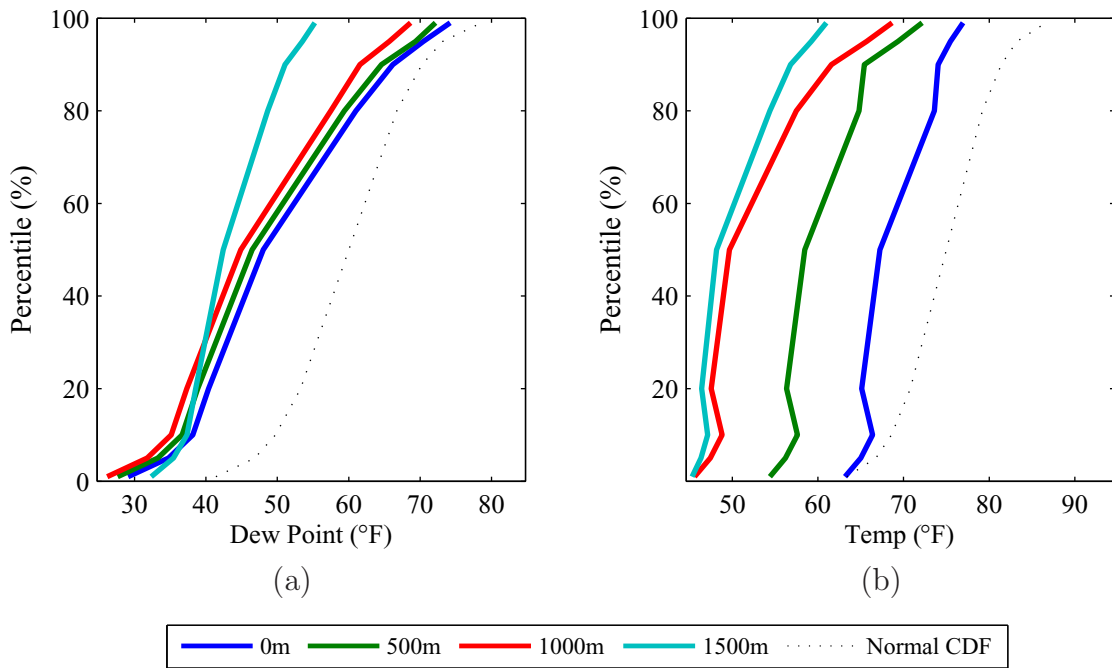


Figure 16: Plots of the atmospheric dew point percentile versus (a) the dew point value and (b) the atmospheric temperature in °F corresponding to that percentile. Four altitudes and an arbitrary Gaussian CDF are shown; LEEDR shows no variation by percentile for higher altitudes. Note that the atmospheric temperature decreases between the 10<sup>th</sup> and 20<sup>th</sup> percentiles of the dew point.

peratures in Fig. 16(a) to represent average values of measurements corresponding to the indicated percentiles of humidity in Fig. 16(b).

Fig. 9 previously showed that the Bhattacharyya coefficients for the AMF output generated for reflectances calculated under the 1<sup>st</sup> thru the 99<sup>th</sup> atmospheric water vapor percentiles suggested that there is insufficient granularity between those nine percentiles. Generally, we see in Fig. 9 that while the Bhattacharyya coefficient peaks at the 50<sup>th</sup> percentile, as we would expect given that the AMF distributions are mathematically identical under that assumption, there is little variation and no consistent pattern among the other percentiles. This confounds our prediction that the Bhattacharyya coefficient would steadily decay the further the true atmospheric water vapor content diverged from the assumed value at the 50<sup>th</sup> percentile. The rapid falloff in overlap followed by relative insensitivity to increased profile error indicates the possibility that most of the degradation occurs between the 20<sup>th</sup> and the 80<sup>th</sup> percentiles.

We therefore interpolate between the values of the atmospheric water vapor content as were provided in the LEEDR database. We use cubic interpolation to estimate the atmospheric parameters at the 25<sup>th</sup>, 30<sup>th</sup>, 35<sup>th</sup>, 40<sup>th</sup>, 45<sup>th</sup>, 55<sup>th</sup>, 60<sup>th</sup>, 65<sup>th</sup>, 70<sup>th</sup>, and 70<sup>th</sup> percentiles of the historic distribution. It is these values, along with the measured value at the 50<sup>th</sup> percentile, that we use throughout the remainder of this dissertation.

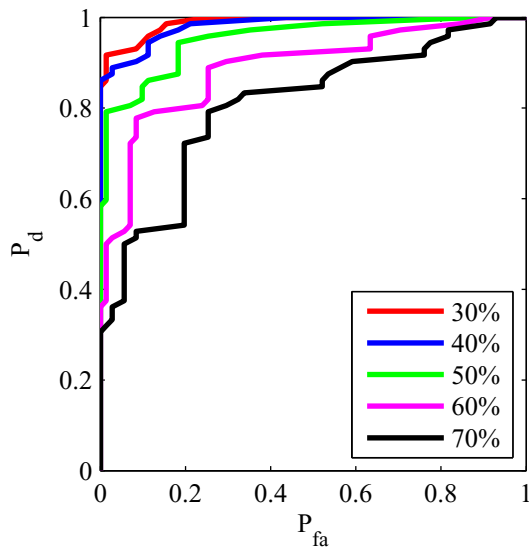
## ***4.2 Receiver Operating Characteristic as a Function of Atmospheric Percentile***

*4.2.1 The ROC Explained.* The receiver operating characteristic (ROC) curve is a useful tool in evaluating the overall ability of a detector to distinguish between target and background. A target detector typically considers some quality about an object (e.g., a reflectance spectrum), evaluates it by some criterium (e.g., a library spectrum), and produce a number measuring the relative strength of the congruity between the object and the criterion (e.g., the output of the AMF). A

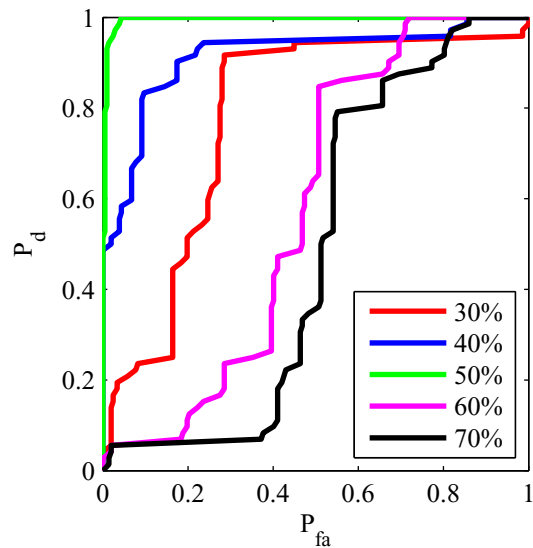
decision threshold then attempts to separate the objects of the class being sought (the target class) from those of the background class (collectively, the background class is all other classes). The efficacy of a particular threshold can be evaluated by comparing two numbers: the probability of detection ( $P_d$ , the percentage of the members of the target class correctly identified) and the probability of false-alarm ( $P_{fa}$ , the percentage of the members of the background class incorrectly identified).

A ROC curve plots the  $P_d$  against the  $P_{fa}$  for every threshold at which a target class member is evaluated. The resulting graph provides an easy way of evaluating the strength of the classifier independent of both a particular threshold and the target density [13], [27].

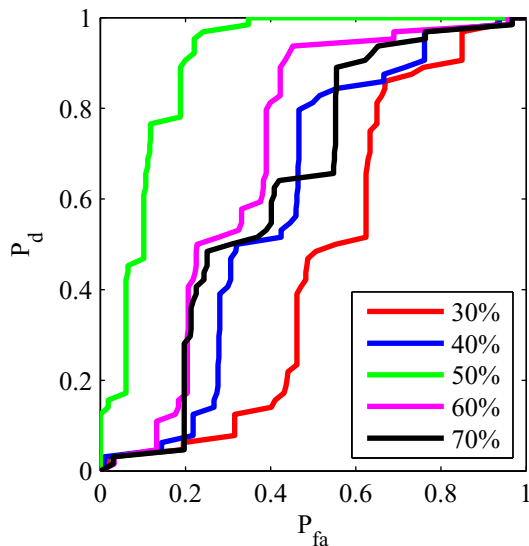
*4.2.2 ROCs by Target.* The ROC curves for four automobiles are shown in Fig. 17. (All other ROC curves are shown in Appendix B and Appendix C.) As described in Section 3.4, we condition the image on different percentiles of the atmospheric distribution at the target site; these percentiles are indicated in the figure legend. We then estimate the image reflectances based on the assumption that the atmospheric conditions were at the 50<sup>th</sup> percentile. Finally, we perform an AMF target detection for the automobile panels using the panel's reflectance spectrum as contained in the spectral library. Our expectation is that the best detection performance is for the atmospheric profile that matches our assumption and that the performance will grow progressively worse the more the truth diverges from that assumption. Note that while the covariance matrix of the AMF is calculated from the entire image as corrected to the 50<sup>th</sup> percentile assumption, the  $P_{fa}$ 's are calculated considering only other automobiles of the same color. For example, the ROC curves shown in Fig. 17(d) are generated by successfully distinguishing white car #20103 from white car #20101, not from the background as a whole. This is representative of the hardest case; our hypothesis is that the mis-estimation of the atmospheric water vapor profile for purposes of atmospheric correction will have the most significant impact on our ability to separate targets that are spectrally similar.



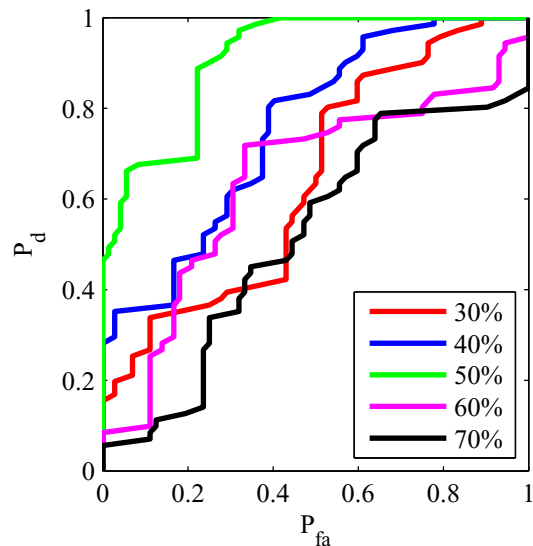
(a) Green Car #20132



(b) Gold Car #20108



(c) Silver Car #20114



(d) White Car #20103

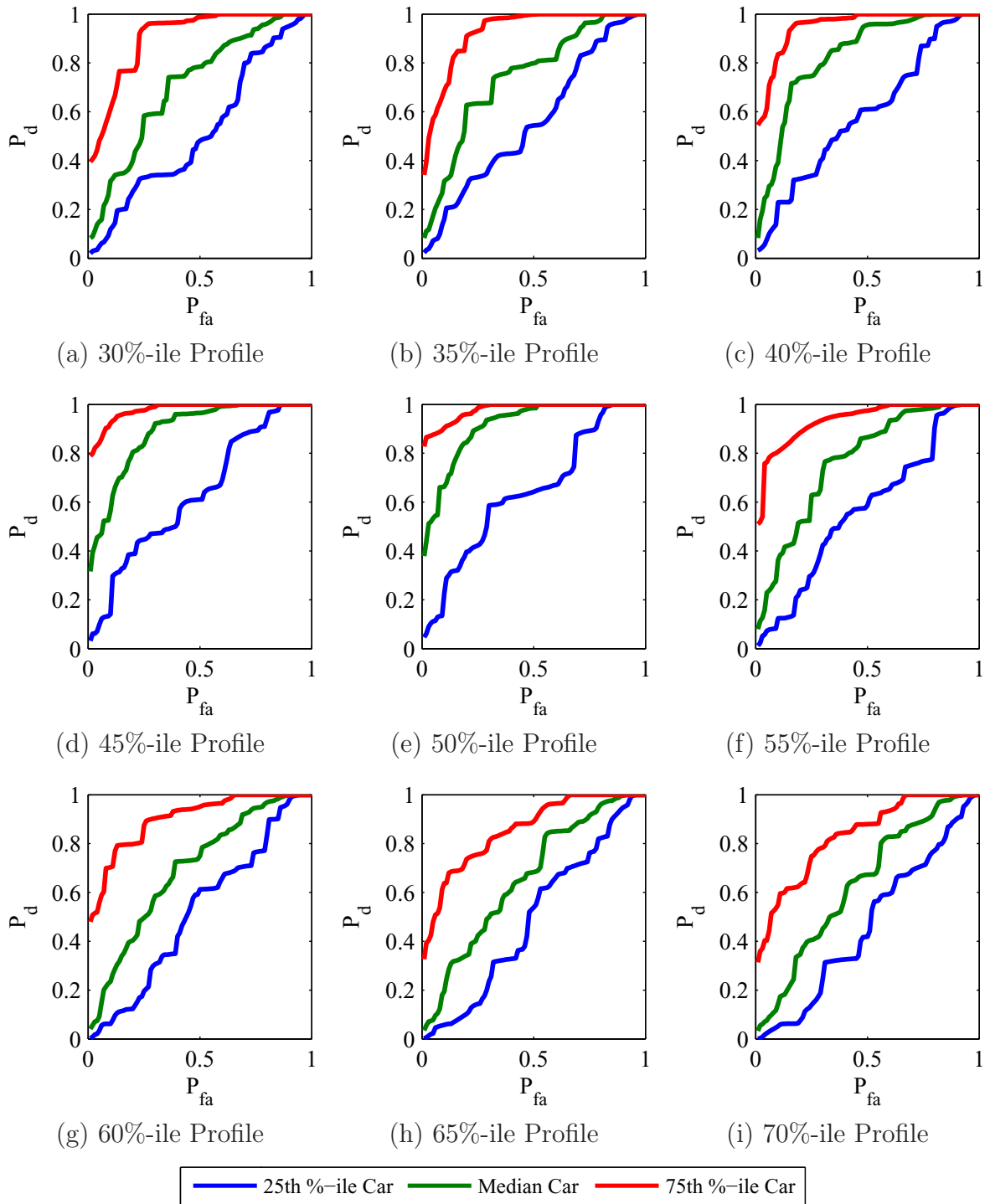
Figure 17: Receiver Operating Characteristic (ROC) curves for AMF detection of: (a) green car #20132; (b) gold car #20108; (c) silver car #20114; and (d) white car #20103. The “estimated” atmosphere used to convert the image radiance measurements to reflectance was the 50<sup>th</sup> percentile; the “true” atmosphere used to simulate the image radiances are indicated in the legend. Note that the probabilities of false alarm ( $P_{fa}$ ) are calculated from only among cars of the same color as the target car.

We can make several observations about the resulting ROC curves. For three of the automobile panels – Gold, Silver, and White – we observe the best detector performance corresponding to a true atmospheric profile at the 50<sup>th</sup> percentile (i.e., the one matching our assumption). However, for the Green automobile panel, we see that the detector performance continues to improve as the true atmospheric profile becomes more dry, approaching the 30<sup>th</sup> percentile in the distribution. This counter-intuitive result suggests the converse possibility: for certain targets, the optimum atmospheric profile estimation may be other than the 50<sup>th</sup> percentile of the distribution. We explore this possibility later in Section 4.4.

We also note several differences between the graphs. The overall effect of the mis-estimation varies between the targets. It appears that it has the least effect on the Green car and the most effect on the Gold car. We also see that, while, with the exception of the Green car, performance degrades the further away the estimate from the true profile, this degradation is lopsided. For instance, in Fig. 17(b), we see that the performance for the 60<sup>th</sup> and 70<sup>th</sup> percentiles is worse than for the 30<sup>th</sup> and 40<sup>th</sup> percentiles, in Fig. 17(c) the performance for the 30<sup>th</sup> and 40<sup>th</sup> percentiles is worse. It is our belief that these differences are due to the relative distributions of the targets and decoys in hyperspectral space compared to that of the background, as illustrated by our analysis in Section 3.3.2.

*4.2.3 ROCs by Percentile.* In Fig. 18, we have organized the results differently. For the 41 cars for which we have more than one car of each color, we have organized the in-color ROC curves at each atmospheric profile by plotting the 25<sup>th</sup>, median, and 75<sup>th</sup> percentile values of the  $P_d$  for each value of the  $P_{fa}$ . In other words, for each value of the  $P_{fa}$ , we order the  $P_d$ s of the 41 automobiles from highest to lowest. We then plot the  $P_d$  versus  $P_{fa}$  for the 10<sup>th</sup>, 21<sup>st</sup>, and 32<sup>nd</sup> highest  $P_d$  values. The generality from Fig. 17 continues to apply: we see that as the true atmospheric profile approaches the estimated atmospheric profile of 50% (Fig. 18(e)), the detector perfor-

mance continues to improve such that higher accuracies become possible. However, to confirm this observation, we further evaluate and quantify them in Section 4.3.



Legend

Figure 18: In-color ROC curves for the median, 25<sup>th</sup> percentile, and 75<sup>th</sup> percentile automobile. The “estimated” atmosphere used to convert the image radiance measurements to reflectance was the 50<sup>th</sup> percentile; the “true” atmosphere used to simulate the image radiances are indicated for each figure. The percentiles indicated in the legend refer to order of each car’s ROC curve, from lowest to highest.

### 4.3 Area under the Curve (AUC) as a ROC Performance Measure

While a visual inspection is often sufficient to recognize which of several ROC curves plotted on the same axes indicates a superior detector (as measured by yielding high  $P_d$  values at low  $P_{fa}$  values), the large number of comparisons we wish to make require us to reduce the ROC performance to a single number. To this end, we measure the detector performance by calculating the area under the ROC curve (AUC) [8]. The AUC allows us to avoid the difficulty of picking a threshold for detection, gives us a metric that is insensitive to the relative frequency of our target pixels in the image, and tells us the probability that a randomly chosen target pixel will be ranked higher than a randomly chosen background pixel [13]. The AUC is sufficiently robust that its use can be extended to other purposes [48], including multi-classification systems [23]. In Fig. 19, we plot the AUC against the percentile of the true atmosphere for nine automobile panels corresponding to vehicles for which we have only one target per color. In all cases, the estimated atmospheric profile is at the 50<sup>th</sup> percentile. Because we cannot do in-color detections for targets whose colors are unique, we instead create the ROC curves two different ways: 1) by calculating the  $P_{fa}$  considering only pixels in the class of automobiles; and 2) calculating the  $P_{fa}$  considering all background pixels. Our hypothesis is that automobile paints will bear spectral similarities to each other irrespective of color compared to other background materials.

We observe from Fig. 19 that the previously stated hypothesis is generally correct. The black lines represent detections against the entire background. For most percentiles of the distribution, the black lines are above the blue lines representing detections against only other automobile target pixels.

We observed earlier that the effect of atmospheric mis-estimation is often asymmetric. Likewise here in Fig. 19(a) and Fig. 19(b), the effect of underestimating atmospheric water vapor content when it is at the high end of the historical distribution is much more dramatic (and bad) than when we overestimate the water vapor content when it is at the low end of the distribution. We can explain this effect in terms of

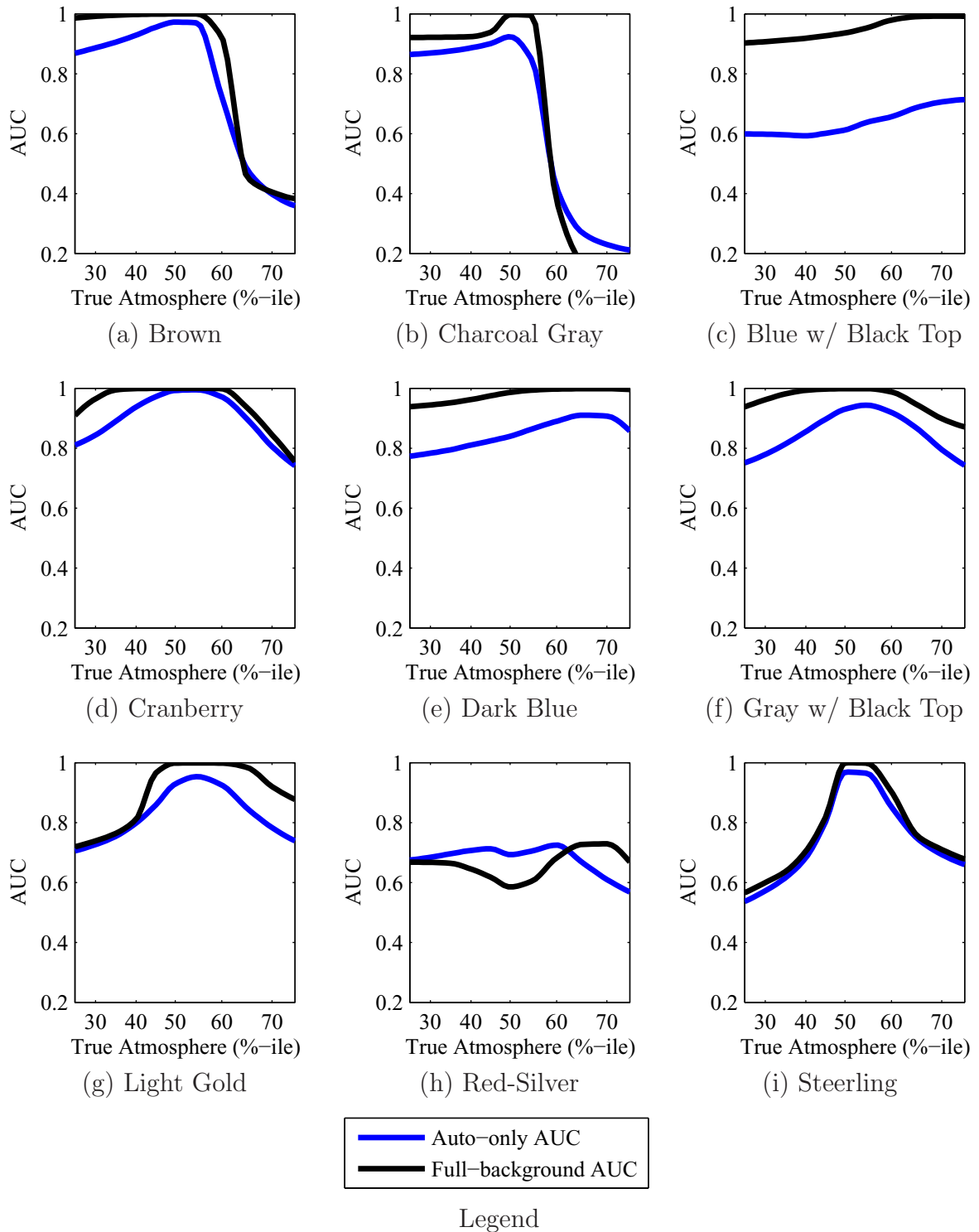


Figure 19: AUCs from AMF detection of automobiles of the indicated colors. We show results both from target detections against the entire image background (black) and against only other automobiles of all colors (blue).

the relative distribution of the target pixels in hyperspectral space with respect to that of the background, as we saw in our example illustrated in Section 3.3.2.

Finally, while we can see that the AUC tends to peak at true atmospheres at the 50<sup>th</sup> percentile, there are exceptions. Most notably in Fig. 19(c) and (e), we see that the best detection performance is when water vapor content is at its highest value. This, too, was predicted in Section 3.3.2.

In Fig. 20 and Fig. 21, we present results for automobiles for which there are multiple targets per color. In these graphs, the solid lines are AUC plots of in-color detections for the individual automobiles indicated in the plot legend. The dotted lines represent vertical averages of the AUC values for targets of that color for three different detections. The red dotted line is the average of the in-color detections (i.e., the average of the solid lines shown for each color). The blue dotted line is the average of the AUC for detections against only other automobile targets. The black dotted line is the average of the AUC for detections against the entire background. According to Fawcett [13], vertical averaging is most applicable when “comparing across model classes,” meaning using different types of detectors or different parameters (i.e., the covariance matrix) with the same detector. In contrast to threshold averaging, it requires controlling for  $P_{fa}$  across ROC curves; this we accomplished with interpolation. Threshold averaging is in our estimation inappropriate, since the specific AMF output values are not comparable across model classes.

As with the results presented in Fig. 19, our intuitions are generally confirmed. We see most AUC curves peaking for true atmospheres at the 50<sup>th</sup> percentile. We see that target detections are best when performed against the entire background and worst when performed only against other cars of the same color. This indicates that automobiles bearing similar colors are spectrally similar across the measured wavelengths and thus more difficult to distinguish using the AMF. As suggested by Fig. 21(d), detections against black objects are especially difficult; the resulting AUC curves are almost random in appearance.

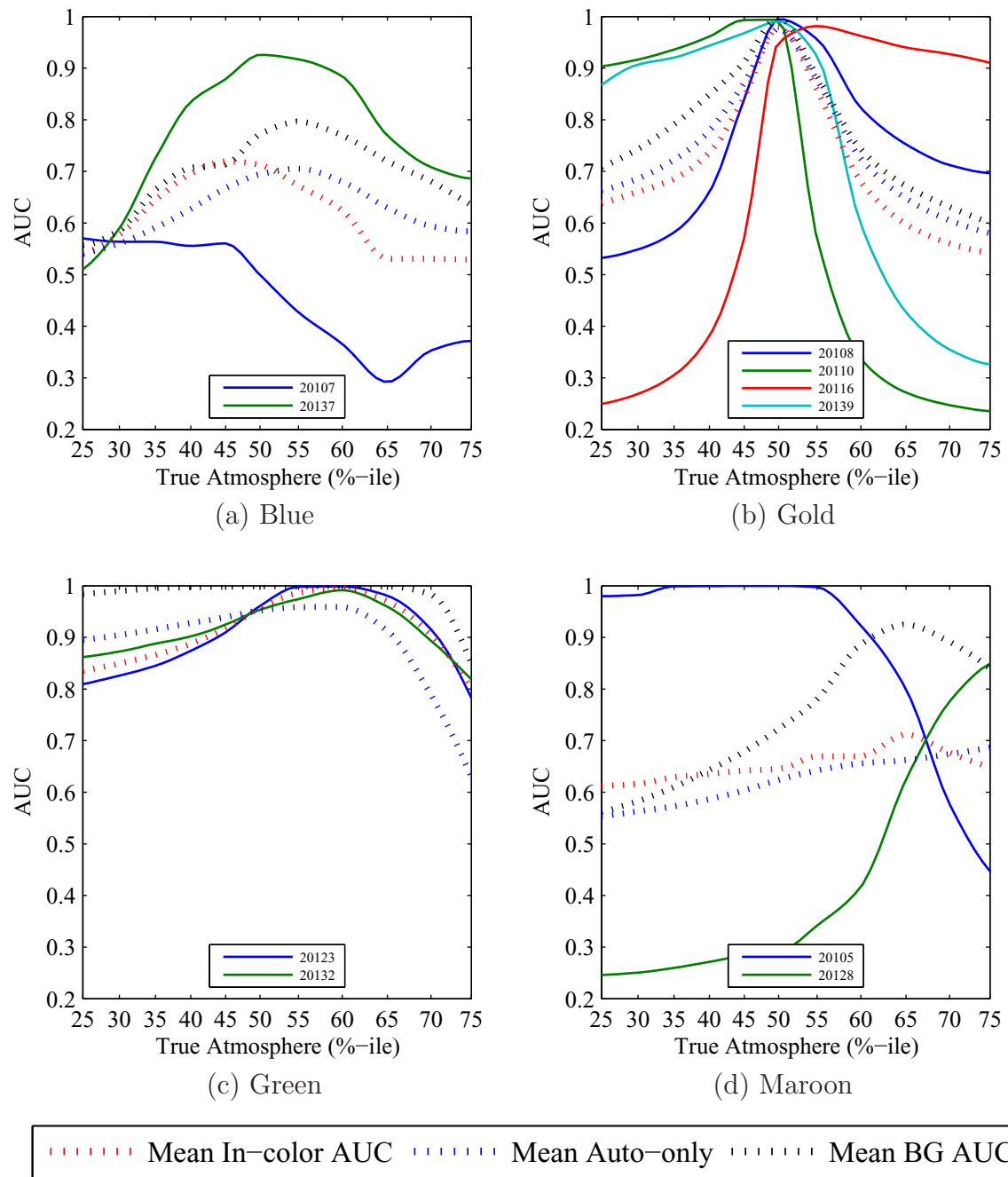


Figure 20: AUCs from AMF detection of automobiles of the indicated colors. We show results for the individual cars (solid lines), listed by material IDs, as detected against only cars of the same color. We also show the average of all cars of that color as detected against: only cars of the same color (red dotted); only the cars of all colors (blue dotted); and the entire background of the image (black dotted).

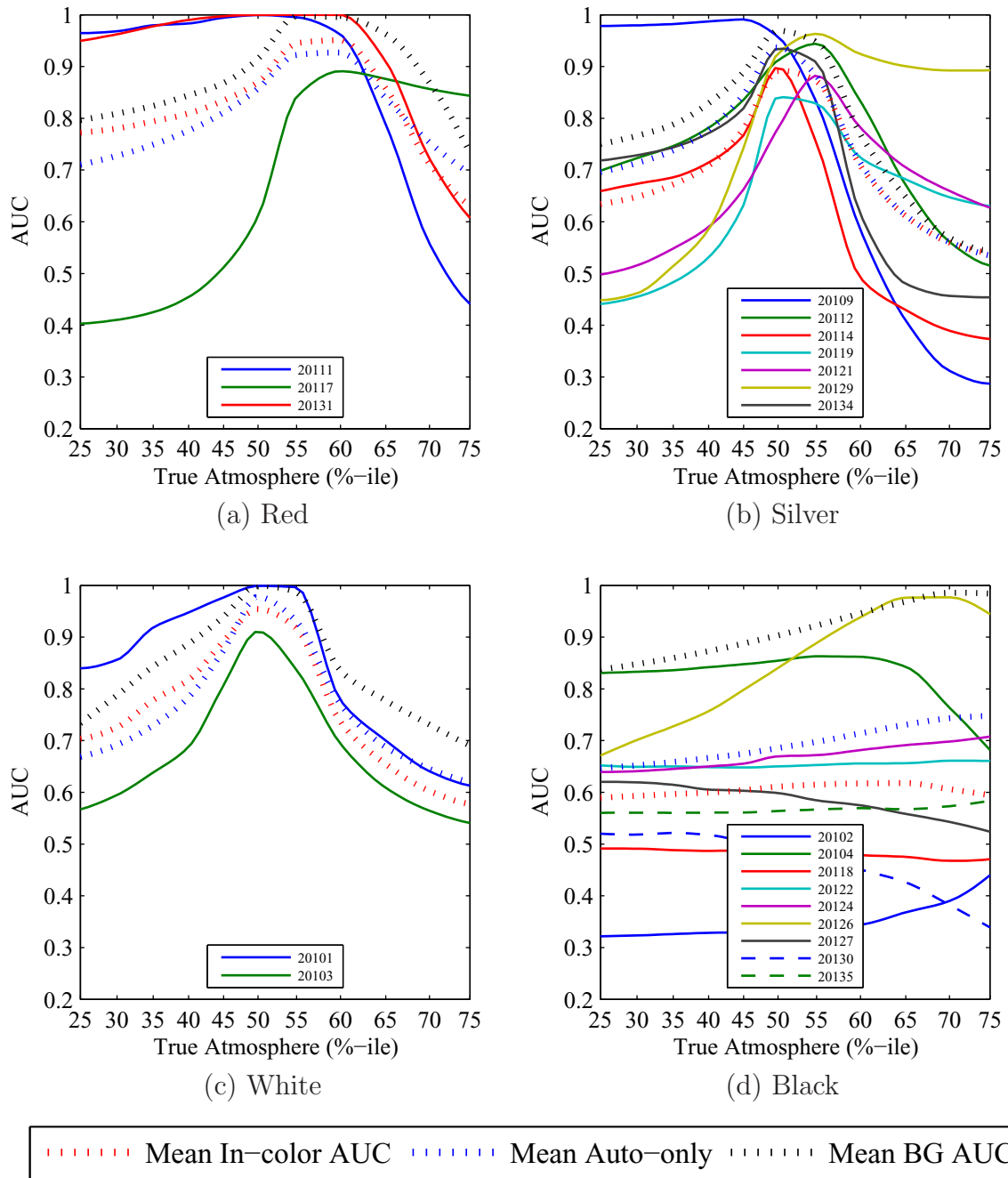


Figure 21: AUCs from AMF detection of automobiles of the indicated colors. We show results for the individual cars (solid lines), listed by material IDs, as detected against only cars of the same color. We also show the average of all cars of that color as detected against: only cars of the same color (red dotted); only the cars of all colors (blue dotted); and the entire background of the image (black dotted).

#### 4.4 AUC Contours as a Function of True Atmosphere and Estimated Atmosphere

We wish to explore the possibility suggested by our earlier plots: that the 50<sup>th</sup> percentile estimation may not maximize detector performance for all target types. To do this, we must examine not only variations in the *true* atmospheric profile but also variations in the *estimated* profile. We use contour plots where the contour lines indicate the AUC as a function of both the estimated atmosphere ( $x$ -axis) and the

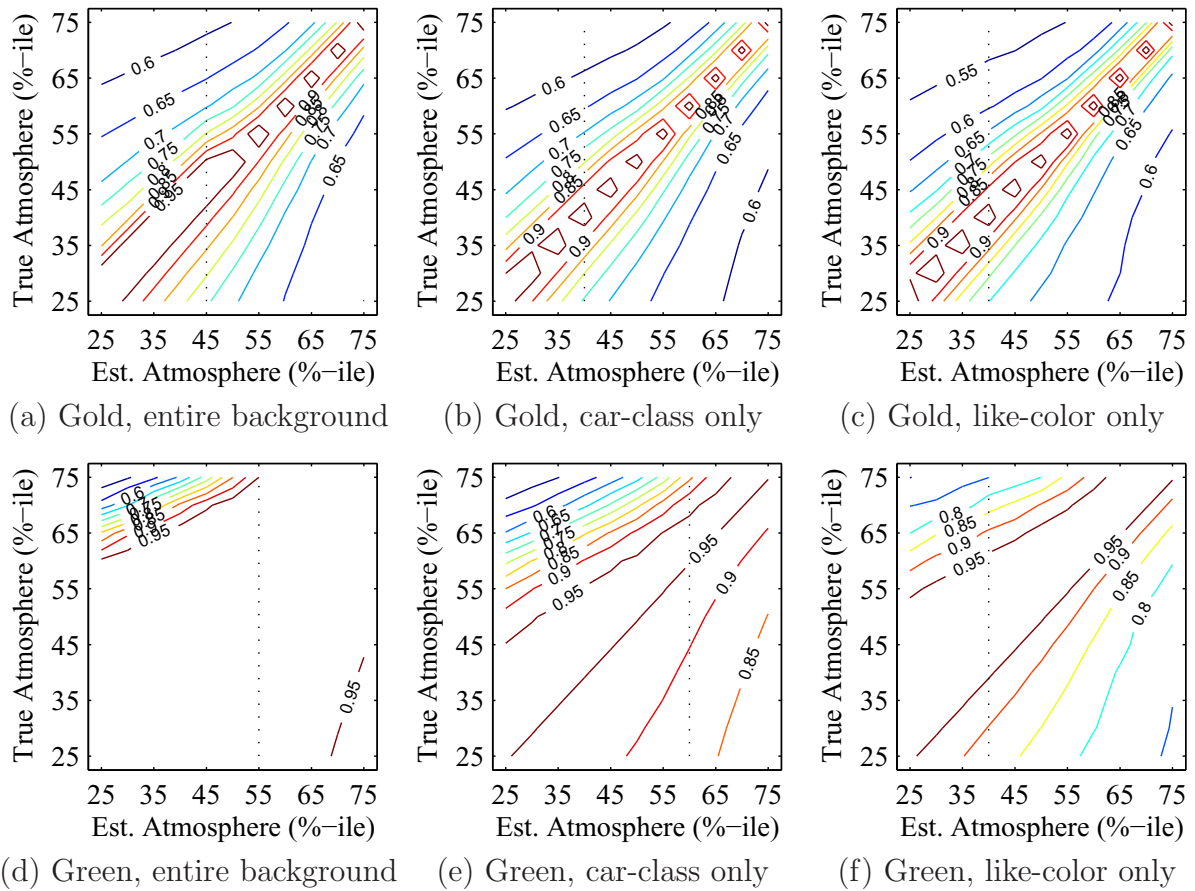


Figure 22: Contour plots of the average AUCs for AMF detection of the green, maroon, and red cars with the  $P_{fa}$ 's calculated from false alarms generated by all background pixels, automobile pixels only, and like-color automobile pixels. We vary both the “true” image illumination ( $y$ -axis) and the estimated illumination ( $x$ -axis) by their percentiles in the historical distribution at the target site. Note that the estimated illumination percentile that maximizes the AUC averaged across all possible true illumination percentiles is indicated by the black dotted line.

true atmosphere ( $y$ -axis). In Fig. 22 and Fig. 23, we consider panels that represent the green, gold, white, and silver automobiles. (The AUC contour plots for all other automobile colors are presented in Appendix D.) We plot the average AUC contours for all cars of each color for detections against the entire background (first column), all automobiles (second column) and same-color automobiles (third column). In all graphs, we use a vertical dotted line to indicate the estimated atmosphere that maximizes the average AUC for all true atmospheres, i.e.,

$$AUC_{avg} = \frac{1}{11} \sum_{\%} AUC(\%), \% = \{25, 30, 35, \dots, 75\} \quad (36)$$

There are several generalizations we can make from these graphs. First, we see that the contour lines are denser in the upper right hand corner of the graph, indicating greater spectral variation in reaction to changes in atmospheric water vapor content at high humidities than variation at low humidities, although this observation is mitigated by the non-linear relationship between the nominal percentile of the distribution and the underlying water vapor measurements. Second, we see that using the 50<sup>th</sup> percentile of the atmospheric profile distribution as the optimum estimation of water vapor content for purposes of target detection is the exception rather than the rule, and that the actual optimum percentile varies with the target. The examples in Fig. 22 and Fig. 23 are typical: the optimum values are just below the 50<sup>th</sup> percentile. More extreme cases can be found in Appendix D.

#### ***4.5 Probability of Detection ( $P_d$ ) at a Constant Probability of False Alarm ( $P_{fa}$ ): Contour Plots***

A possible objection to the use of the AUC as a performance metric is that it is inevitably influenced by regions of the ROC curve with no operational utility. For instance, while the  $P_d$  might be quite high for  $P_{fa}$ 's between, say, 10% and 100%, no operational detection system would be able to make use of data with false alarm rates

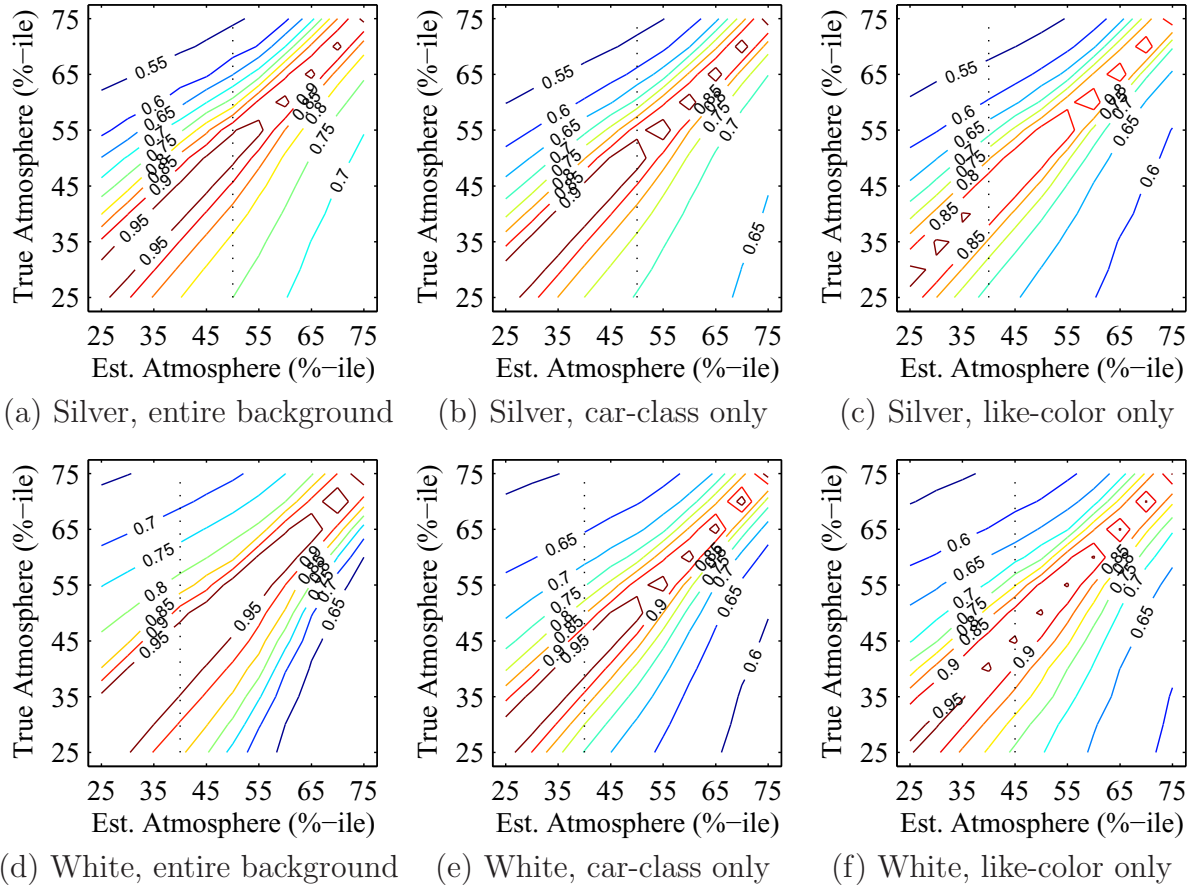


Figure 23: Contour plots of the average AUCs for AMF detection of the silver and white cars with the  $P_{fa}$ 's calculated from false alarms generated by all background pixels, automobile pixels only, and like-color automobile pixels. We vary both the “true” image illumination ( $y$ -axis) and the estimated illumination ( $x$ -axis) by their percentiles in the historical distribution at the target site. Note that the estimated illumination percentile that maximizes the AUC across all possible true illumination percentiles is indicated by the black dotted line.

of that magnitude when the in-scene target density is well less than  $10^{-3}$ , as it is in our example.

To overcome this problem, we substitute in our contour plots of the AUC with the  $P_d$  at a constant  $P_{fa} = 0.05$ . The results of this substitution are shown for the gold, maroon, silver, and white automobiles in Fig. 24 and Fig. 25. (All other results are shown in Appendix E.)

We see from these results that many of our conclusions from using the AUC are confirmed. Again, the contour lines are denser in the upper right hand corner of the graph, indicating greater spectral variation in reaction to changes in atmospheric water vapor content at high humidities than variation at low humidities. Again also we see that using the 50<sup>th</sup> percentile of the atmospheric profile distribution as the optimum estimation of water vapor content for the purpose of detection is the exception rather than the rule, and that the actual optimum percentile varies with the target. We see that while the magnitude of this offset from the 50<sup>th</sup> percentile varies with material type, the direction of the offset for a specific material type tends to be consistent across different methods of calculation (i.e., whether we are detecting targets among like-colors, the overall class of automobiles, or the entire background). The reason for these offsets has to do with the relative relationships between the target's location in hyperspectral space relative to that of various background materials.

In Table 4, we present the  $P_d$  and AUC-maximizing atmospheric percentile for each automobile color, as well as the standard deviation of those percentiles. We see that while there are exceptions, most of the optimum parameter assumptions are on the low side of the atmospheric water vapor distribution. We also see from the column of low standard deviations that the best assumption for each automobile panel is stable across multiple measurements (the detection of red car among other red cars being the significant outlier); this is surprising given the spectral dissimilarities among different automobile colors and between the cars and the background. Note that the data for the automobile colors whose optimums are at the tails (25<sup>th</sup> and 75<sup>th</sup> percentiles) of the distributions considered are likely unreliable, since there are probably lower or higher distributions at which the true optimum would be found. Black, blue w/black top and charcoal gray are colors likely in this category.

In Fig. 26, we present normalized histogram plots of optimum percentiles. The  $P_d$  and AUC plots for detections against the entire background and the automobile class only include results for all automobiles, while the detections against only other like-color cars only include results for which we have multiple cars of the same color.

Again, our earlier intuitions from Table 4 is confirmed: we see that the optimum atmospheric assumptions for purposes of target detection are in the lower half of the distribution of atmospheric water vapor.

#### 4.6 Summary of Results

This chapter demonstrates that a high level of target dependence governs results across metrics. In Section 4.2, we observed that the particular target governed the

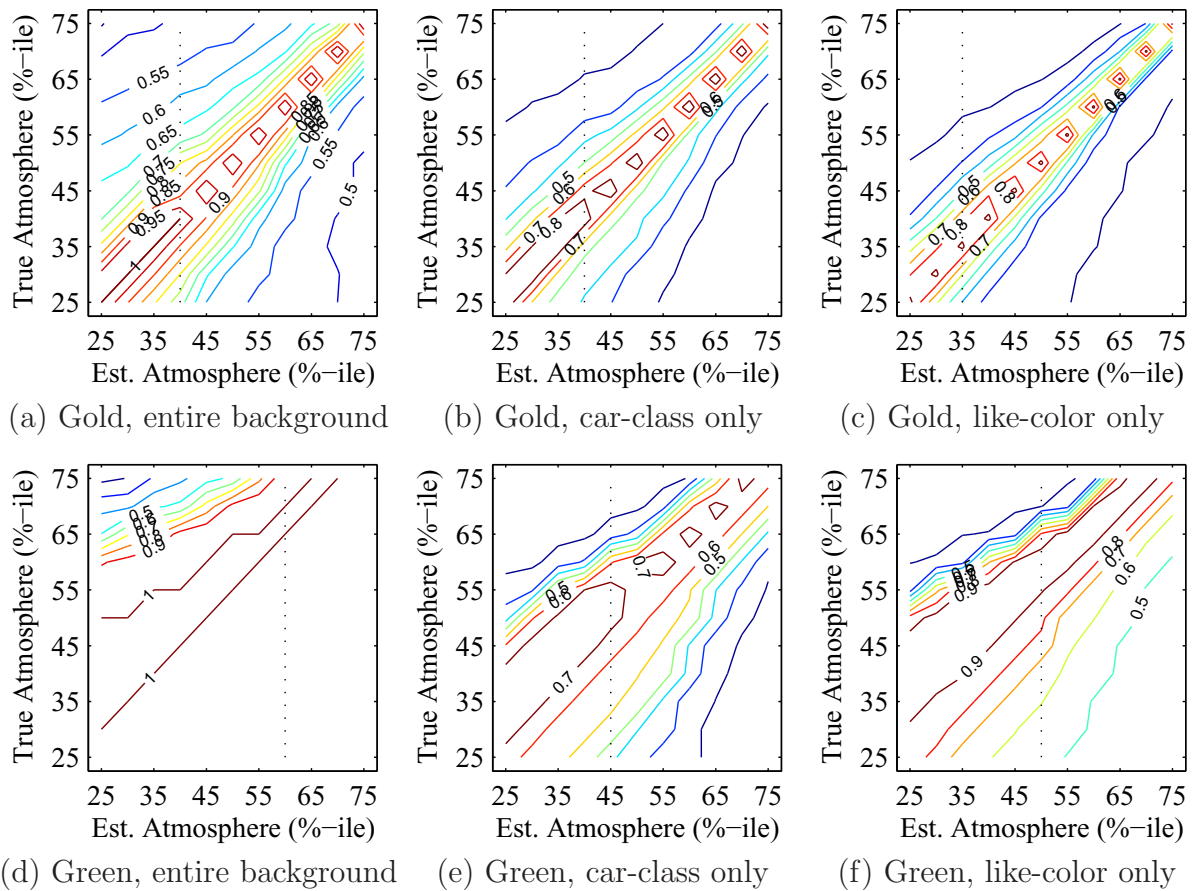


Figure 24: Contour plots of the average ROC  $P_d$  when  $P_{fa} = 0.05$  for AMF detection of the green cars with the  $P_{fa}$ 's calculated from false alarms generated by all background pixels, automobile pixels only, and like-color automobile pixels. We vary both the “true” image illumination ( $y$ -axis) and the estimated illumination ( $x$ -axis) by their percentiles in the historical distribution at the target site. Note that the estimated illumination percentile that maximizes the  $P_d$  across all possible true illumination percentiles is indicated by the black dotted line.

degree to which our best detector performance could be found at the 50<sup>th</sup> percentile atmospheric estimation. We confirmed this result in Section 4.3, where we also observed that detection of specific cars was more difficult among like-colored cars than among either the entire car class or the entire background. Finally, in Section 4.4 and Section 4.5, we confirmed all of these results with the use of contours of the AUC and  $P_d$ , noting that we could obtain detection optimizations by varying our atmospheric assumptions depending on the specific target.

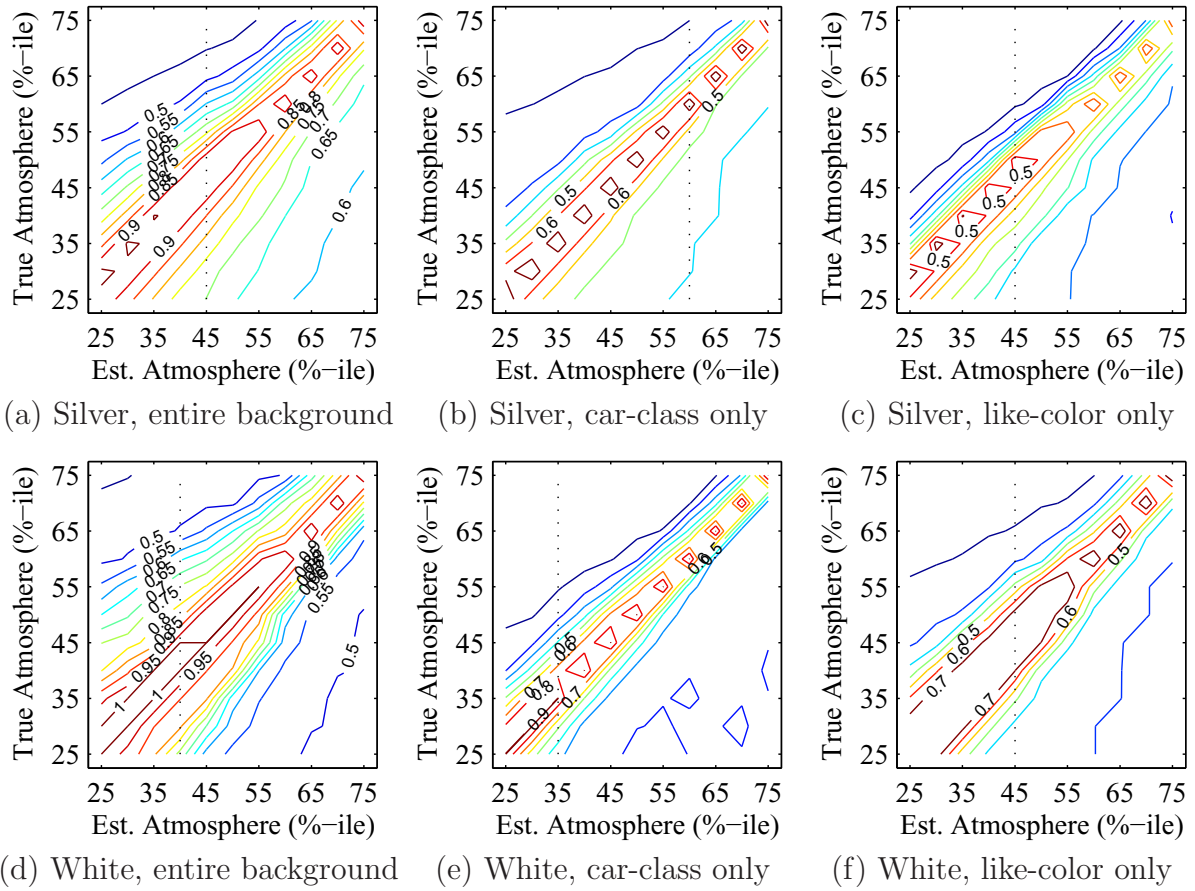


Figure 25: Contour plots of the average ROC  $P_d$  when  $P_{fa} = 0.05$  for AMF detection of the silver and white cars with the  $P_{fa}$ 's calculated from false alarms generated by all background pixels, automobile pixels only, and like-color automobile pixels. We vary both the “true” image illumination ( $y$ -axis) and the estimated illumination ( $x$ -axis) by their percentiles in the historical distribution at the target site. Note that the estimated illumination percentile that maximizes the  $P_d$  across all possible true illumination percentiles is indicated by the black dotted line.

This observation may come as no surprise, given that the reflectance spectra of different automobiles differ in the regions of the solar spectrum they emphasize. Meanwhile, the atmospheric variation also affects the illumination in specific spectral regions. When the regions of emphasis overlap the regions of variation, this results in decreased signal to noise ratio (SNR) and ultimately hinders detection.

We point out here that the considered range of atmospheric variation under the conditions described in Section 3.4.1 is very narrow and represents the most optimistic scenario for knowing the true historic range. None of the standard atmospheric profiles employed by MODTRAN (e.g., “mid-lat summer,” “U.S. Standard Atm,” etc.) lies within that range. It is anticipated that, based on the results presented here, the use

Table 4: Performance maximizing atmospheric parameter assumptions for AMF target detection in percentile of the distribution. In the header line, “BG” indicates the detection was performed against the entire background, “AO” indicates the detection was performed against only the class of automobiles, and “CO” indicates the detection was performed against only cars of the same color. Where the “CO” column is empty, there is only one car of that color in our data set. The “Stddev” column shows the standard deviation of the  $P_d$  and AUC values for each auto color.

Auto Color	$P_d(P_{fa} = 0.05)$			AUC			Stddev
	BG	AO	CO	BG	AO	CO	
black	25	25	25	25	25	30	1.86
blue	35	30	40	25	35	45	6.46
gold	40	40	35	45	40	40	2.89
green	50	45	50	55	60	40	6.46
red	25	40	70	25	25	25	16.58
silver	40	35	45	40	35	55	6.87
white	45	60	45	50	50	40	6.24
blue w/black top	25	25		25	25		0
brown	70	75		70	70		2.17
charcoal gray	75	75		75	75		0
cranberry	45	35		50	45		5.45
dark blue	40	25		35	30		5.59
gray	55	40		55	50		6.12
gray w/black top	40	30		45	40		5.45
light gold	30	40		30	35		4.15
red/silver	60	55		55	60		2.50
sterling	30	30		30	30		0

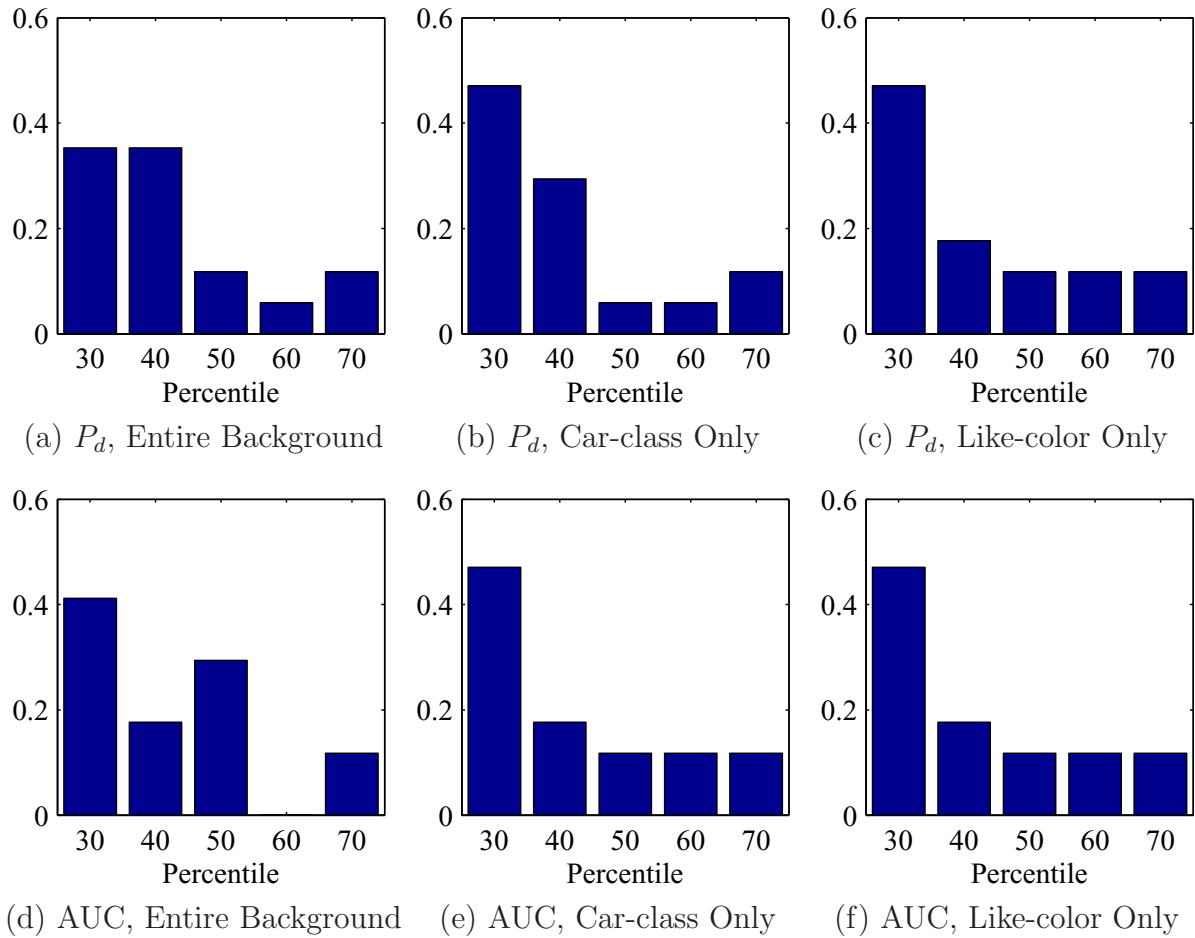


Figure 26: Normalized histograms of the optimum atmospheric water vapor profile percentile for use in radiative transfer atmospheric correction for purposes of target detection with the AMF. The metrics are the  $P_d$  when  $P_{fa} = 0.05$  and the AUC for detection against the entire background, the class of all automobiles, and like-color automobiles.

of such atmospheres would produce quite poor results in general. These atmospheres constitute continent-wide seasonal averages, and in any case do not take into account various climatological shifts in the atmospheric parameters, such as  $CO_2$  and  $H_2O$  levels.

## V. Conclusion

### 5.1 Summary

Our goal with this dissertation is to characterize the detection error of the Adaptive Matched Filter (AMF) output as a distribution dependent on the estimation of the atmospheric parameters. In the prospectus submitted to the committee, we proposed three specific objectives:

- Reconcile, to an order of magnitude, the solar radiances between PLEXUS MODTRAN and DIRSIG.
- Characterize the atmospheric profiles, not by percentiles, but by some weighted measure of the differences between their actual water vapor content in the boundary layer.
- Develop a relationship between the input error, as defined by the difference between atmospheric profiles, and two measures of the output error: the Bhattacharyya coefficient between the AMF output distributions and the change in the detection performance as measured by the AUC.

We have accomplished all three of these objectives.

The problems with both MODTRAN and DIRSIG involved the use of the user-defined atmospheric profiles. The profiles as provided by LEEDR gave the atmospheric parameters in units of altitude above the local ground level (AGL); however, the profiles as expected by MODTRAN (and, by extension, DIRSIG and PLEXUS) had altitude units above mean sea level (MSL). Our failure to adjust these altitudes meant that we had been giving altitudes to MODTRAN that it interpreted as being underneath the ground. This resulted in a critical error, and one which the DIRSIG and PLEXUS TAPE5 parsers handled differently, with dramatically different outputs.

As shown in Fig. 7, The Euclidean distance between the profiles of several measures of atmospheric water vapor content give us a highly linear relationship with Euclidean distance between the atmospheric transmission – and therefore sensor-reaching radiance and calculated target reflectance – generated by those profiles. Since

the dew point temperature relationships are the most linear, this is the measure we use in subsequent comparisons.

We have shown that the greater the error between the estimated atmospheric profile and the actual profile under which the image was acquired, the greater the difference between the outputs of the AMF as measured by the Bhattacharyya coefficient and, in general, the greater the error in detector performance as measured by the ROC and the AUC. We have shown that the size of these errors is heavily target dependent, specifically on its spectral properties. We have shown by our use of contour plots that, again depending on the target, we can often improve detector performance by assuming other than the median atmospheric conditions, given our inherent uncertainty about the actual water vapor content at the time of the image.

## 5.2 Contributions

As the dearth of references in our background literature review indicates, very little prior work has been done in the area of evaluating the effect of atmospheric profile variation on detector performance. This dissertation makes several unique contributions:

- A characterization along multiple metrics of the variable nature of the AMF distribution and rates of detection as a function of changing water vapor content along the atmospheric profile;
- An illustration of the dependence on specific target spectra of this effect; and
- The use of contour plots of the AUC and  $P_d$  to identify superior atmospheric assumptions for the purpose of target detection.

The operational utility of these findings is readily apparent. Mission planners and target intelligence officers will welcome the opportunity to improve their ability to detect targets at lower rates of false-positives, particularly when that target is singular in nature and decoys easy to deploy. This is especially true when, for instance,

a quality of actionable intelligence would be to distinguish a particular automobile (carrying adversaries) from other like-color automobiles (carrying neutrals).

### ***5.3 Possibility of Future Work***

Directions for future research would be to measure the effects under further variation in atmospheric parameters. Our research considers variation under the “best case scenario” when detailed atmospheric profile distributions are known for time of day and time of year at a specific location. We could consider the effect of greater variation when we are required to use regional, seasonal or daily average distributions.

We could expand the range of atmospheric parameters to include aerosols in the limited visibility case, considering the effect of few and scattered clouds, fog, and rain.

We could check to see if the results are consistent using alternative methods of feature selection and the number of features retained. For the purpose of these experiments, we first culled our spectra of the water vapor absorption bands around 1.4 and 1.9 microns. However, our choices as to the cutoff criteria are somewhat arbitrary, and it would be useful to check the results using other methods.

A further area of inquiry might be to consider the high level of variation in the reconstructed reflectances of Appendix A and try to use them to determine atmospheric water vapor, given known in-scene targets.

Another area of research would be to validate our conclusions against actual imagery. Use a representative background to model the detection of particular targets in-scene, and then compare our performance to actual detection under various atmospheric assumptions.

Finally, an interesting extension to the current work is to consider other target detection schemes to determine, under what atmospheric conditions, which detection scheme should be used?

## Bibliography

1. "Spectra for the 41 automobiles were collected by the Sensors Exploitation Research Group, Department of Electrical and Computer Engineering, Air Force Institute of Technology and the Multispectral branch, Air Force Research Laboratory Sensors Directorate for work sponsored by Dr. Devert Wicker in AFR-L/Ryat, the ATR division of AFRL/Ry."
2. "Private Conversation with Dr. Steven Fiorino", May 2009.
3. Adams, N. M. and D. J. Hand. "Improving the Practice of Classifier Performance Assessment". *Neural Computation*, 12(2):305–311, 2000.
4. Ahmad, Z. and R. Fraser. "Satellite measurements of cloud reflectance and optical thickness". *Advances in Space Research*, 2(6):29–34, 1982.
5. Borel, C. "Surface Emissivity and Temperature Retrieval for a Hyperspectral Sensor". *Geoscience and Remote Sensing Symposium Proceedings*, volume 1, 546–549. IGARSS, IEEE International, 1998. ISBN 0-7803-4403-0.
6. Borel, C. "ARTEMISS - an Algorithm to Retrieve temperature and Emissivity from HyperSpectral Thermal Image Data". *28th Annual GOMACTech Conference, Hyperspectral Imaging Session*. March 2003.
7. Borel, C.C. "Iterative Retrieval of Surface Emissivity and Temperature for a Hyperspectral Sensor". *First JPL Workshop on Remote Sensing of Land Surface Emissivity*. 1997.
8. Bradley, Andrew P. "The use of the area under the ROC curve in the evaluation of machine learning algorithms". *Pattern Recognition*, 30(7):1145 – 1159, 1997.
9. Burger, James and Paul Geladi. "Hyperspectral NIR imaging for calibration and prediction: a comparison between image and spectrometer data for studying organic and biological samples". *Analyst*, 131:1152–1160, 2006.
10. Carvalho, O.B. and P.R. Meneses. "Spectral Correlation Mapper (SCM): An improvement on the spectral angle mapper (SAM)". *Proceedings of NASA JPL AVIRIS Workshop*. 2000.
11. d'Almeida, G., P. Koepke, , and E. Shettle. *Atmospheric Aerosols: Global Climatology and Radiative Characteristics*. A. Deepak Publishing, 1991.
12. Elachi, C. and J. Van Zyl. *Introduction to the Physics and Techniques of Remote Sensing (2nd Edition)*. John Wiley and Sons, 2006.
13. Fawcett, T. "ROC Graphs: Notes and Practical Considerations for Researchers", 2004.
14. Fawcett, Tom. "An introduction to ROC analysis". *Pattern Recognition Letters*, 27(8):861 – 874, 2006.

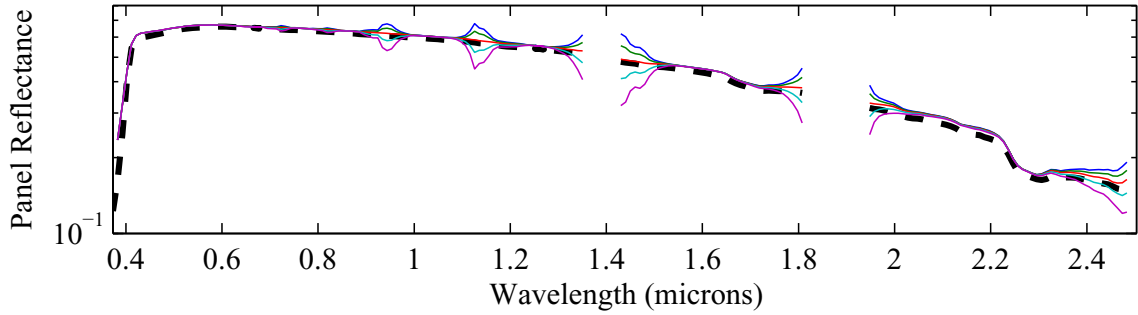
15. Fiorino, S.T., R. Bartell, M. Krizo, G. Caylor, K. Moore, T. Harris, and S. Cusumano. "A first principles atmospheric propagation and characterization tool: the laser environmental effects definition and reference (LEEDR)". *SPIE Proceedings*, volume 6878, 122–124. Feb 2001.
16. Fiorino, S.T., R. Bartell, M. Krizo, K. Moore, and S. Cusumano. "Validation of a Worldwide Physics-Based, High Spectral Resolution Atmospheric Characterization and Propagation Package for UV to RF Wavelengths". S.M. Hammel, A.M.J. van Eijk, and M.A. Vorontsov (editors), *Atmospheric Optics: Models, Measurements, and Target-in-the-Loop Propagation II*, volume 7090. SPIE, Aug 2008.
17. Fiorino, S.T., R.J. Bartell, G.P. Perram, D.W. Bunch, L.E. Gravley, C.A. Rice, Z.P. Manning, and M.J. Krizo. "The HELEEOS Atmospheric Effects Package: A Probabilistic Method for Evaluating Uncertainty in Low-Altitude High Energy Laser Effectiveness". *Journal of Directed Energy*, 1(4):347–359, 2006.
18. Gao, B., K. Heidebrecht, and A. Goetz. "Derivation of Scaled Surface Reflectances from AVIRIS Data". *Remote Sensing of the Environment*, 1:546 – 549, Jul 1998.
19. Gao, B., M. Montes, Z. Ahmad, and C. Davis. "An Atmospheric Correction Algorithm based on vector radiative transfer modeling for hyperspectral remote sensing of ocean color". *SPIE Conference on Imaging Spectrometry V*, volume 3753, 70–78. SPIE, July 1999.
20. Goodenough, D.G., A. Dyk, T. Han, A. Jazayeri, and J. Li. "Impacts of lossy compression on hyperspectral products for forestry". *Proceedings of IEEE International Geoscience and Remote Sensing Symposium (IGARSS), 2004.*, volume 1, 465–468. Sept 2004.
21. Green, R. O., D. A. Roberts, and J. E. Conel. "Characterization and Compensation of the Atmosphere for the Inversion of AVIRIS Calibrated Radiance to Apparent Surface Reflectance". *Summaries of the 6th Annual JPL Airborne Geoscience Workshop, AVIRIS Workshop*, volume 1, 135–146. Pasadena, CA, March 1996.
22. Gruninger, J., M. Fox, J. Lee, A. Ratkowski, and M. Hoke. "Use of the Vis-SWIR to Aid Atmospheric Correction of Multispectral and Hyperspectral Thermal Infrared (TIR) Imagery: The TIR Model". *SPIE Proceeding, Imaging Spectroscopy VIII*, volume 4816-11. July 2002.
23. Hand, David J. and Robert J. Till. "A Simple Generalisation of the Area Under the ROC Curve for Multiple Class Classification Problems". *Machine Learning*, 45:171–186, 2001. 10.1023/A:1010920819831.
24. Hastie, Trevor, Robert Tibshirani, and Jerome Friedman. *The Elements of Statistical Learning, Second Edition: Data Mining, Inference, and Prediction*. Springer Series in Statistics. Springer, 2nd edition, 2009.

25. Healy, G. and D. Slater. "Models and Methods for Automated Material Identification in Hyperspectral Imagery Acquired Under Unknown Illumination and Atmospheric Conditions". *IEEE Transactions on Geoscience and Remote Sensing*, 37(6):27062717, Nov 1999.
26. Hege, E. Keith, Dan O'Connell, William Johnson, Shridhar Basty, and Eustace L. Dereniak. "Hyperspectral imaging for astronomy and space surveillance". *SPIE Proceedings*, 5159:380, 2004.
27. Holte, Robert C. and Chris Drummond. "Cost-sensitive classifier evaluation". *Proceedings of the 1st international workshop on Utility-based data mining, UBDM '05*, 3–9. ACM, New York, NY, USA, 2005.
28. Ientilucci, S.D., E.J.; Brown. "Advances in Wide Area Hyperspectral Image Simulation". *Unpublished*, 2009.
29. Johnson B. R., S. J. Young. *In Scene Atmospheric Compensation: Application to SEBASS Data Collected at the ARM Site*. Technical report, 1998.
30. Kacenjjar, S., S. Esposito, and F. Crawford. "Atmospheric Profile Variability Impact on the Performance of Hyperspectral Remote Sensing Detection Systems". *Geoscience and Remote Sensing Symposium, 2001. IGARSS '01. IEEE 2001 International*, volume 4, 1829–1831 vol.4. IEEE, 2001.
31. Keane, Robert E., Robert Burgan, and van Wagendonk. "Mapping wildland fuels for fire management across multiple scales: Integrating remote sensing, GIS, and biophysical modeling". *International Journal of Wildland Fire*, 10:301–319, Jan 2001.
32. Kidder, Stanley Q. and Thomas H. Vonder Haar. *Satellite Meteorology: an Introduction*.
33. Landgrebe, D. *Signal Theory Methods in Multispectral Remote Sensing*. John Wiley and Sons, Inc., 2003.
34. Manolakis, D. and G. Shaw. "Detection algorithms for hyperspectral imaging applications". *IEEE Signal Processing Magazine*, 19(1):29–43, Jan 2002.
35. Mendenhall, Michael J. *A Neural Relevance Model for Feature Extraction from Hyperspectral Images, and its Application in the Wavelet Domain*. Ph.D. thesis, Rice University, 2006.
36. Metternicht, Graciela, Lorenz Hurni, and Radu Gogu. "Remote sensing of landslides: An analysis of the potential contribution to geo-spatial systems for hazard assessment in mountainous environments". *Remote Sensing of Environment*, 98(2-3):284 – 303, 2005. ISSN 0034-4257.
37. "NASA JPL ASTER Spectral Library". <http://speclib.jpl.nasa.gov>.
38. "NOAA FSL Radiosonde Database". <http://www.fsl.noaa.gov>.

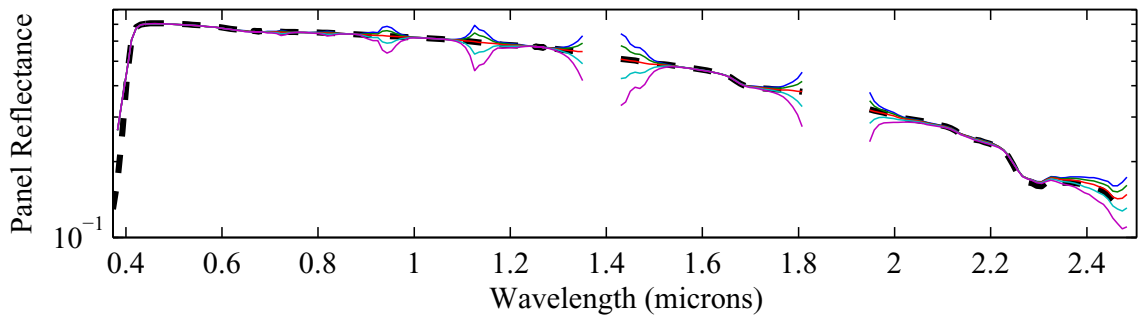
39. Petty, G.W. *A First Course in Atmospheric Radiation (2nd Edition)*. Sundog Publishing, 2006.
40. Provost, F. and P. Domingos. “Tree Induction for Probability-based Ranking”. *Machine Learning*, 199–215, 2003.
41. Robey, F., D. Fuhrmann, E. Kelly, and R. Nitzberg. “A CFAR Adaptive Matched Filter Detector”. *IEEE Transactions on Aerospace and Electronic Systems*, 28(1), Jan 1992.
42. Schott, J.R., S.D. Brown, R.V. Raqueno, H.N. Gross, and G. Robinson. “An advanced synthetic image generation model and its application to multi/hyperspectral algorithm development”. *Canadian Journal of Remote Sensing*, 25(2), Jun 1999.
43. Suen, P., G. Healey, and D. Slater. “The Impact of Viewing Geometry on Vision Through the Atmosphere”. *Eighth International Conference on Computer Vision (ICCV’01)*, volume 2, 454. ICCV, 2001.
44. Thacker, N. A., F. J. Aherne, and P. I. Rockett. “The Bhattacharyya Metric as an Absolute Similarity Measure for Frequency Coded Data”. *Kybernetika*, 34(4):363 – 368, 1998.
45. Utschick, W., P. Nachbar, C. Knobloch, A. Schuler, and J. A. Nossek. “The Evaluation of Feature Extraction Criteria Applied to Neural Network Classifiers”. *Proceedings of the International Conference on Document Analysis and Recognition (ICDAR)*, 315 – 318. 1995.
46. Vongsy, K. and M.J. Mendenhall. “A Comparative Study of Spectral Detectors”. *Hyperspectral Image and Signal Processing: Evolution in Remote Sensing (WHISPERS)*, Lisbon, Portugal, 2011, 1–4. March 2011.
47. Wiscombe, W. “Improved Mie Scattering Algorithms”. *Applied Optics*, 19:1505, May 1980.
48. Wu, Shaomin and Peter Flach. “A Scored AUC Metric for Classifier Evaluation and Selection”. *2nd Workshop on ROC Analysis in Machine Learning, ROCML05*. 2005.
49. Yarbrough, A.W., M.J. Mendenhall, and S.T. Fiorino. “Measuring the error between actual and estimated atmospheric and the effect on estimating reflectance profiles”. *Geoscience and Remote Sensing Symposium (IGARSS), 2010 IEEE International*, 3588–3591. July 2010.
50. Yarbrough, A.W., M.J. Mendenhall, and R.K. Martin. “The effects of atmospheric mis-estimation on hyperspectral-based adaptive matched filter target detection as measured by the Bhattacharyya coefficient”. *2010 2nd Workshop on Hyperspectral Image and Signal Processing: Evolution in Remote Sensing (WHISPERS)*, 1–4. June 2010.

## Appendix A. Spectral Signatures for All Automobiles

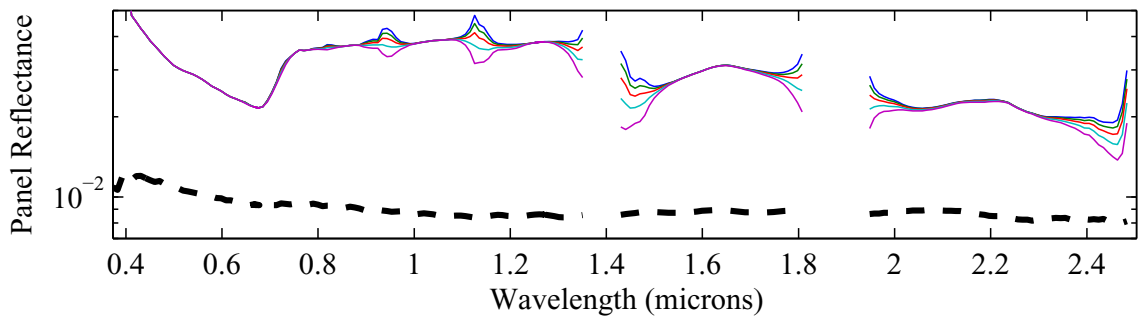
Shown here are the reflectance signatures of each of 41 automobiles, both as it appears in the spectral library (dashed line) and as it appears in the hyperspectral image as it has been reconstructed under the various atmospheric profiles (colored lines), given that the image itself was simulated under the 50<sup>th</sup> percentile of atmospheric water vapor distribution.



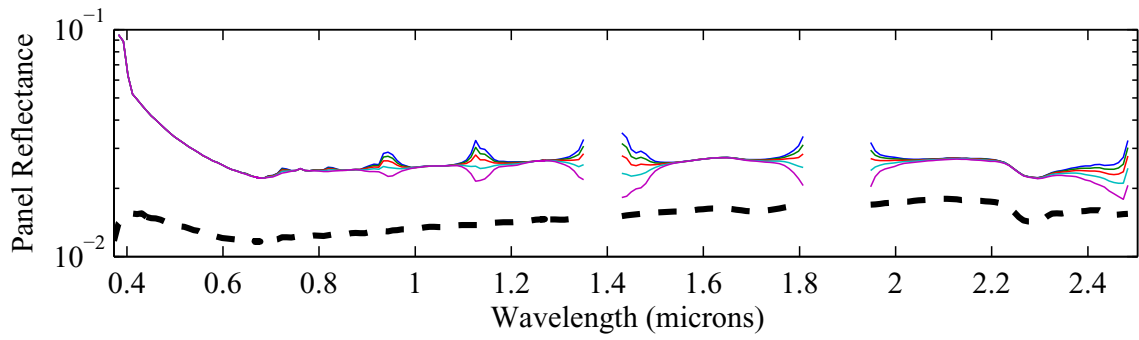
(a) White Car #20101



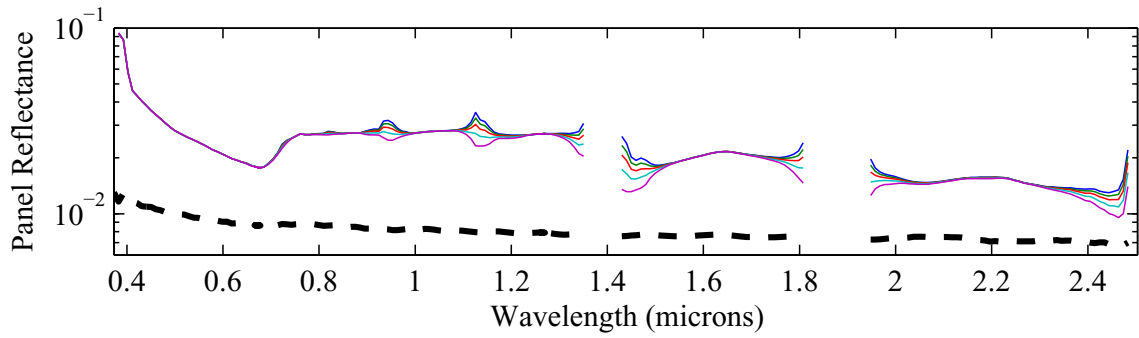
(b) White Car #20103



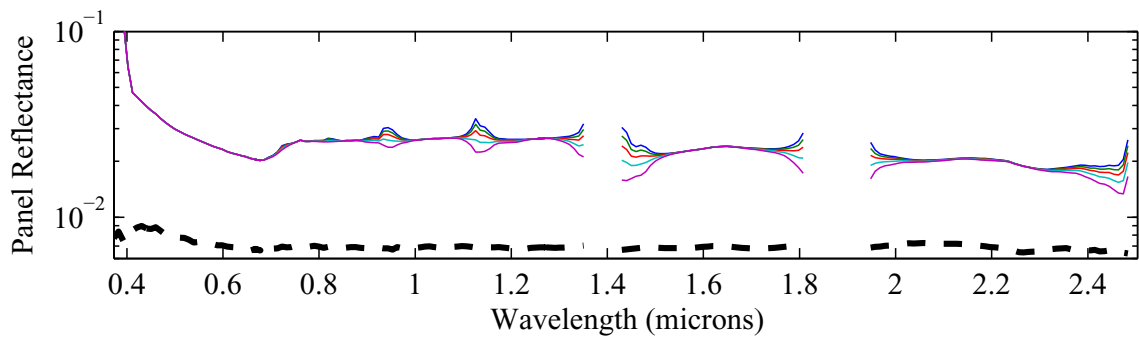
(c) Black Car #20102



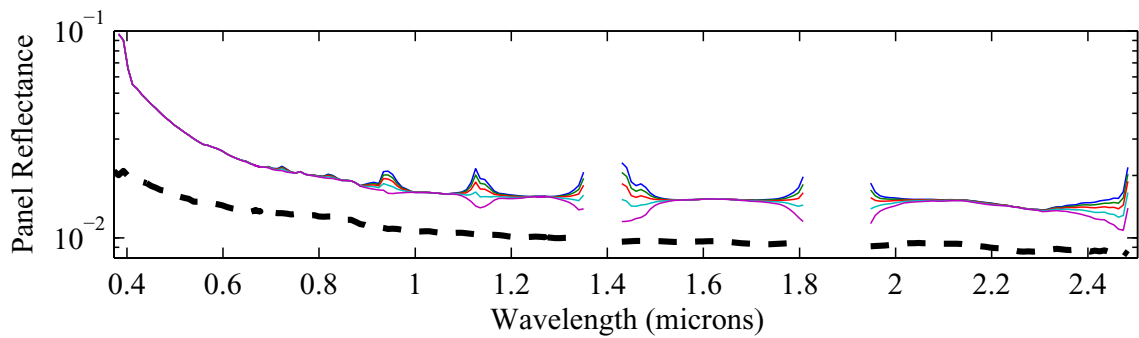
(d) Black Car #20104



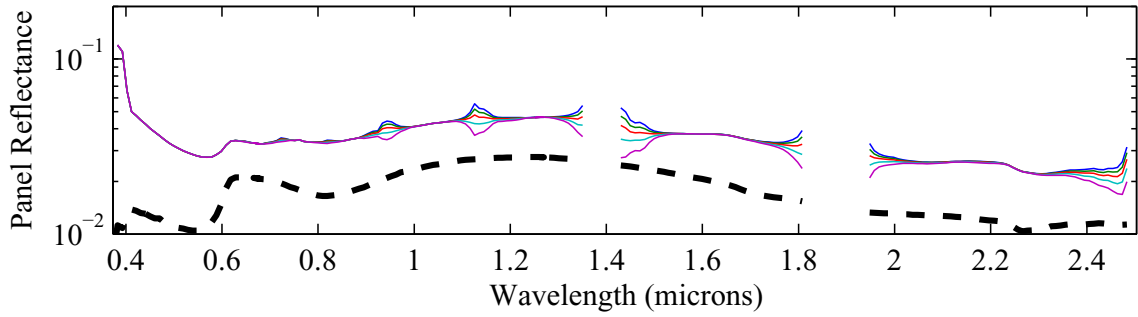
(e) Black Car #20118



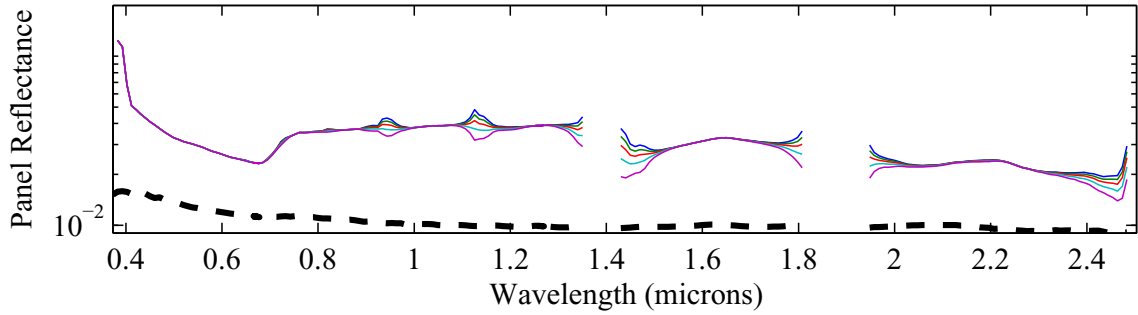
(f) Black Car #20122



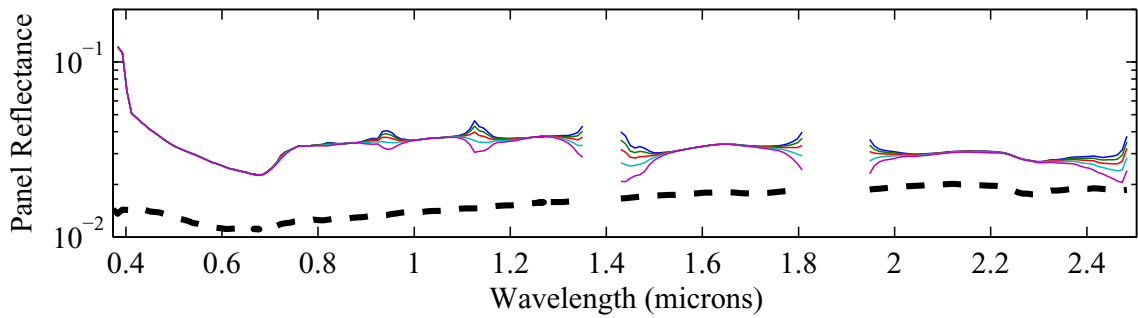
(g) Black Car #20124



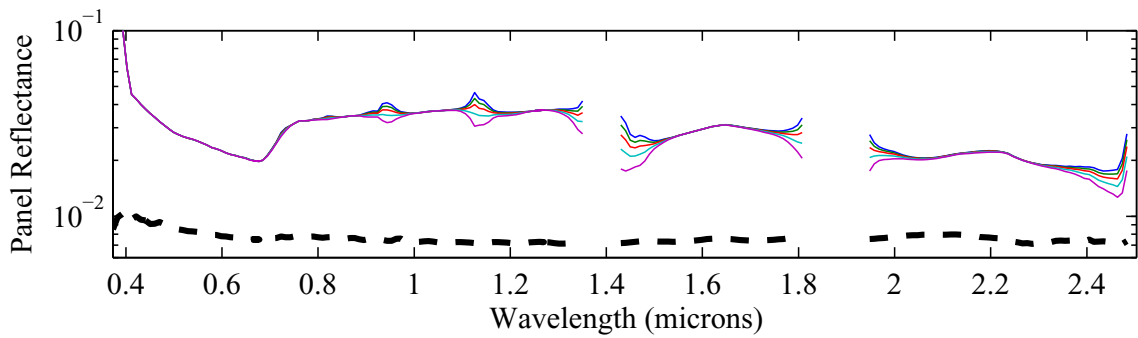
(h) Black Car #20126



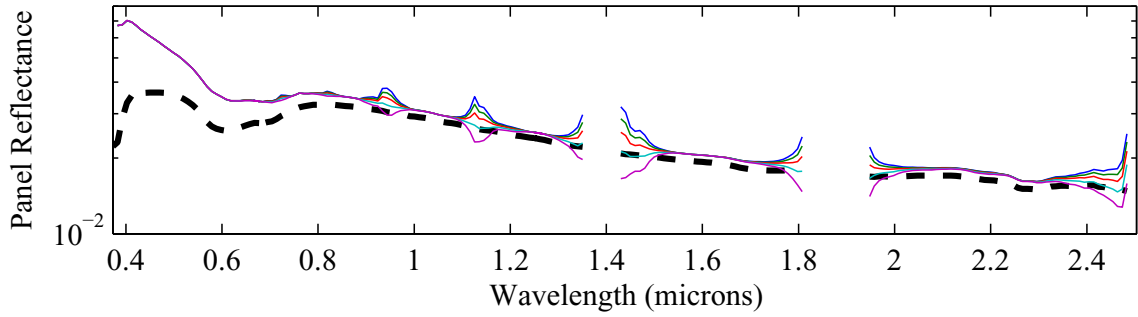
(i) Black Car #20127



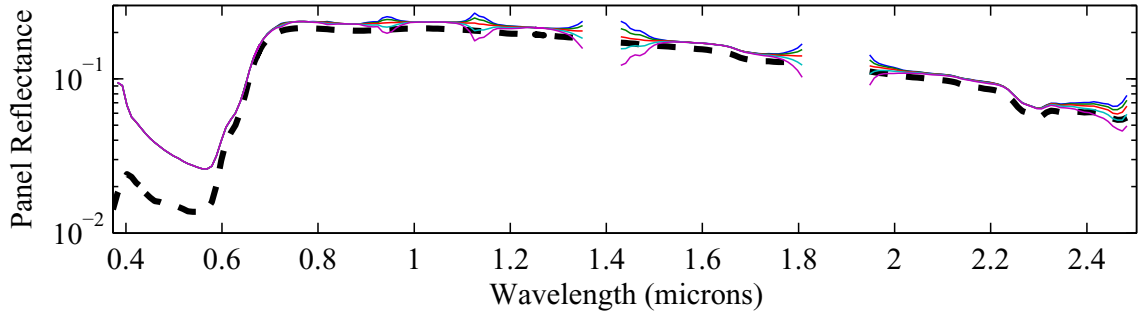
(j) Black Car #20130



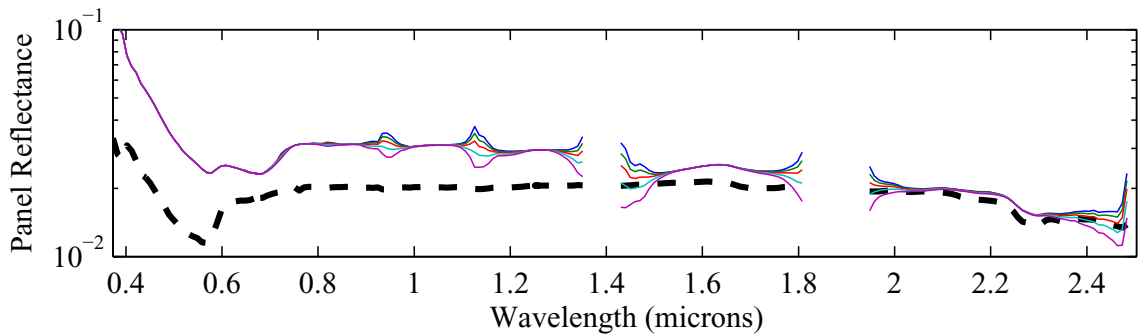
(k) Black Car #20135



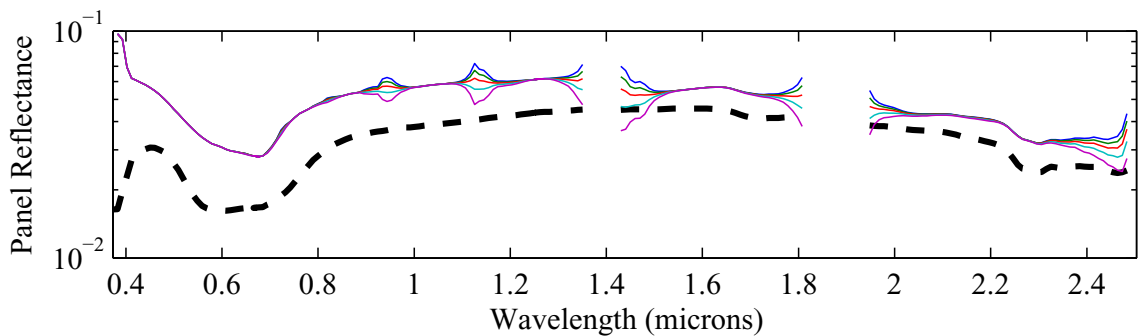
(l) Dark Blue Car #20106



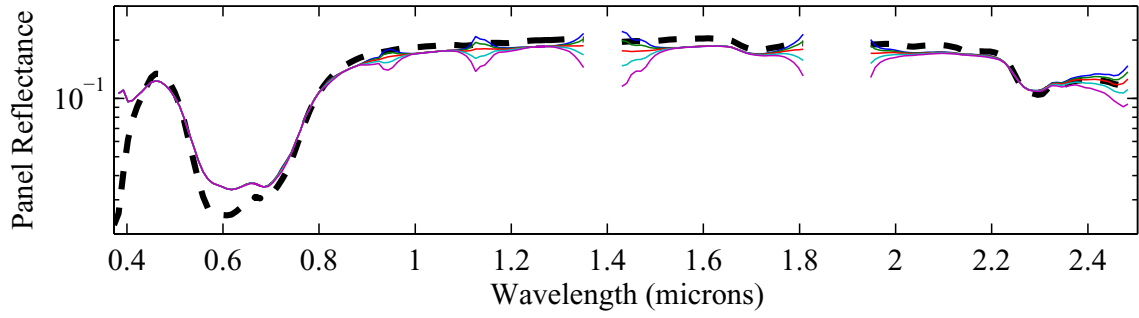
(m) Maroon Car #20105



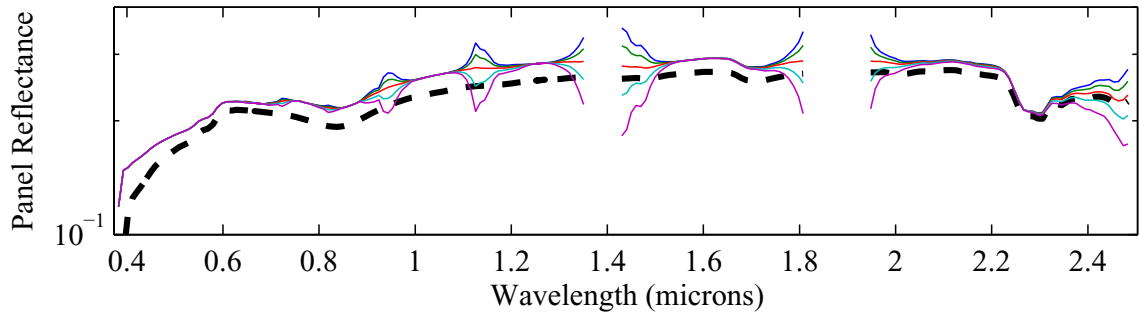
(n) Maroon Car #20128



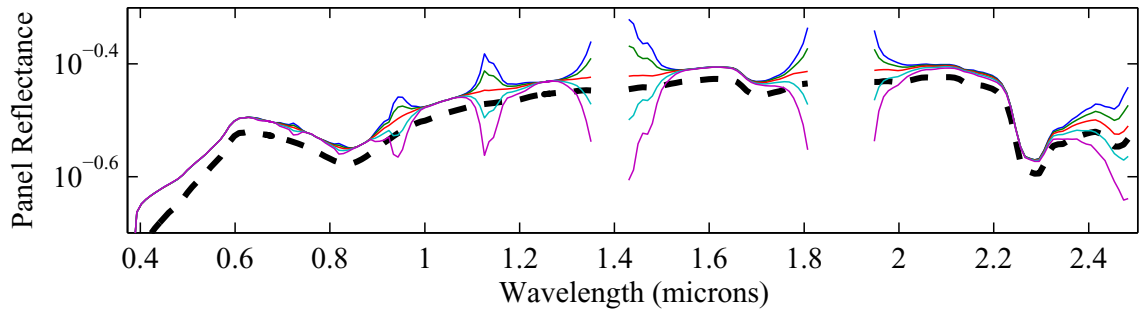
(o) Blue Car #20107



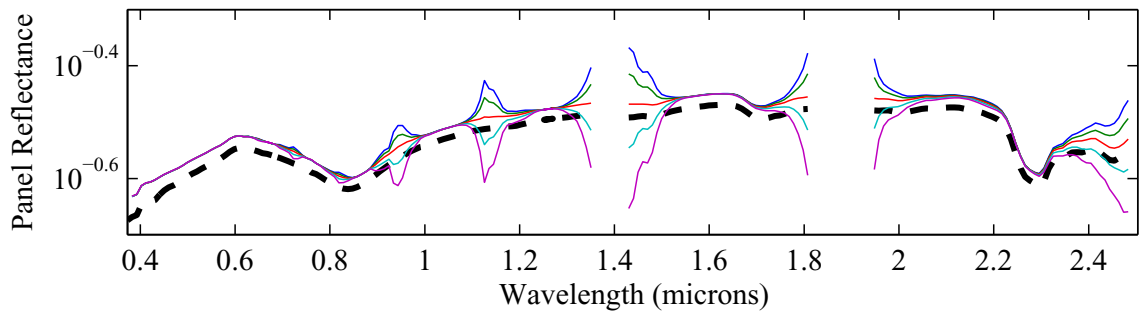
(p) Blue Car #20137



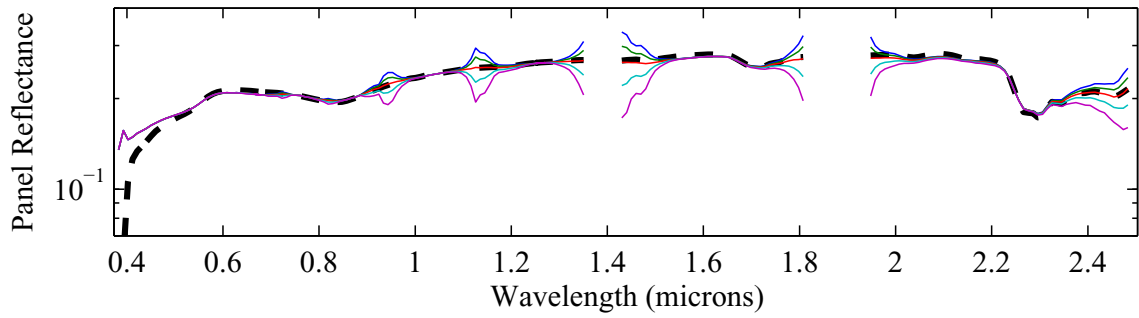
(q) Gold Car #20108



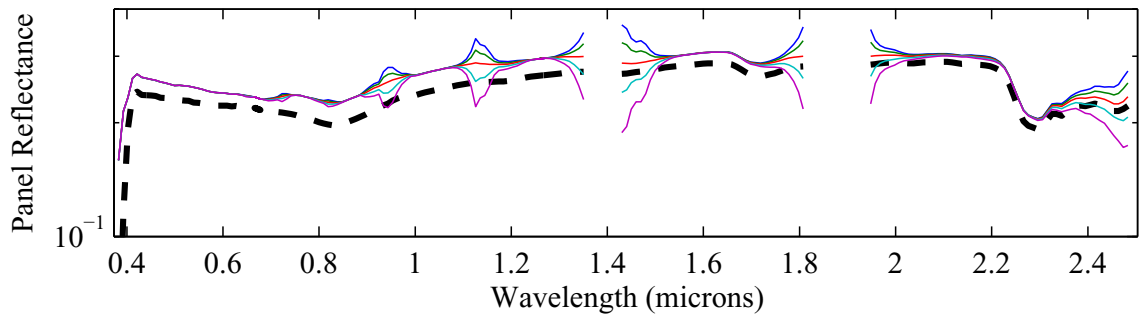
(r) Gold Car #20110



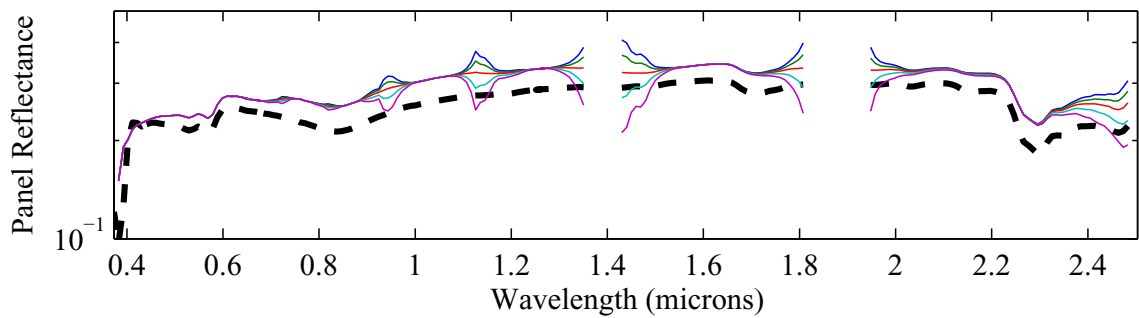
(s) Gold Car #20116



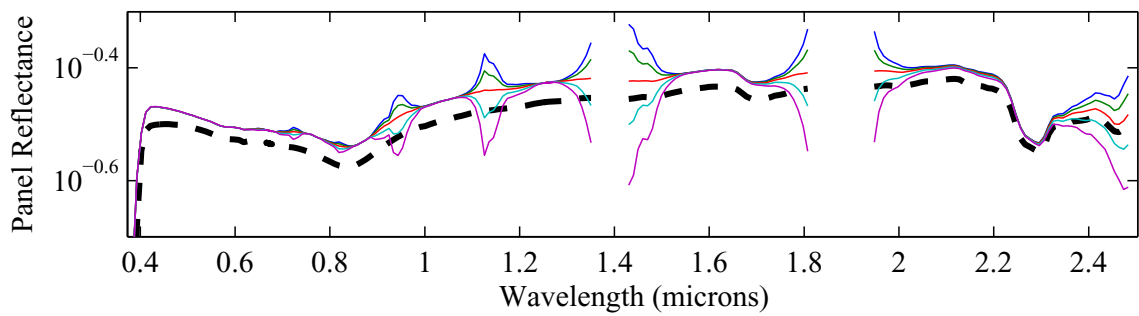
(t) Gold Car #20139



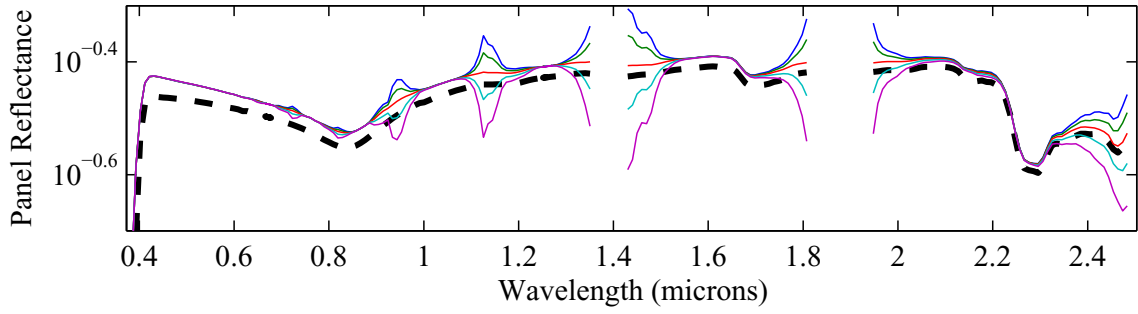
(u) Silver Car #20109



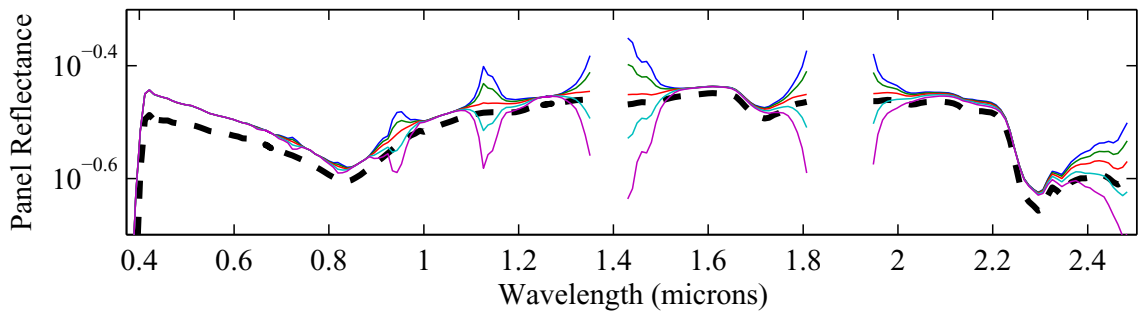
(v) Silver Car #20112



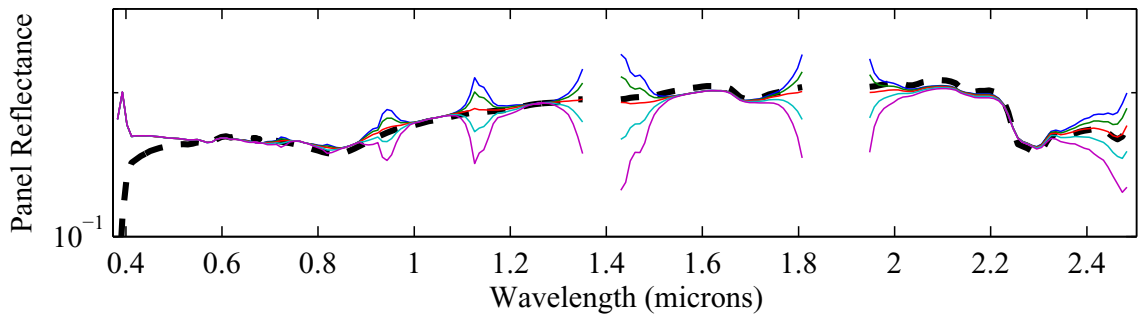
(w) Silver Car #20114



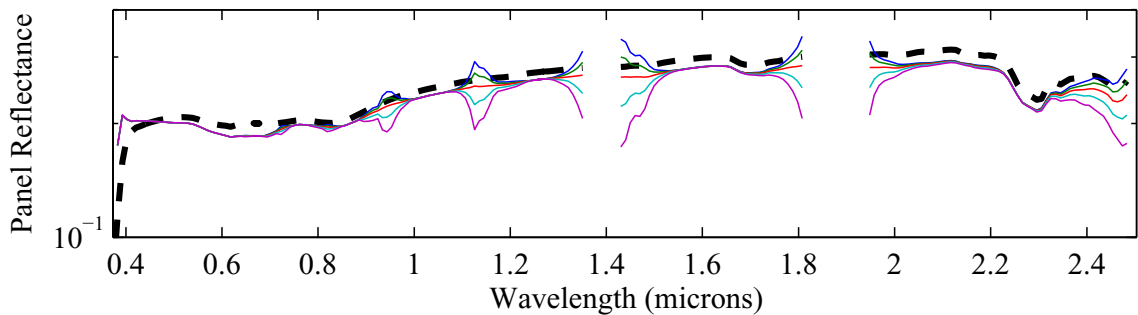
(x) Silver Car #20119



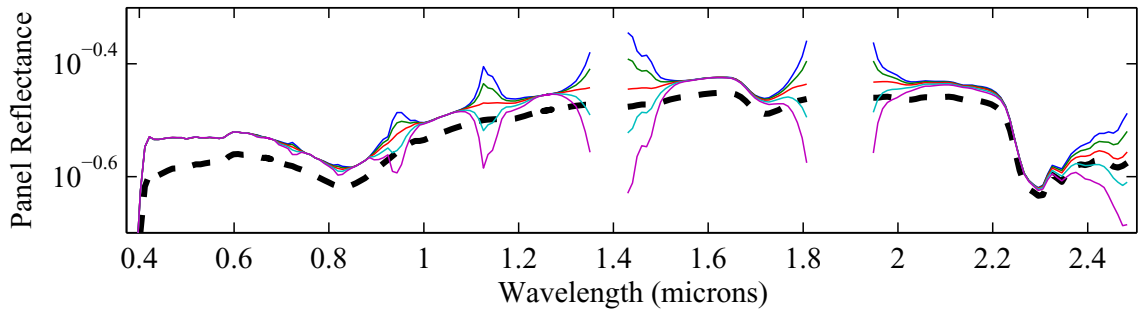
(y) Silver Car #20121



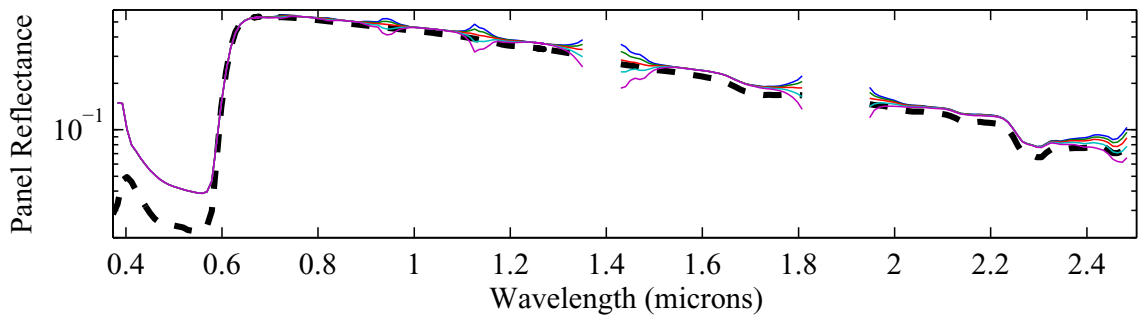
(z) Silver Car #20129



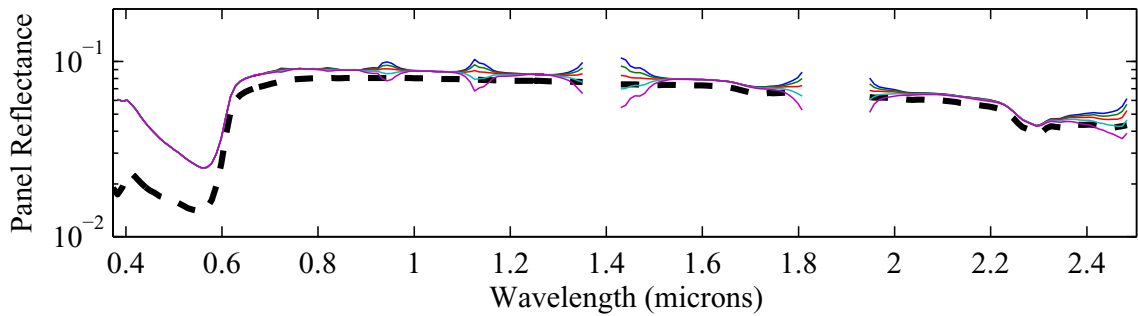
(aa) Silver Car #20134



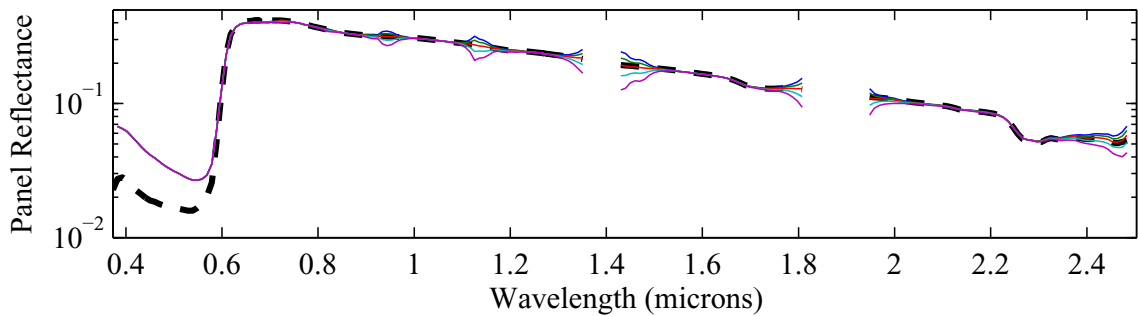
(bb) Steering Car #20113



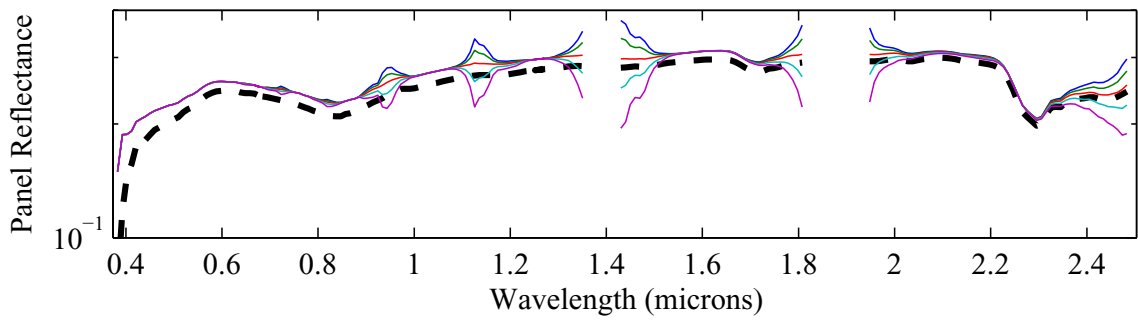
(cc) Red Car #20111



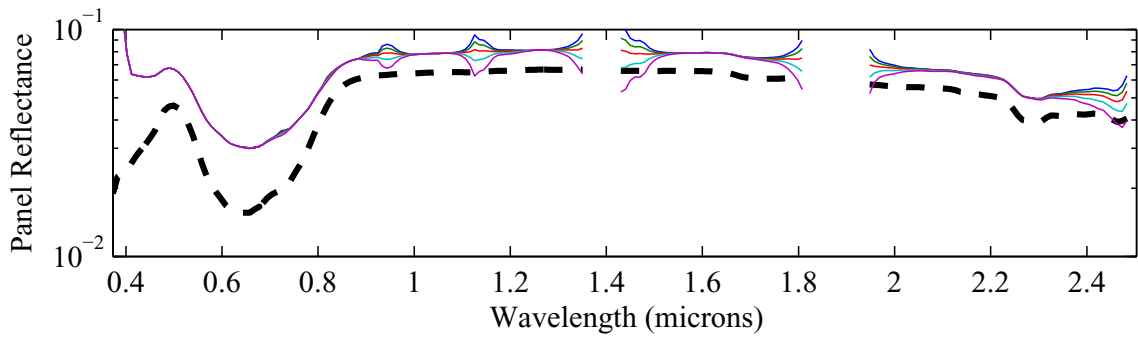
(dd) Red Car #20117



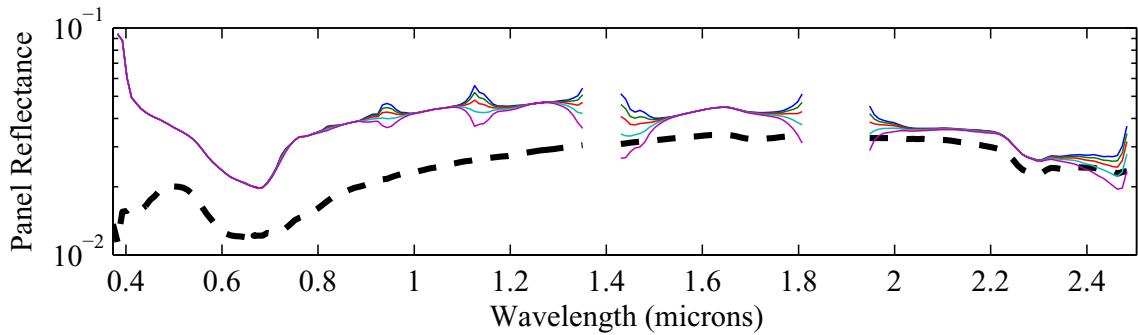
(ee) Red Car #20131



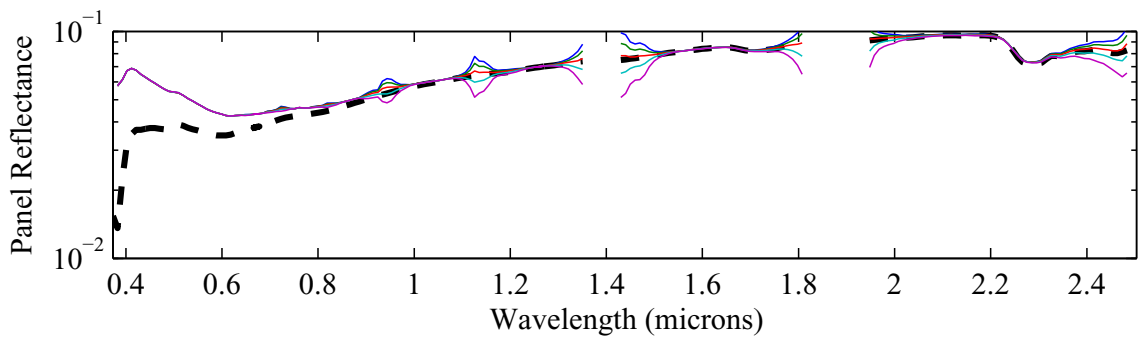
(ff) Light Gold Car #20115



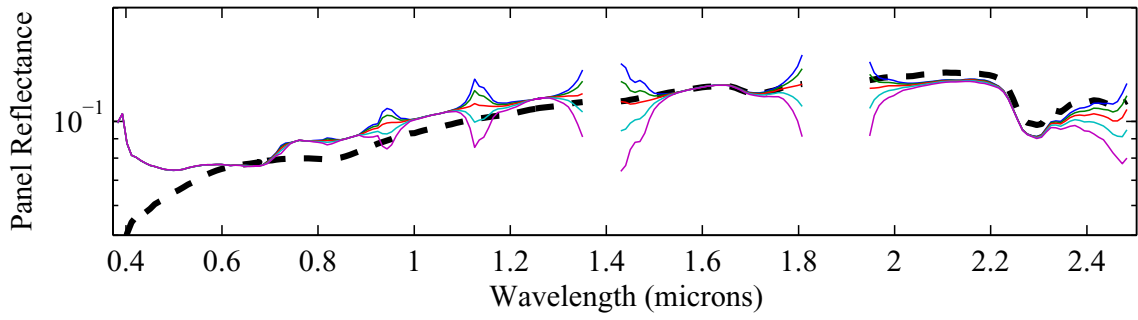
(gg) Green Car #20123



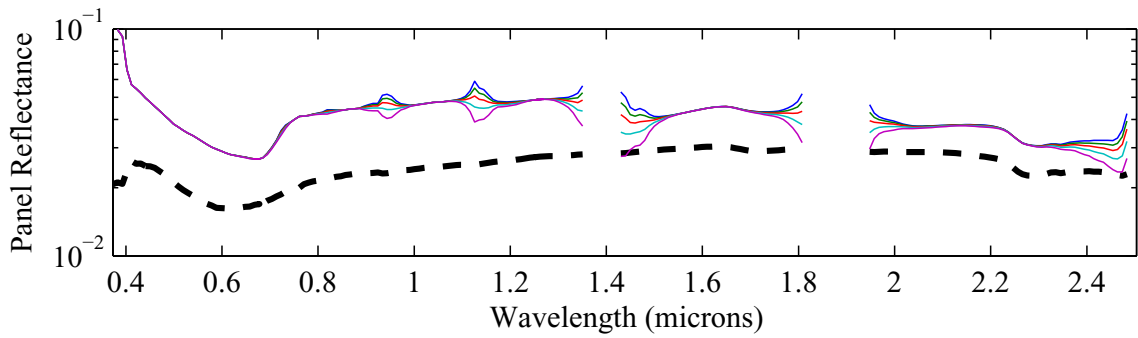
(hh) Green Car #20132



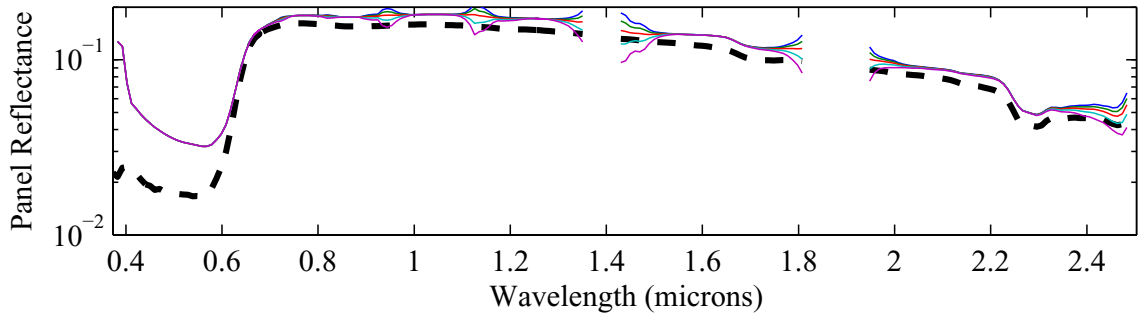
(ii) Gray Car w/ Black Top #20120



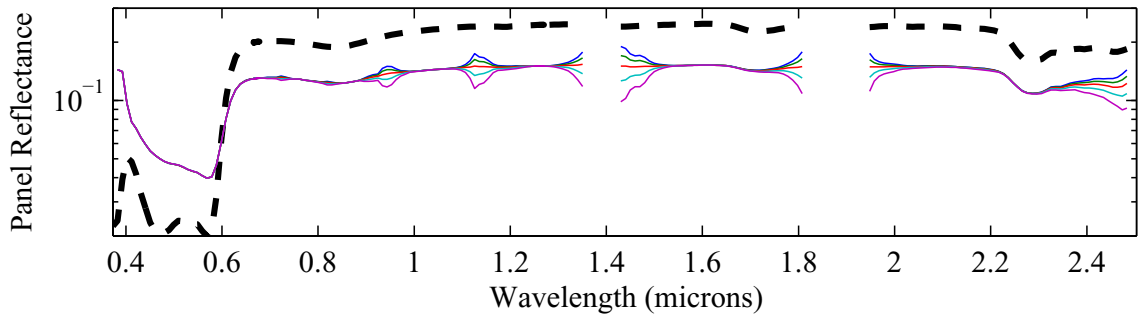
(jj) Brown Car #20125



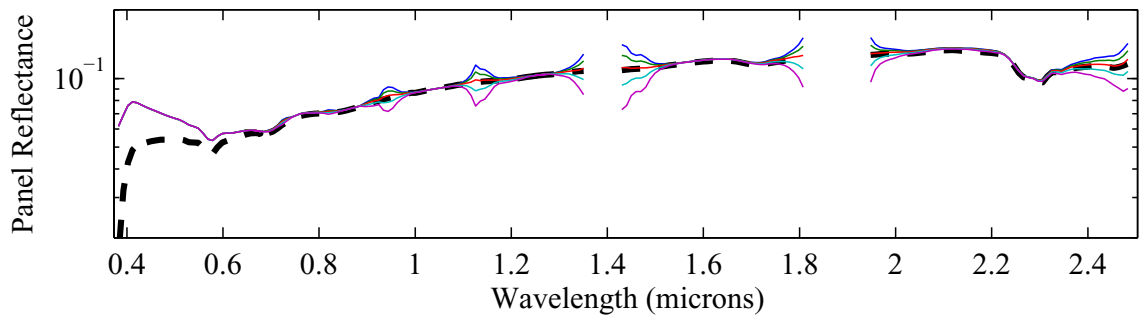
(kk) Blue Car w/ Black Top #20133



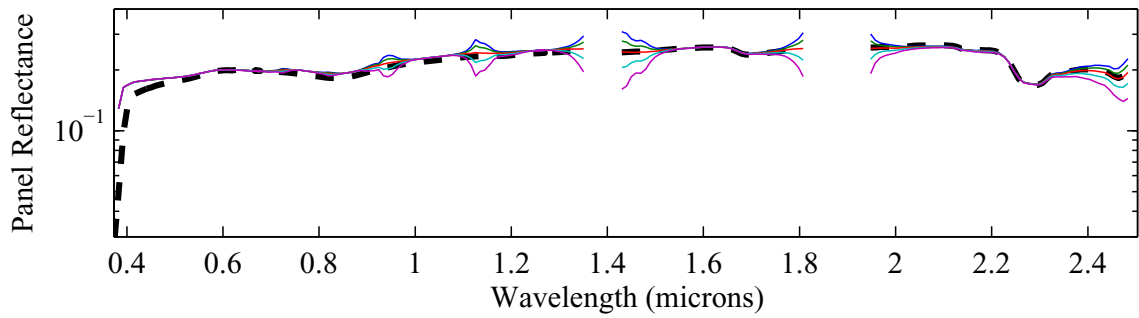
(ll) Cranberry Car #20136



(mm) Red and Silver Car #20138



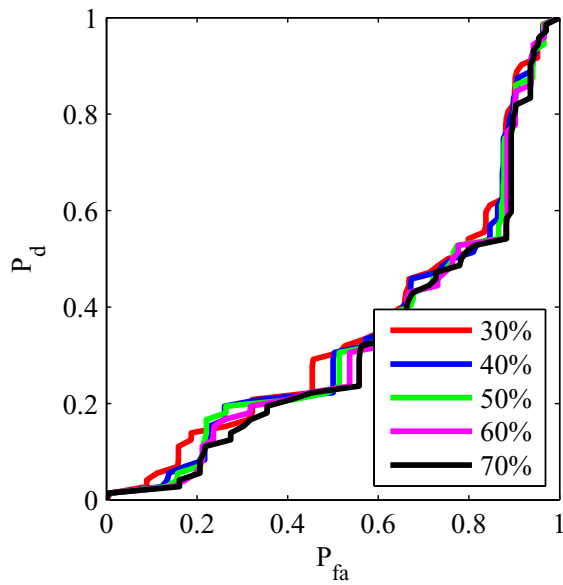
(nn) Charcoal Gray Car #20140



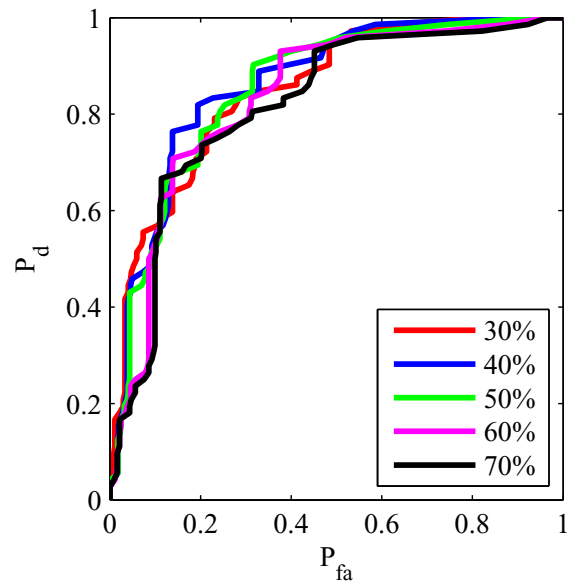
(oo) Gray Car #20141

### Appendix B. In-color ROC Curves by Percentile Atmosphere

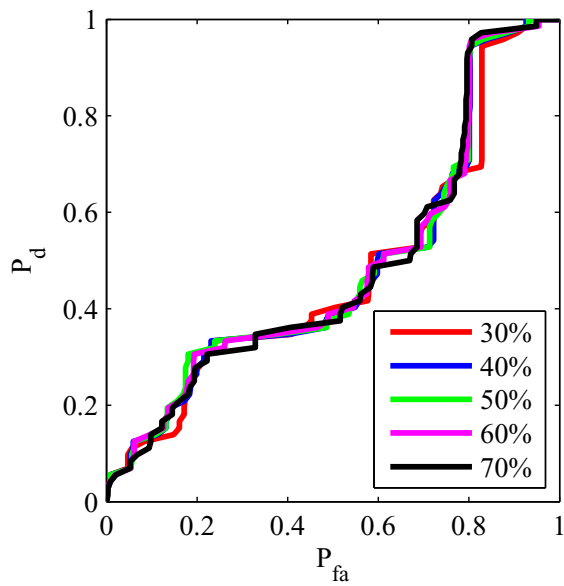
Shown here are the ROC curves for AMF detection of all cars for which we have multiple cars per color. The “estimated” atmosphere used to convert the image radiance measurements to reflectance was the 50<sup>th</sup> percentile; the “true” atmosphere used to simulate the image radiances are indicated in the legend. Note that the probabilities of false alarm ( $P_{fa}$ ) are calculated from only among cars of the same color as the target car.



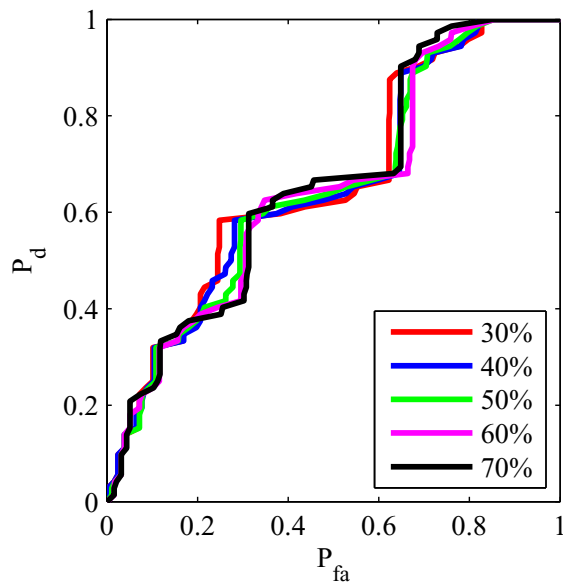
(a) Black Car #20102



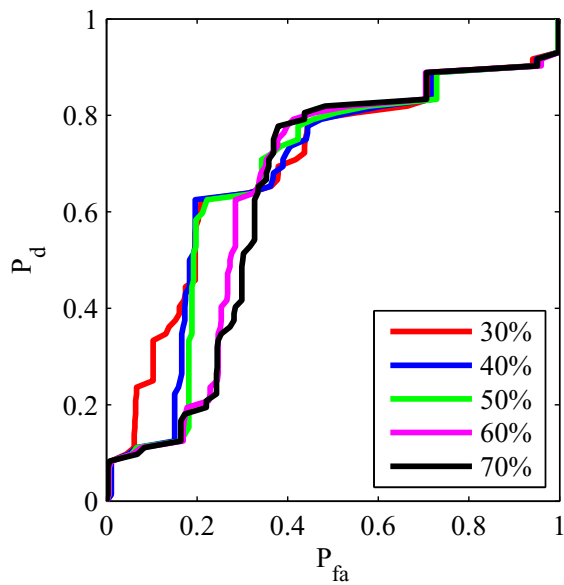
(b) Black Car #20104



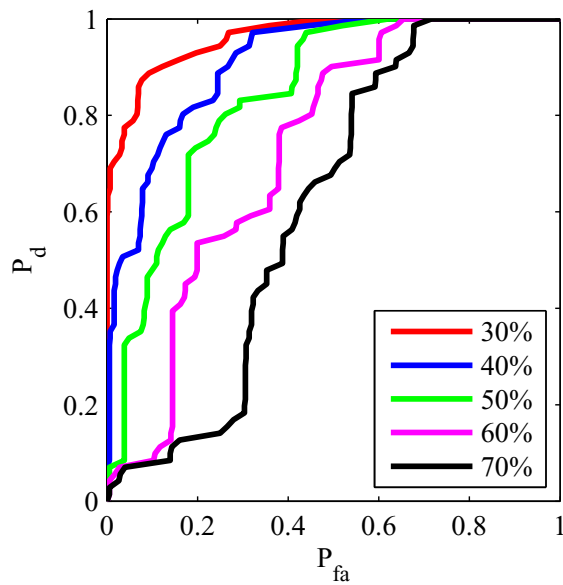
(c) Black Car #20118



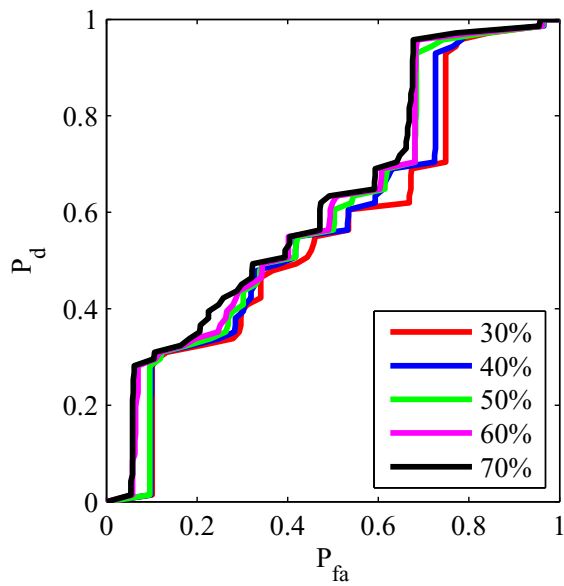
(d) Black Car #20122



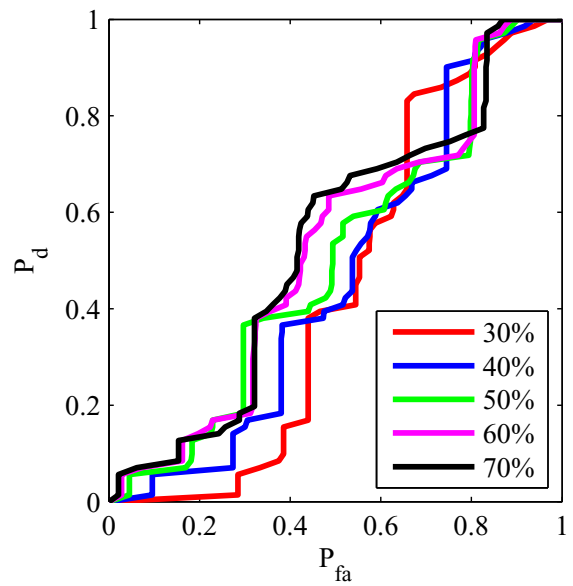
(e) Black Car #20124



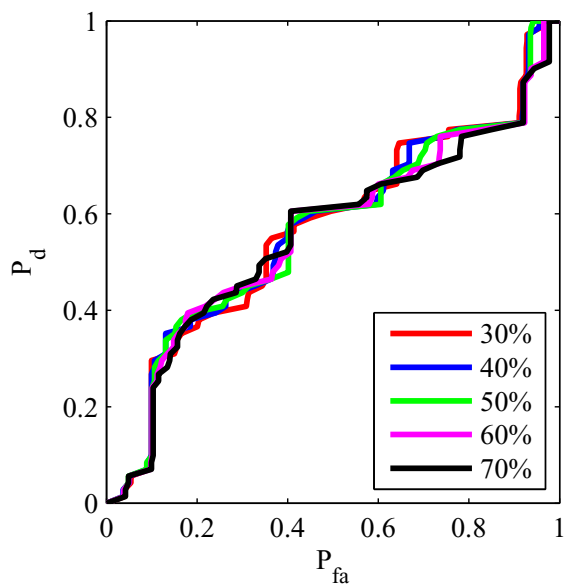
(f) Black Car #20126



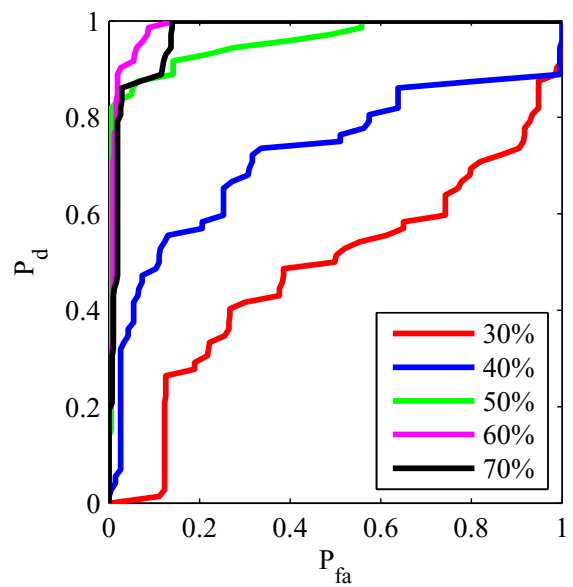
(g) Black Car #20127



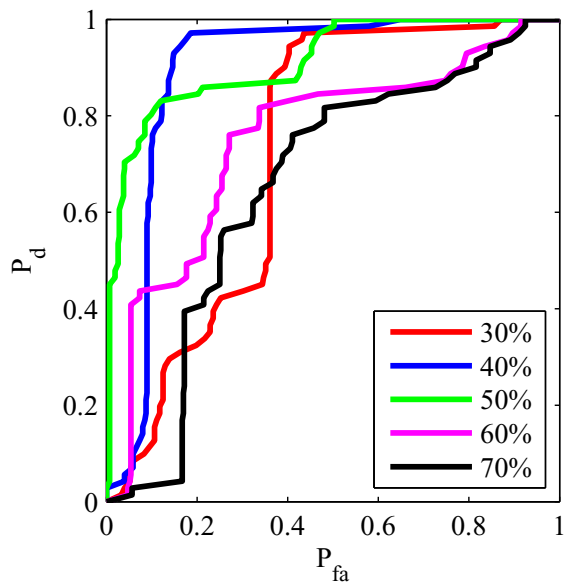
(h) Black Car #20130



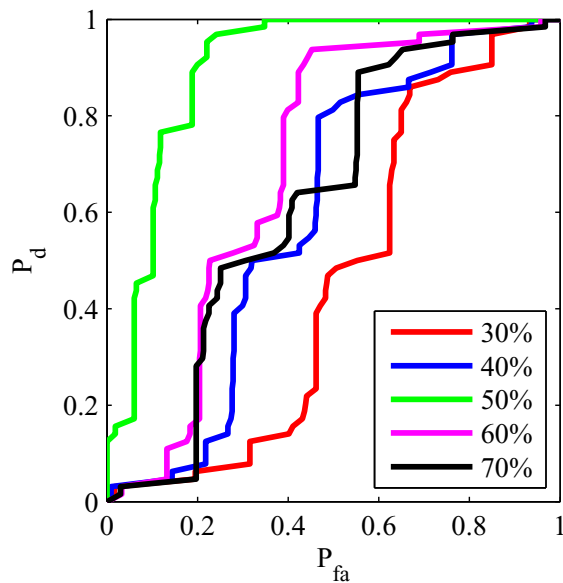
(i) Black Car #20135



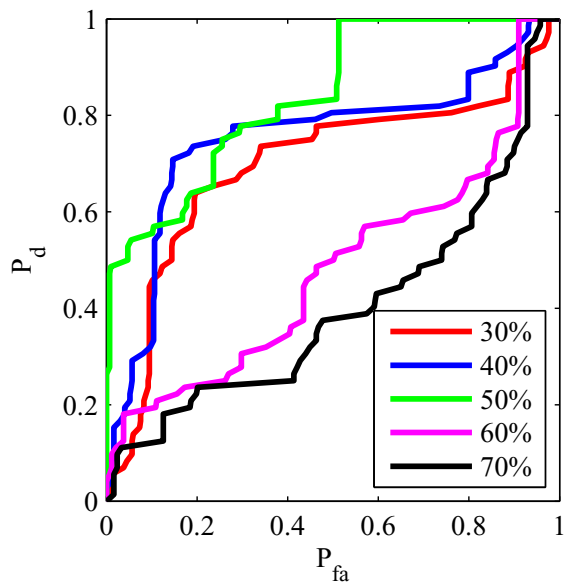
(j) Silver Car #20109



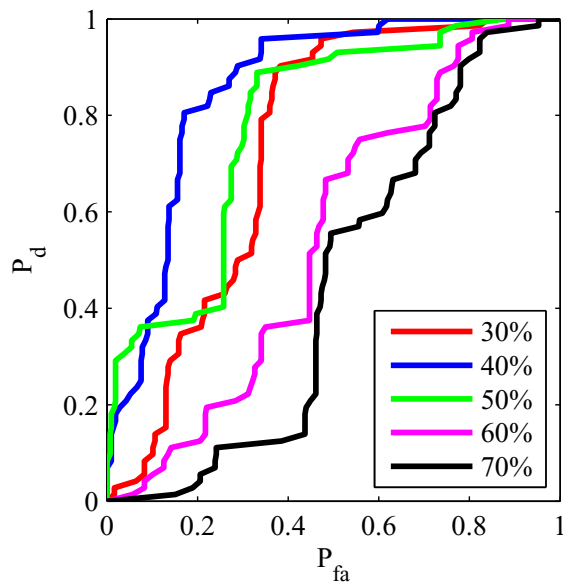
(k) Silver Car #20112



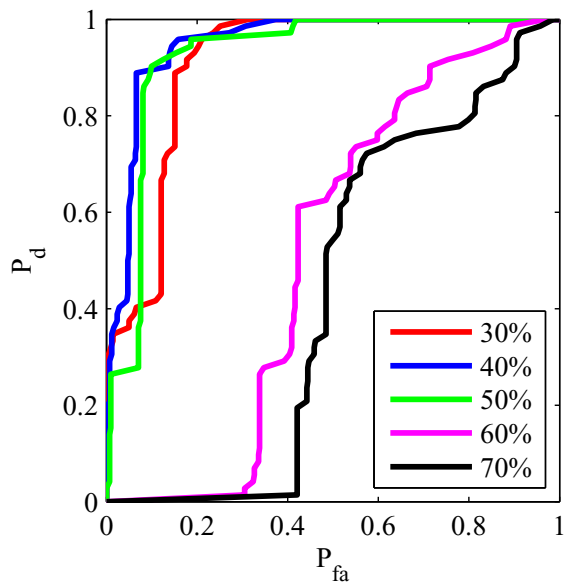
(l) Silver Car #20114



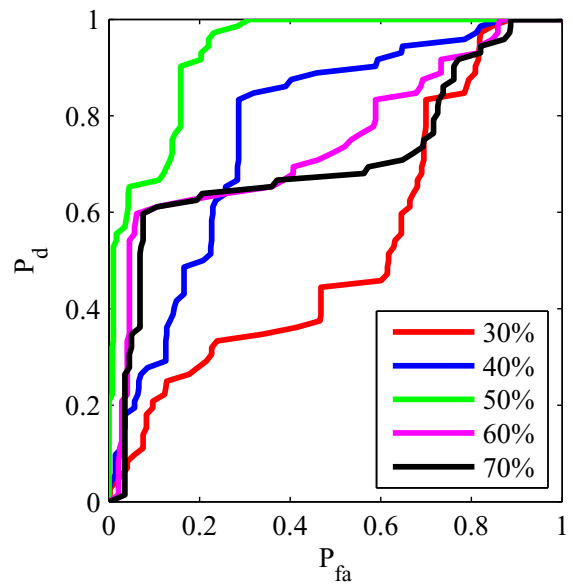
(m) Silver Car #20119



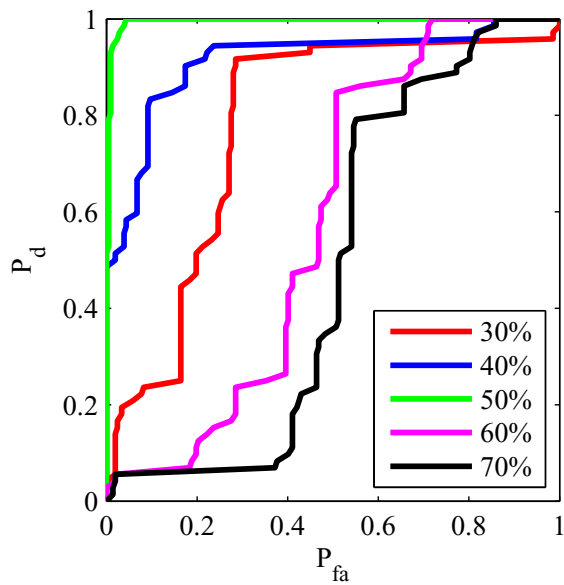
(n) Silver Car #20121



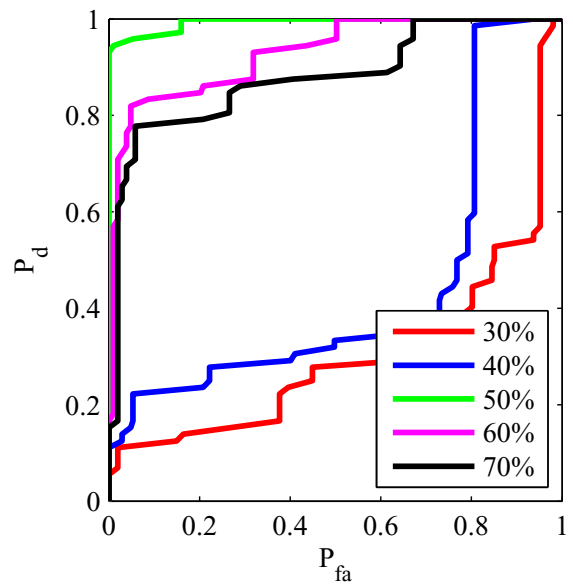
(o) Silver Car #20129



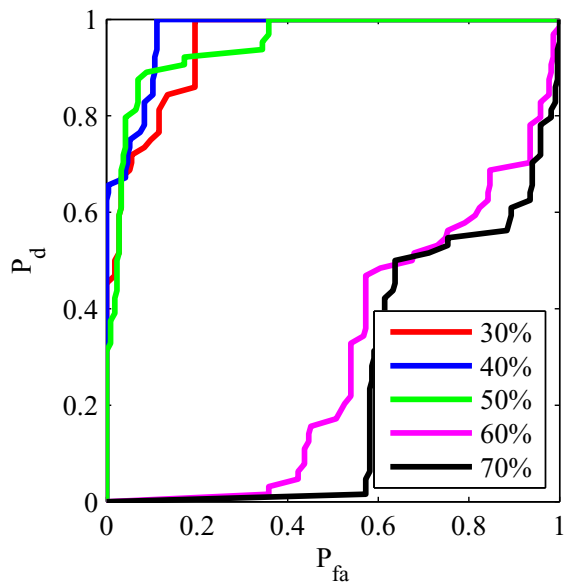
(p) Silver Car #20134



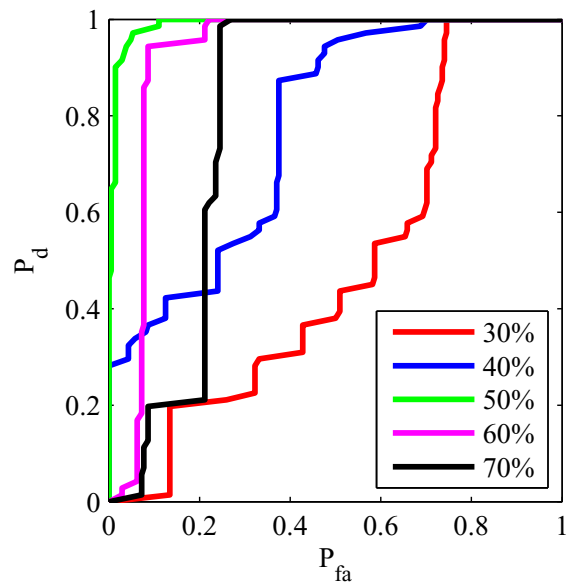
(q) Gold Car #20108



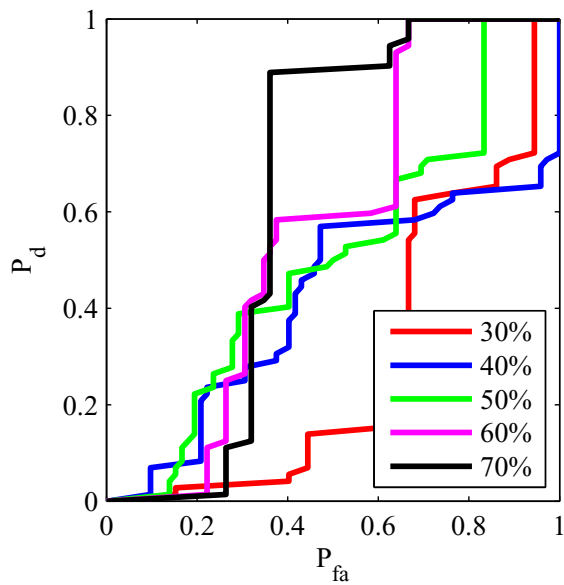
(r) Gold Car #20110



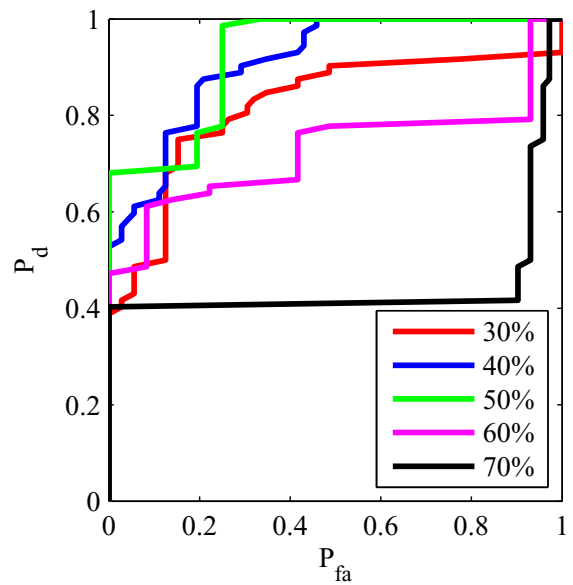
(s) Gold Car #20116



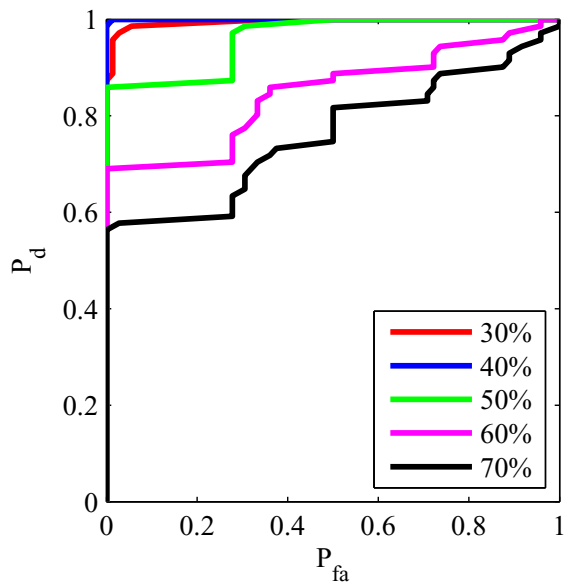
(t) Gold Car #20139



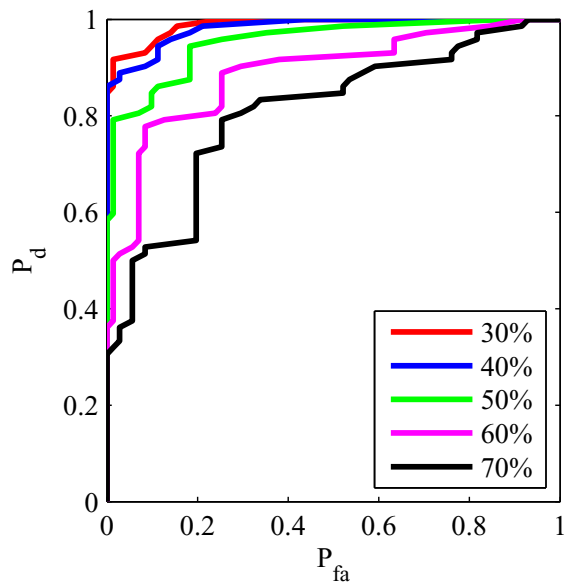
(u) Blue Car #20107



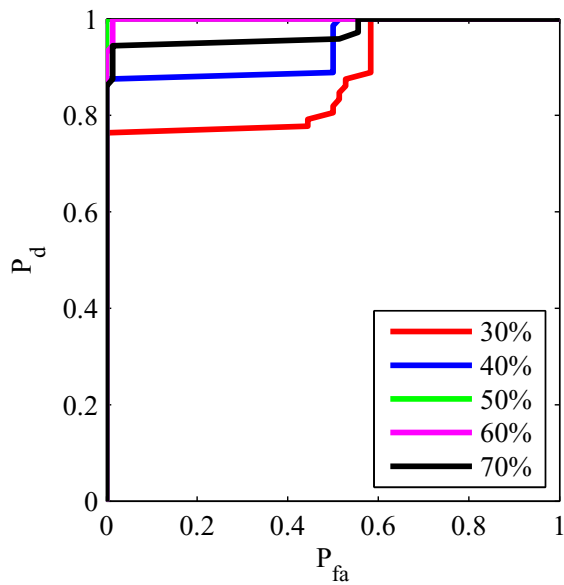
(v) Blue Car #20137



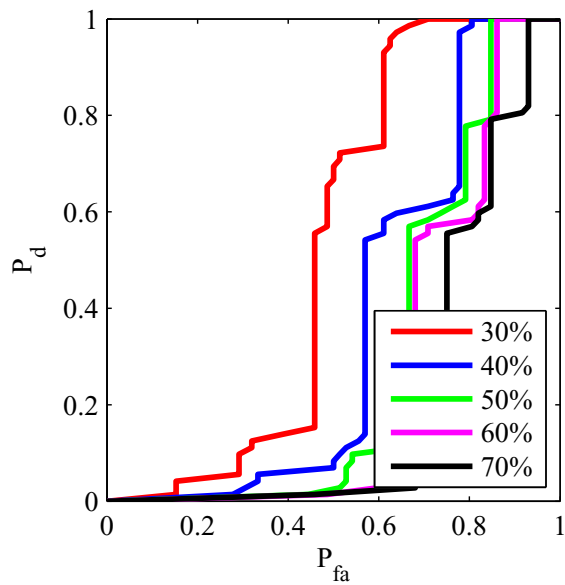
(w) Green Car #20123



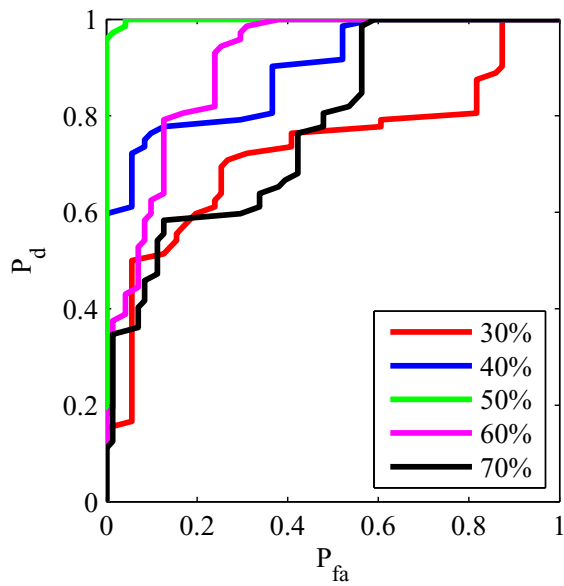
(x) Green Car #20132



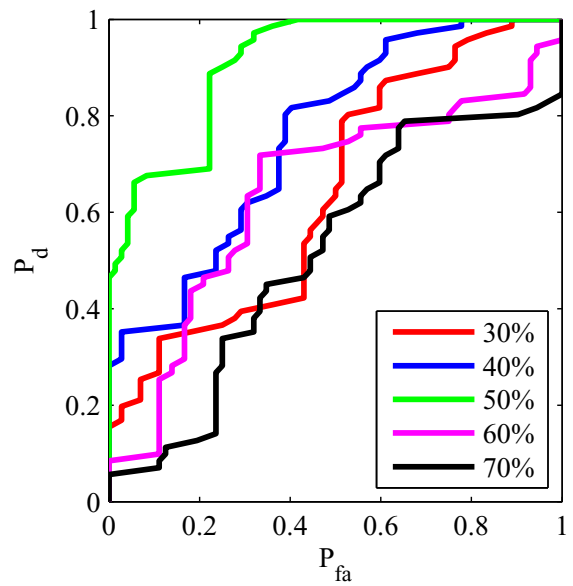
(y) Maroon Car #20105



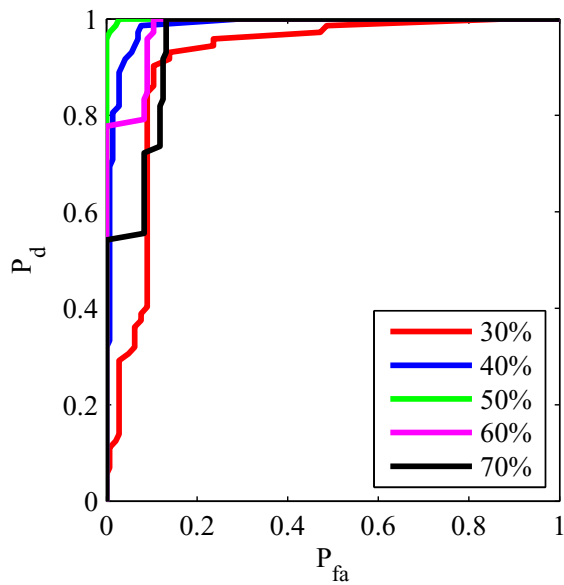
(z) Maroon Car #20128



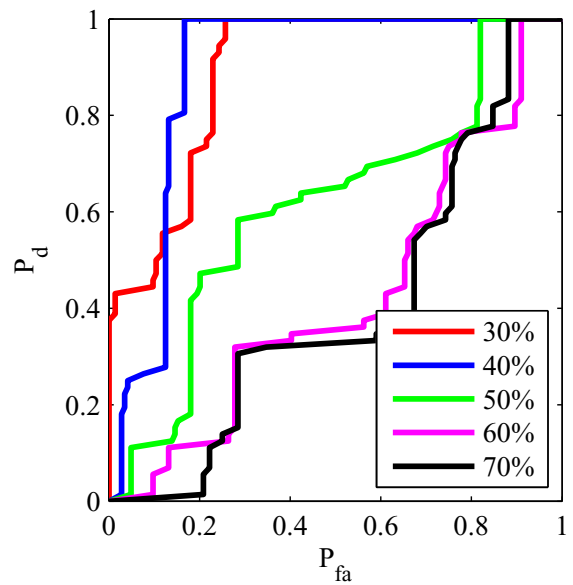
(aa) White Car #20101



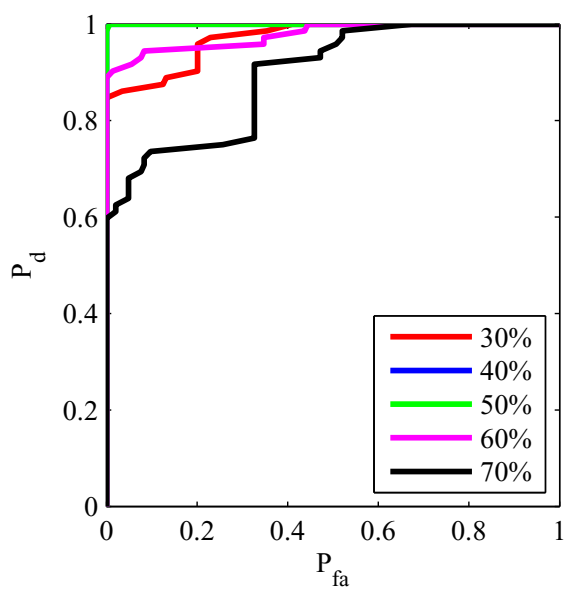
(bb) White Car #20103



(cc) Red Car #20111



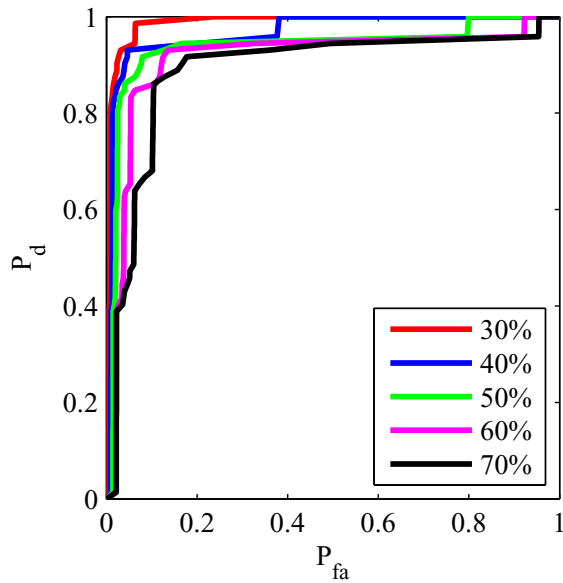
(dd) Red Car #20117



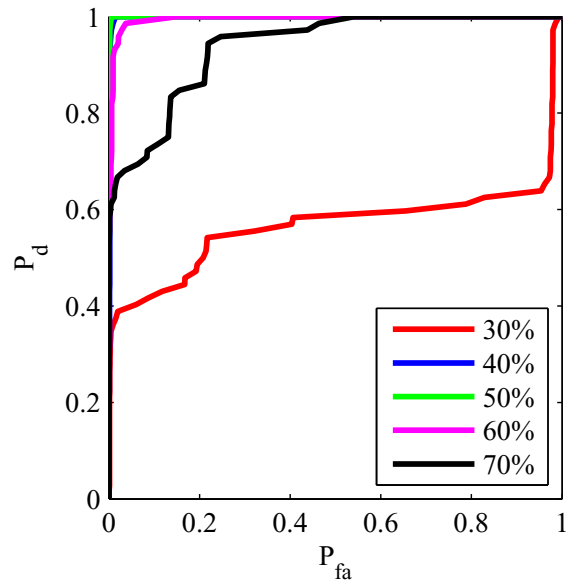
(ee) Red Car #20131

### Appendix C. Full-background ROC Curves by Percentile Atmosphere

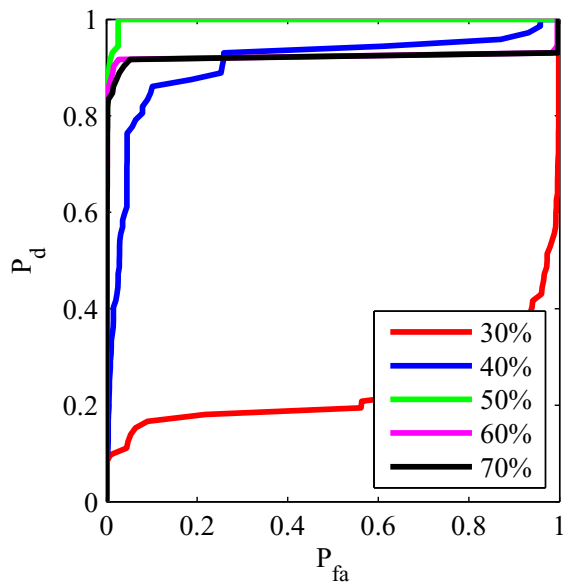
Shown here are the ROC curves for AMF detection of all cars for which we have only one car per color. The “estimated” atmosphere used to convert the image radiance measurements to reflectance was the 50<sup>th</sup> percentile; the “true” atmosphere used to simulate the image radiances are indicated in the legend. Note that the probabilities of false alarm ( $P_{fa}$ ) are calculated from among all image pixels.



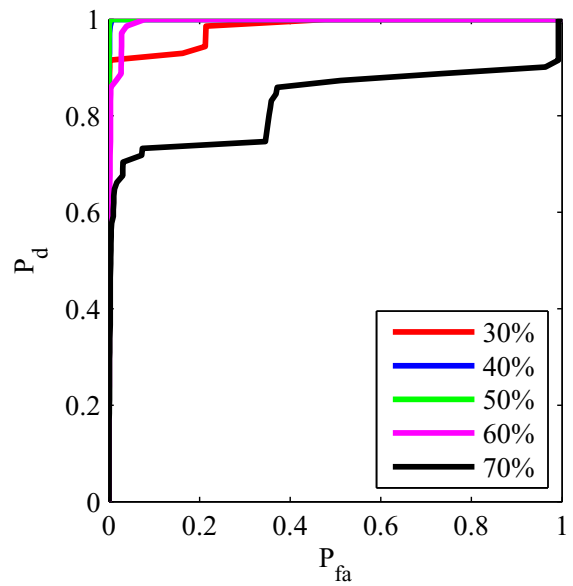
(a) Blue Car w/ Black Top #20133



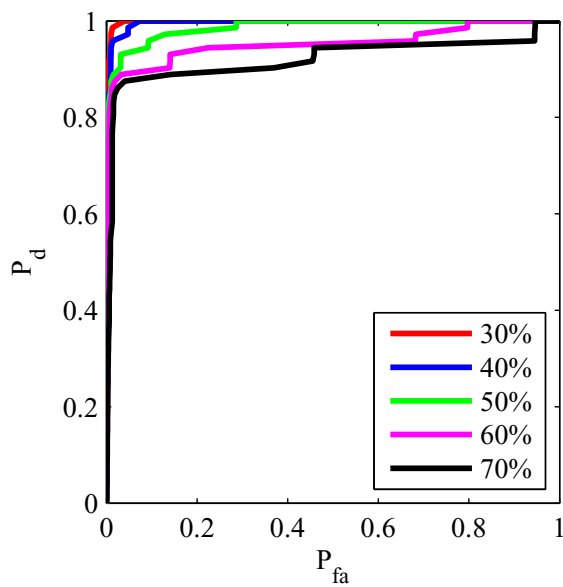
(b) Brown Car #20125



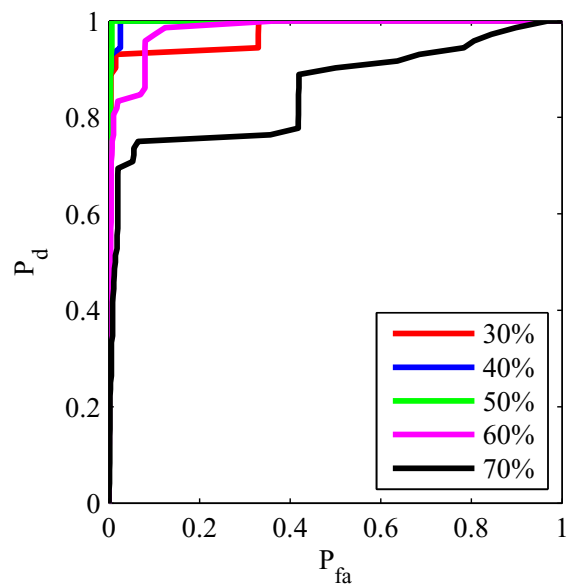
(c) Charcoal Gray Car #20140



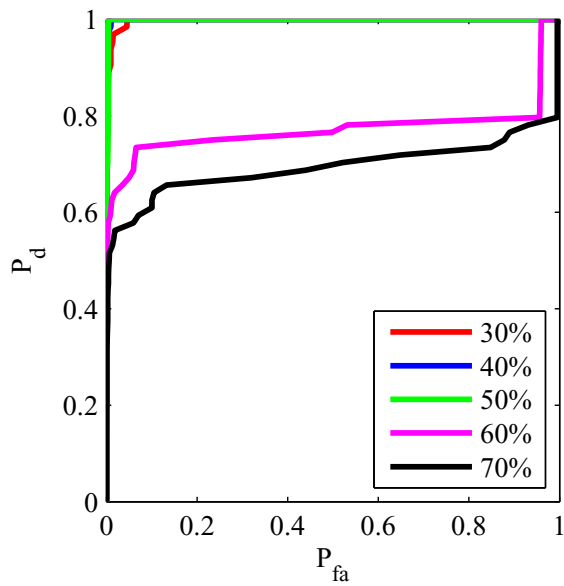
(d) Cranberry Car #20136



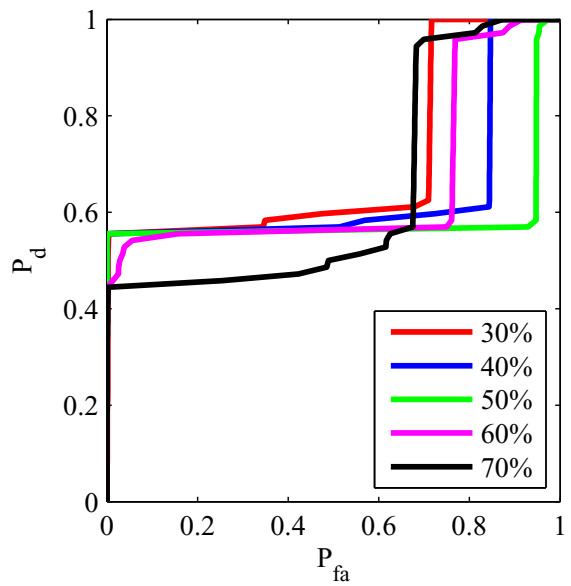
(e) Dark Blue Car #20106



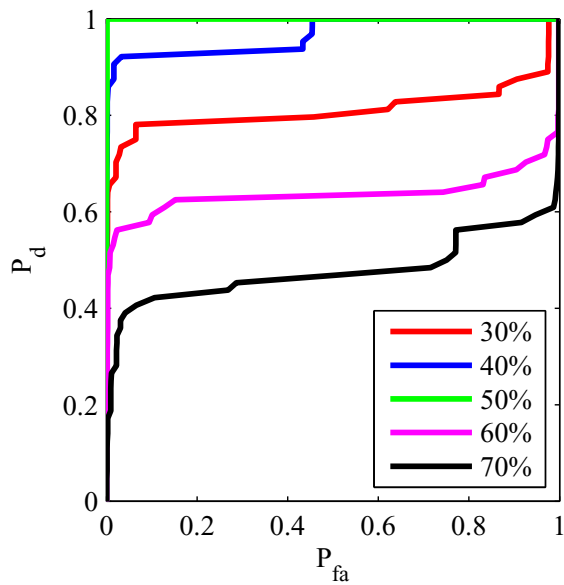
(f) Gray Car w/ Black Top #20120



(g) Light Gold Car #20115



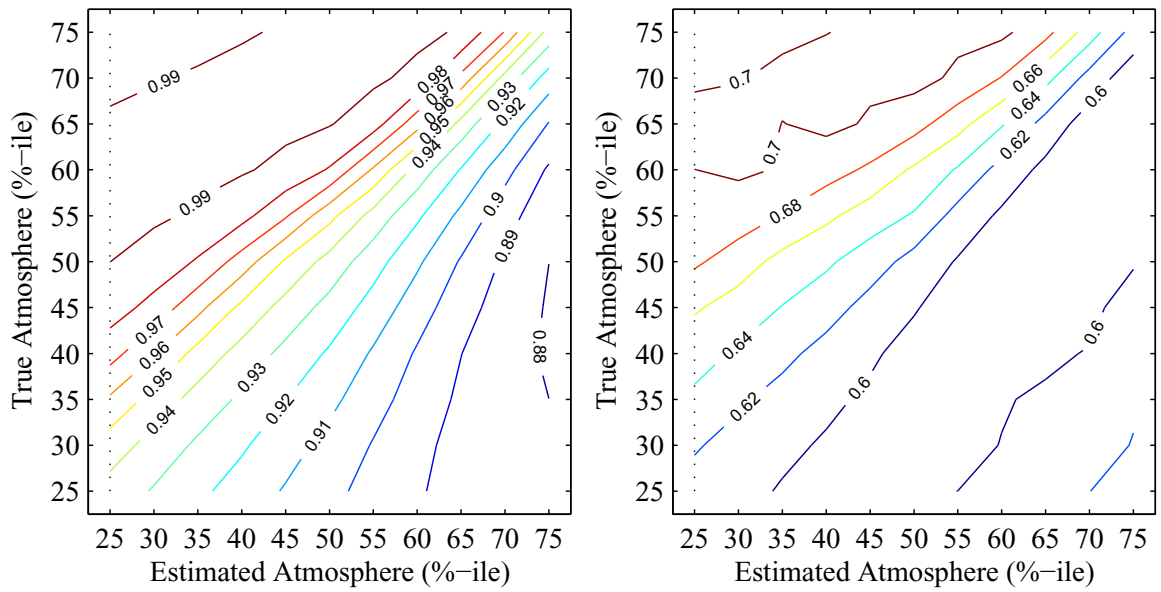
(h) Red and Silver Car #20138



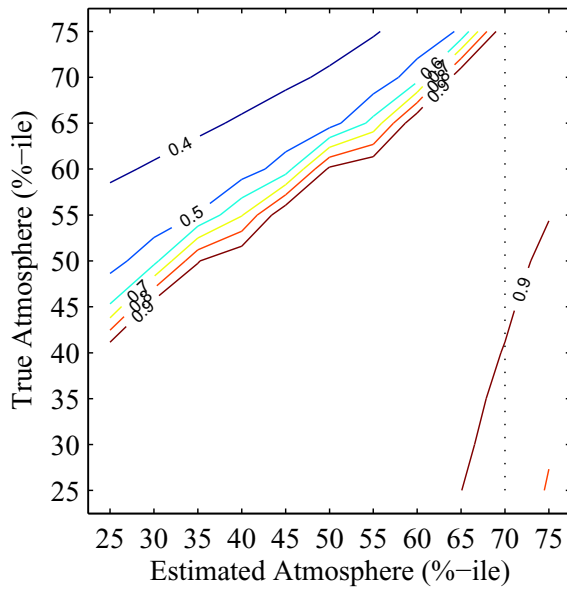
(i) Sterling Car #20113

### Appendix D. AUC Contour Plots

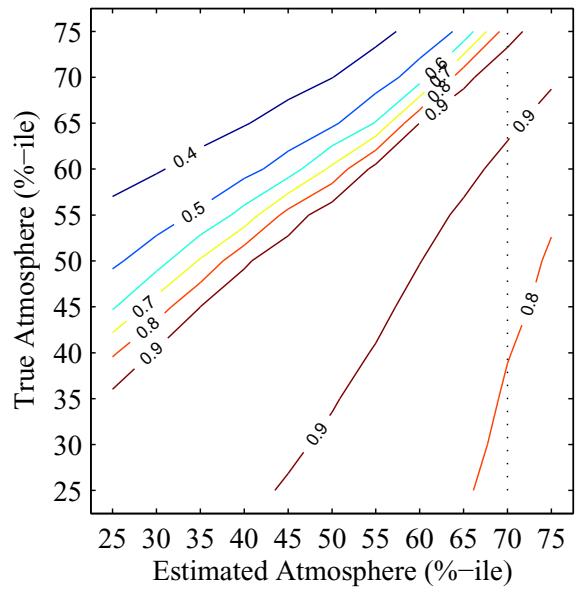
Contour plots of the AUCs for AMF detection of the indicated automobiles with the  $P_{fa}$ 's calculated from false alarms generated by all background pixels and automobile pixels only. We vary both the “true” image illumination ( $y$ -axis) and the estimated illumination ( $x$ -axis) by their percentiles in the historical distribution at the target site. Note that the estimated illumination percentile that maximizes the AUC across all possible true illumination percentiles is indicated by the black dotted line.



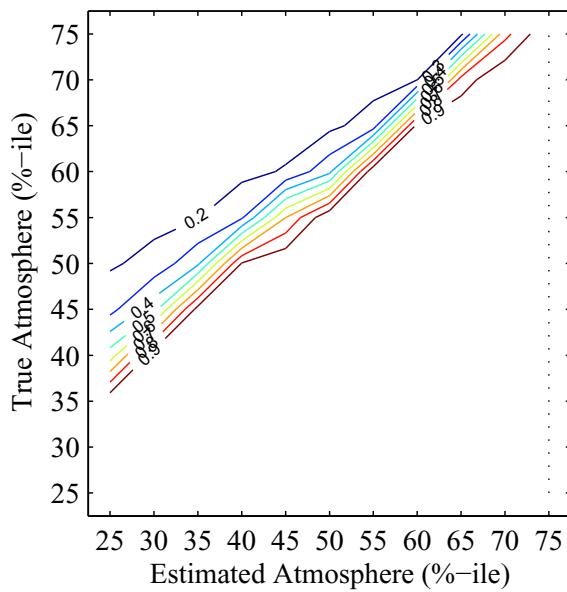
(a) Blue w/ Black Top, Entire Background (b) Blue w/ Black Top, Car-class Only



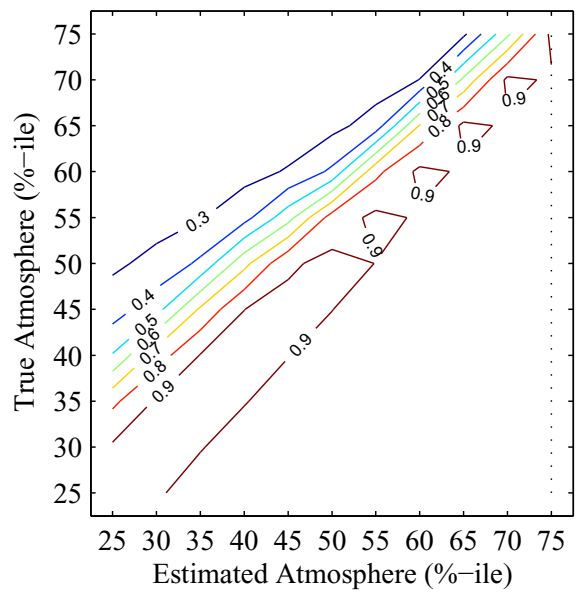
(c) Brown Car AUCs, entire background



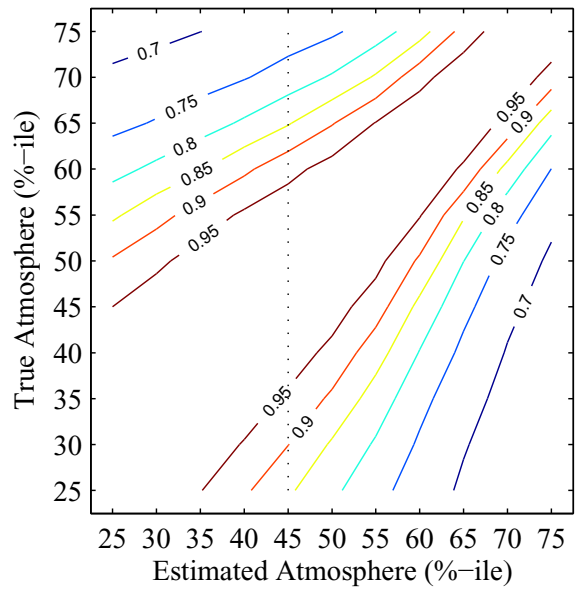
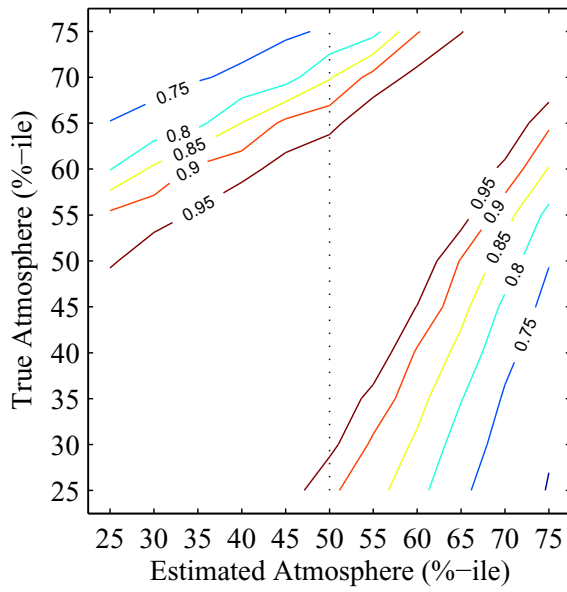
(d) Brown Car AUCs, car-class only



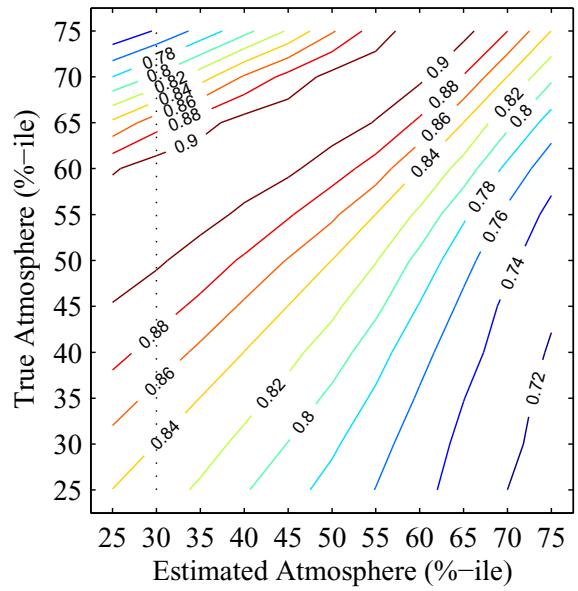
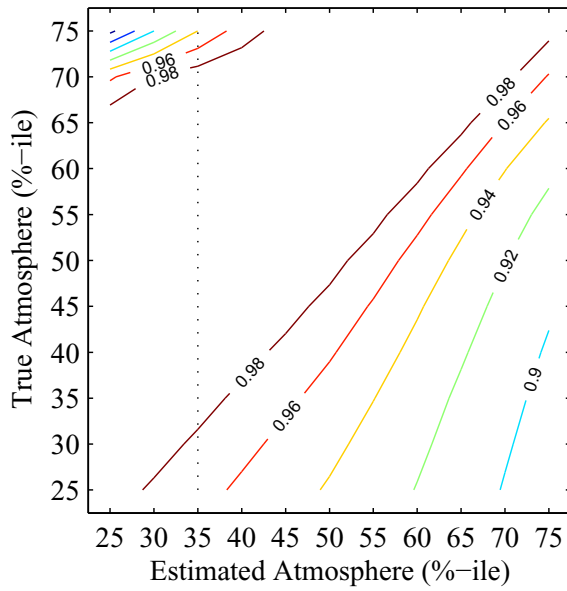
(e) Charcoal Gray, Entire Background



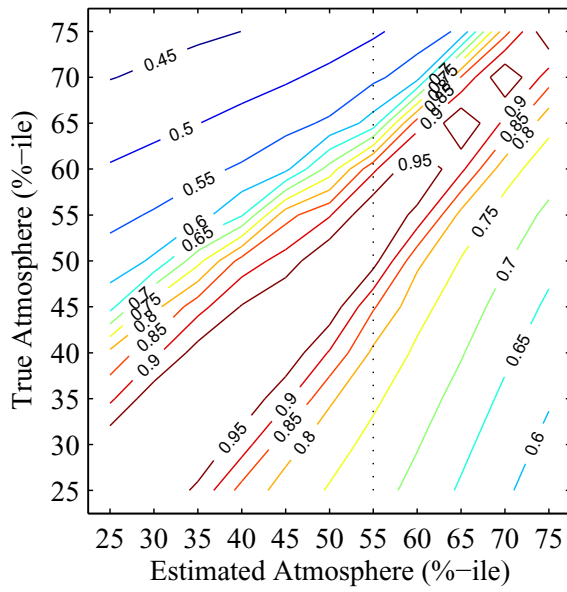
(f) Charcoal Gray, Car-class Only



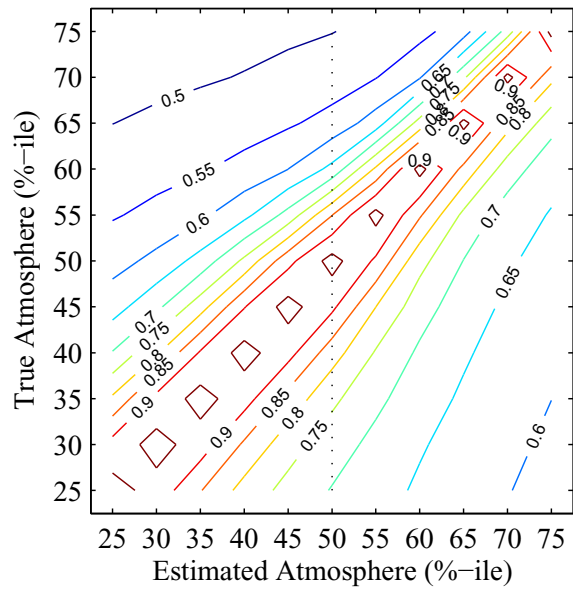
(g) Cranberry Car AUCs, entire background (h) Cranberry Car AUCs, car-class only



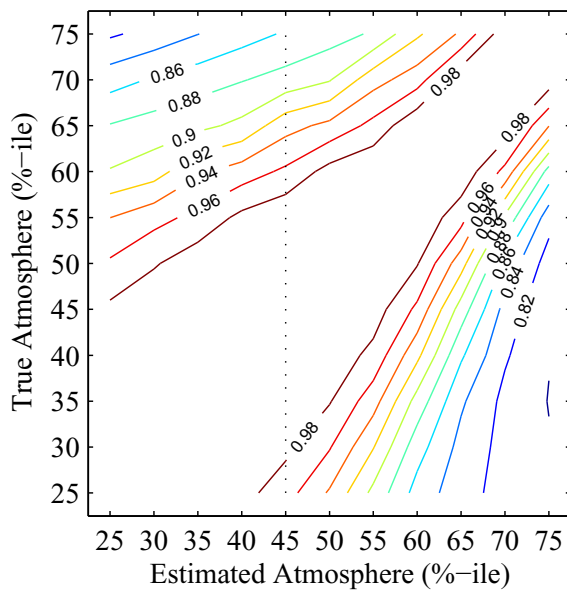
(i) Dark Blue Car AUCs, Entire Background (j) Dark Blue Car AUCs, Car-class Only



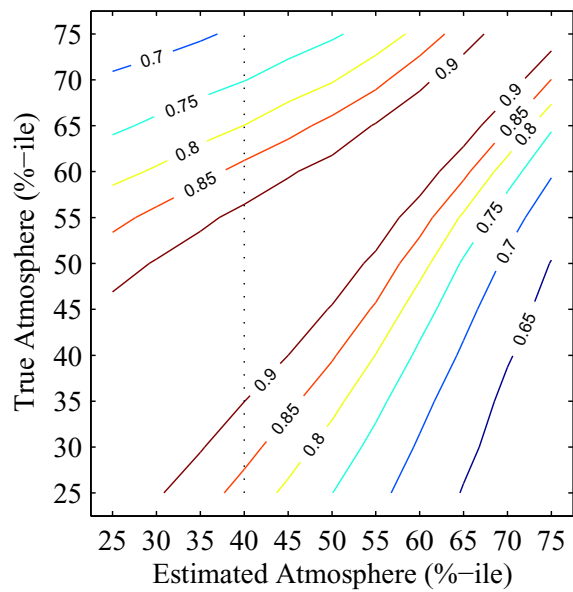
(k) Gray Car AUCs, entire background



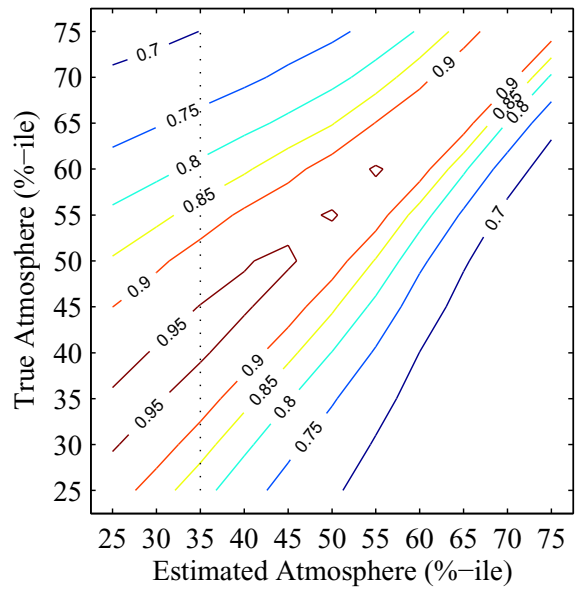
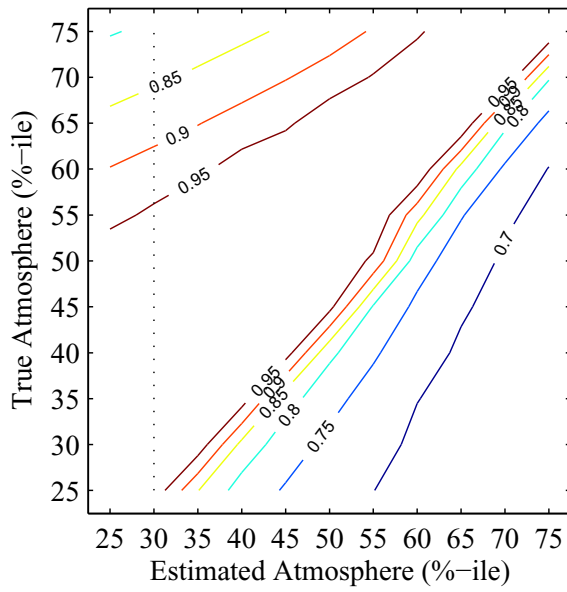
(l) Gray Car AUCs, car-class only



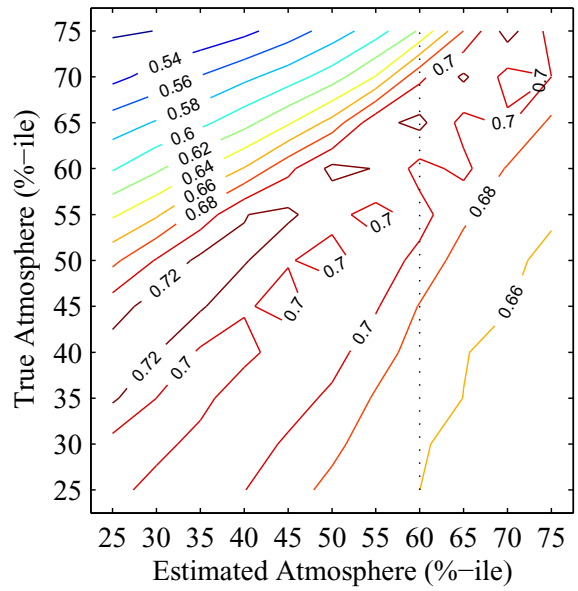
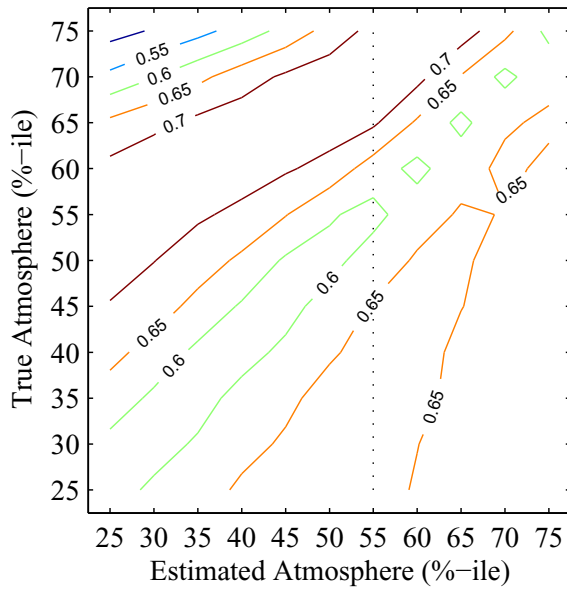
(m) Gray w/ Black Top, Entire Background



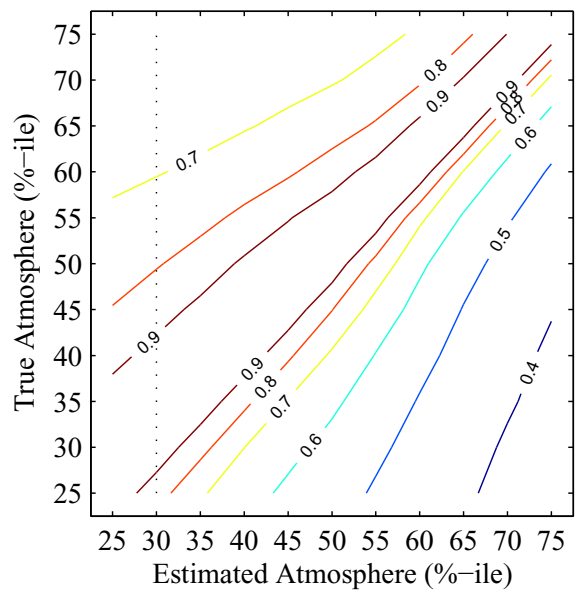
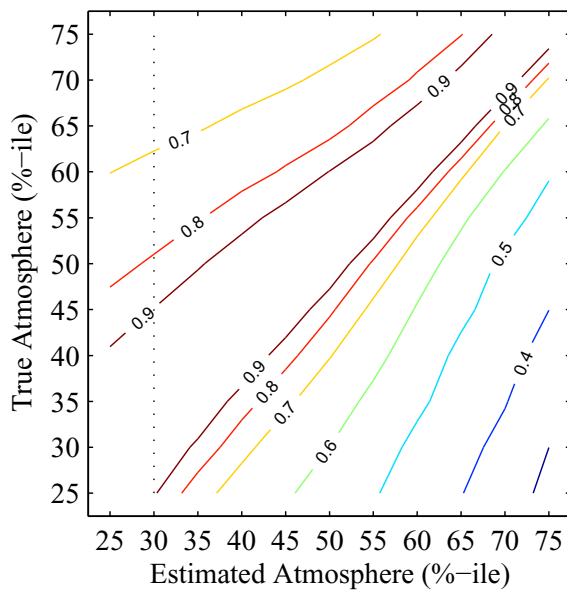
(n) Gray w/ Black Top, Car-class Only



(o) Light Gold Car AUCs, entire background (p) Light Gold Car AUCs, car-class only



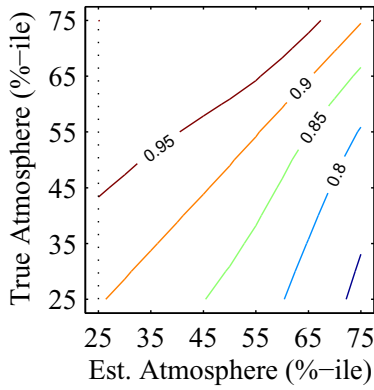
(q) Red-Silver Car AUCs, Entire Background (r) Red-Silver Car AUCs, Car-class Only



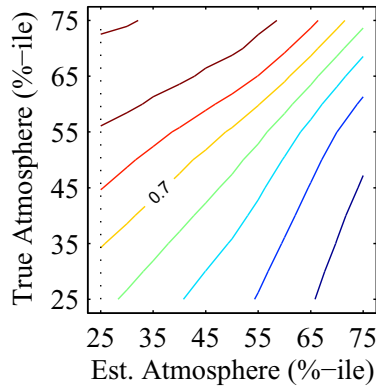
(s) Sterling Car AUCs, entire background

(t) Sterling Car AUCs, car-class only

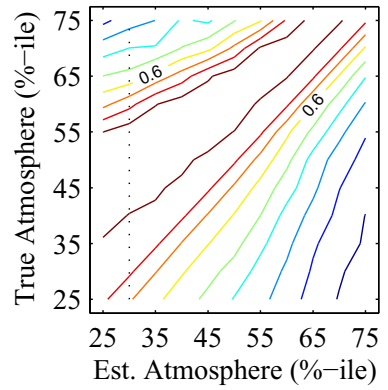
Contour plots of the average AUCs for AMF detection of the indicated cars with the  $P_{fa}$ 's calculated from false alarms generated by all background pixels, automobile pixels only, and like-color automobile pixels. We vary both the “true” image illumination ( $y$ -axis) and the estimated illumination ( $x$ -axis) by their percentiles in the historical distribution at the target site. Note that the estimated illumination percentile that maximizes the AUC across all possible true illumination percentiles is indicated by the black dotted line.



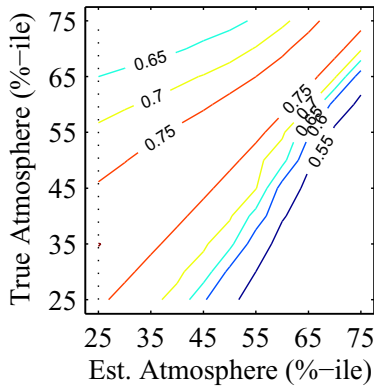
(u) Black, entire background



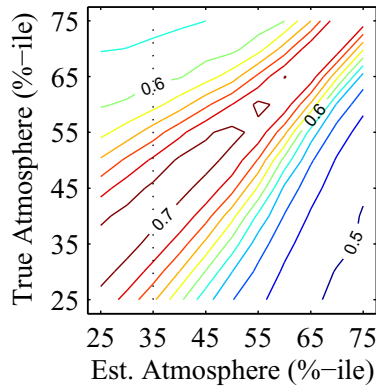
(v) Black, car-class only



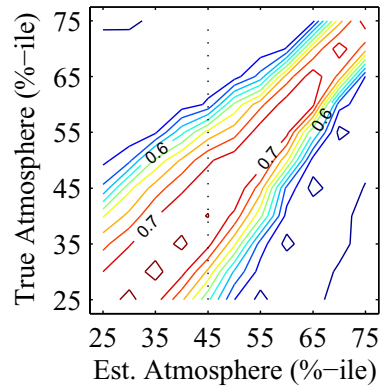
(w) Black, like-color only



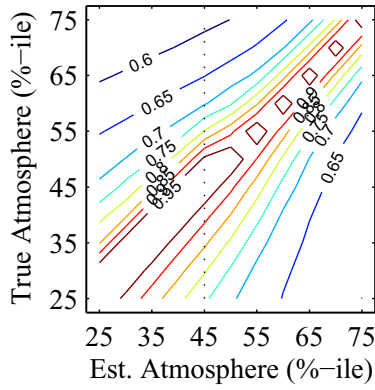
(x) Blue, entire background



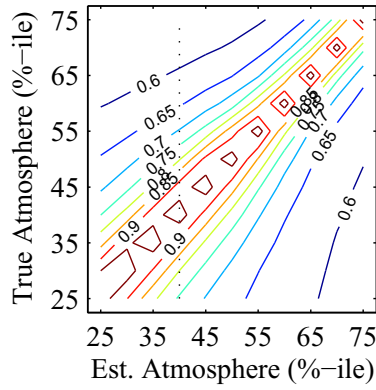
(y) Blue, car-class only



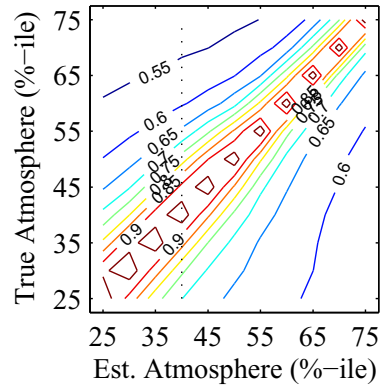
(z) Blue, like-color only



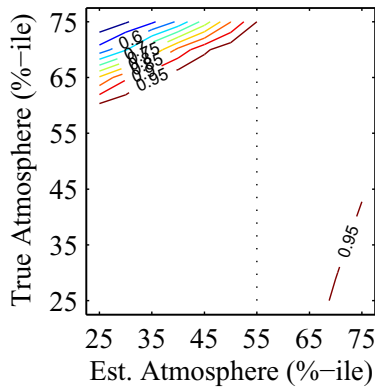
(aa) Gold, entire background



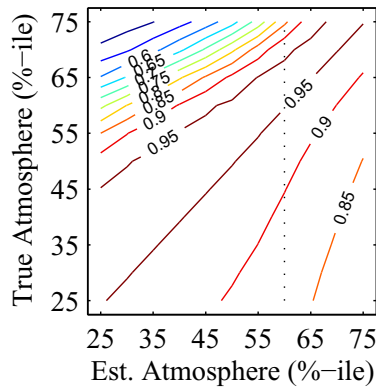
(bb) Gold, car-class only



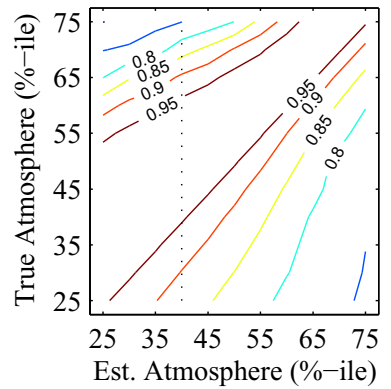
(cc) Gold, like-color only



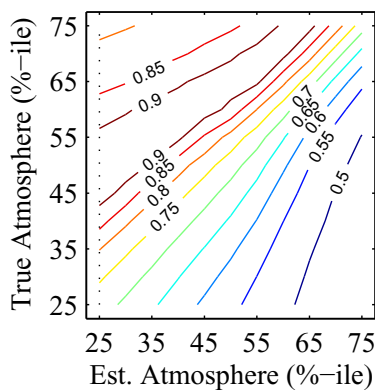
(dd) Green, entire background



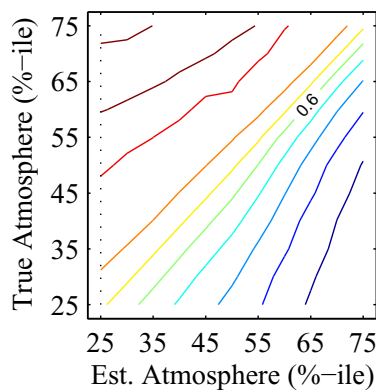
(ee) Green, car-class only



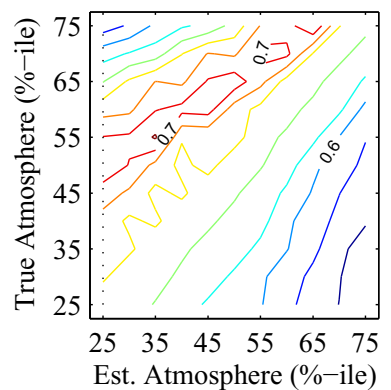
(ff) Green, like-color only



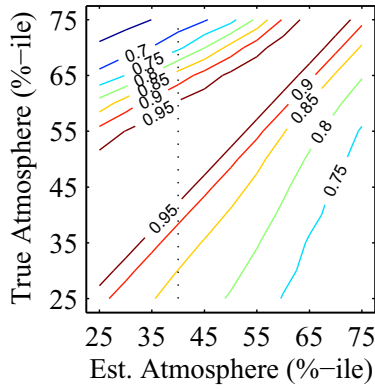
(gg) Maroon, entire background



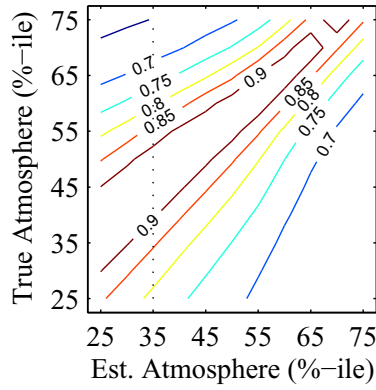
(hh) Maroon, car-class only



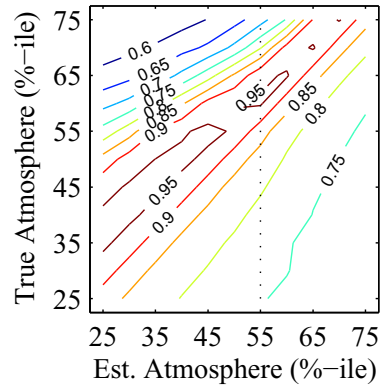
(ii) Maroon, like-color only



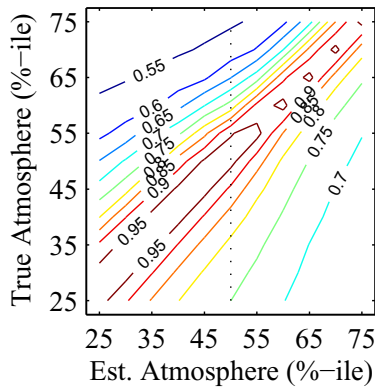
(jj) Red, entire background



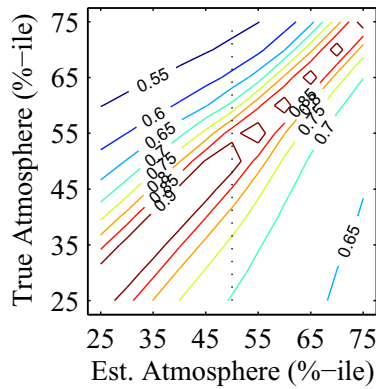
(kk) Red, car-class only



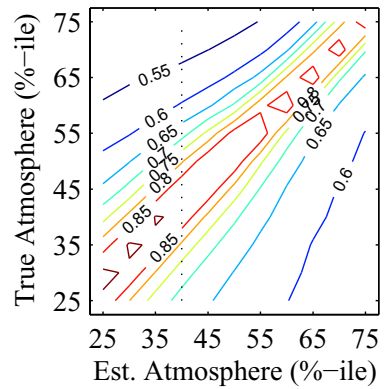
(ll) Red, like-color only



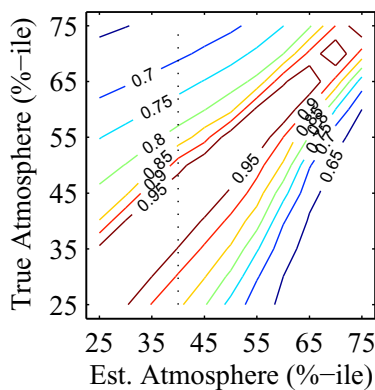
(mm) Silver, entire background



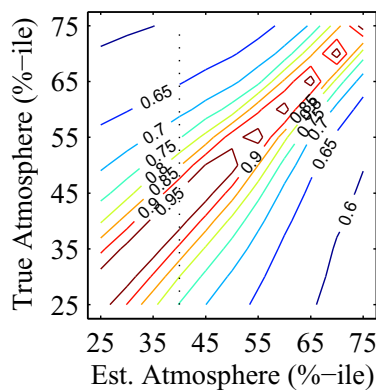
(nn) Silver, car-class only



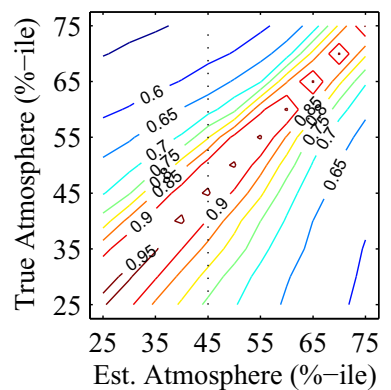
(oo) Silver, like-color only



(pp) White, entire background



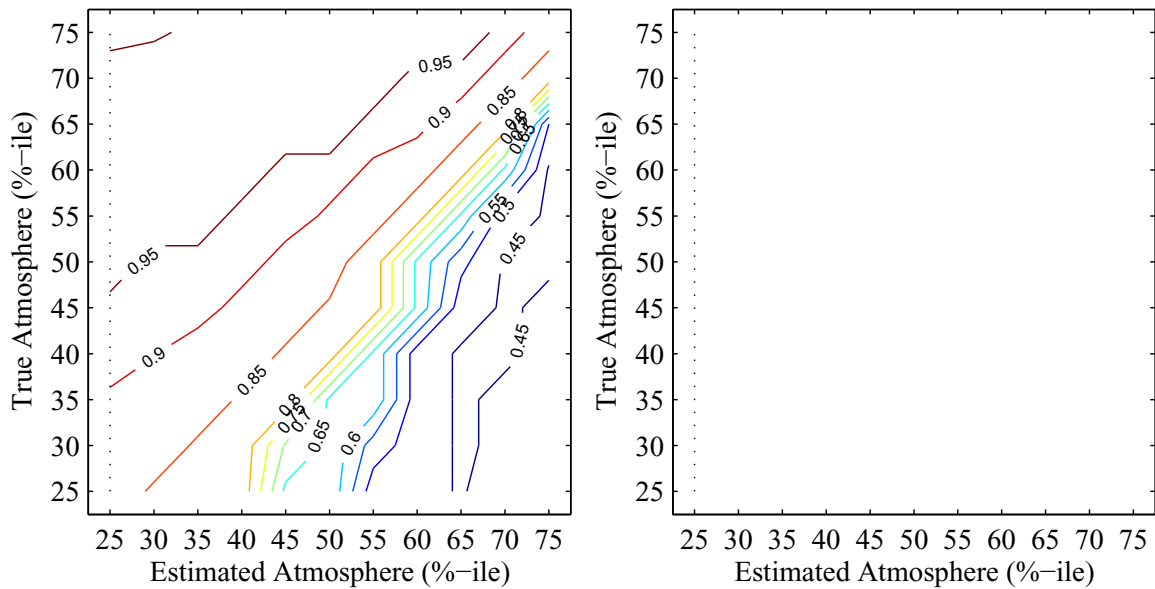
(qq) White, car-class only



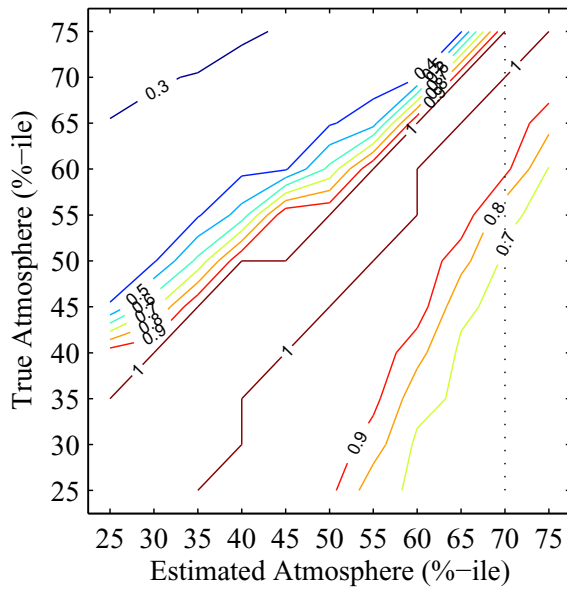
(rr) White, like-color only

### Appendix E. $P_d$ Contour Plots

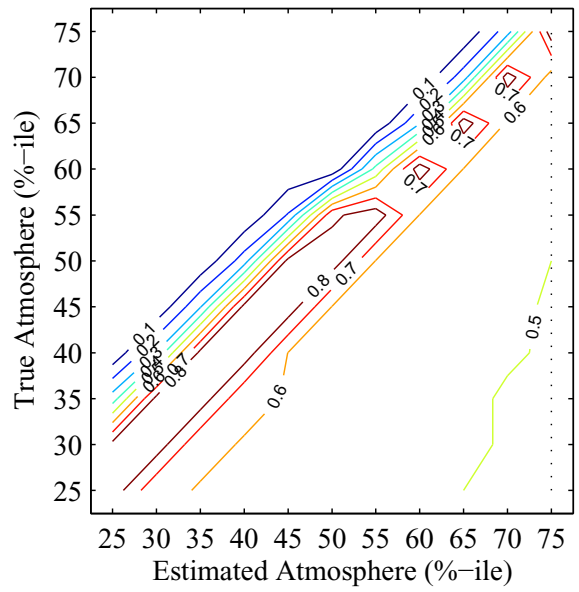
Contour plots of the ROC  $P_d$  at  $P_{fa} = 0.05$  for AMF detection of the indicated automobiles with the  $P_{fa}$ 's calculated from false alarms generated by all background pixels and automobile pixels only. We vary both the “true” image illumination ( $y$ -axis) and the estimated illumination ( $x$ -axis) by their percentiles in the historical distribution at the target site. Note that the estimated illumination percentile that maximizes the  $P_d$  across all possible true illumination percentiles is indicated by the black dotted line. We see that one of the contour plots for detections of the blue car is empty; this is because the  $P_d$  was uniformly zero for  $P_{fa} = 0.05$  among only automobiles.



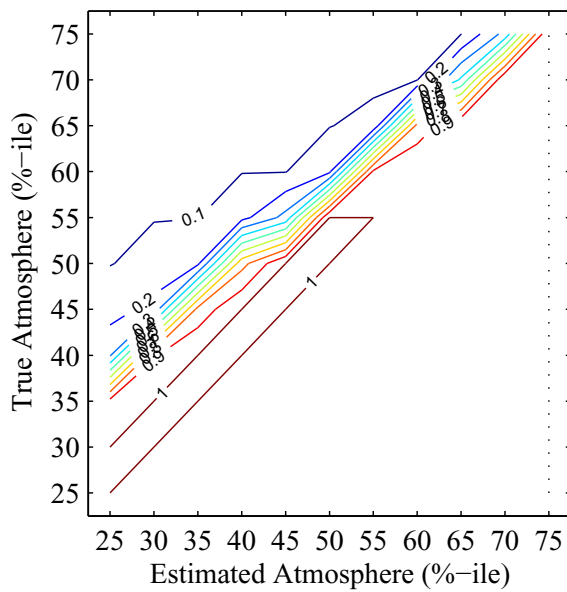
(a) Blue w/ Black Top, Entire Background (b) Blue w/ Black Top, Car-class Only



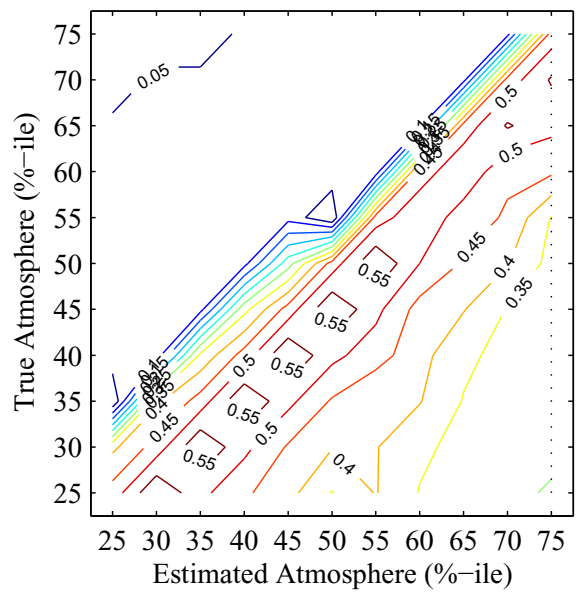
(c) Brown Car  $P_{ds}$ , entire background



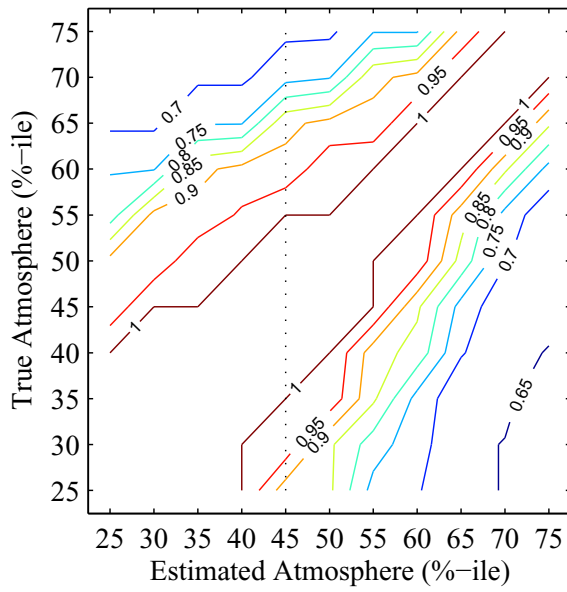
(d) Brown Car  $P_{ds}$ , car-class only



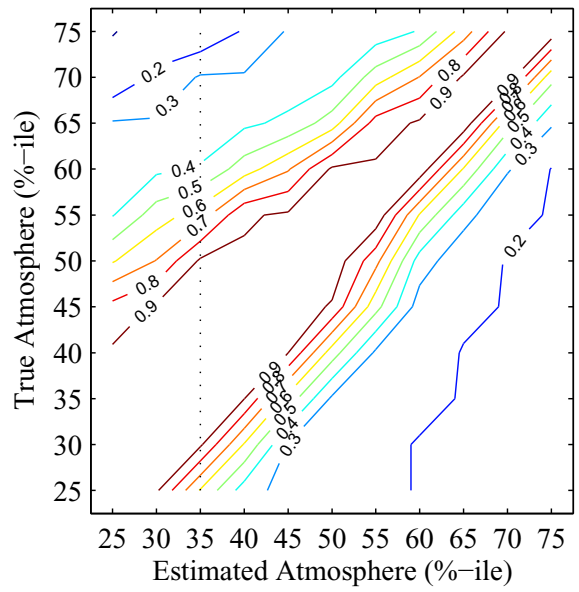
(e) Charcoal Gray, Entire Background



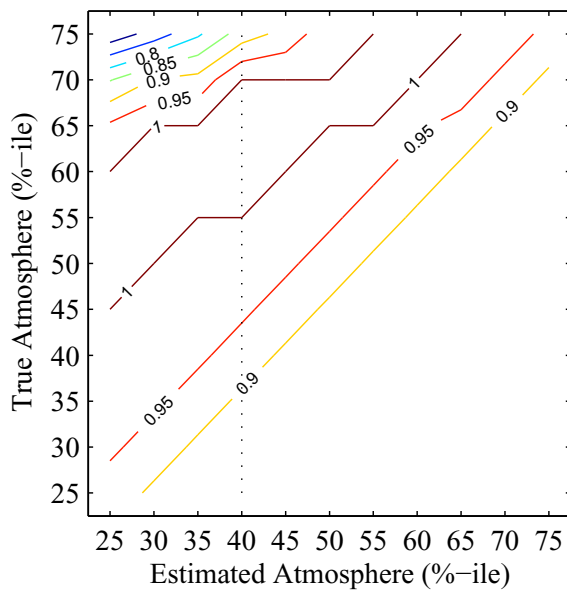
(f) Charcoal Gray, Car-class Only



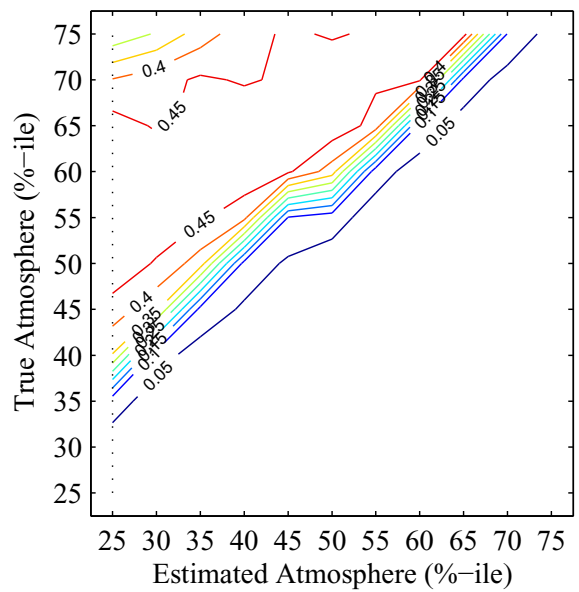
(g) Cranberry Car  $P_{dS}$ , entire background



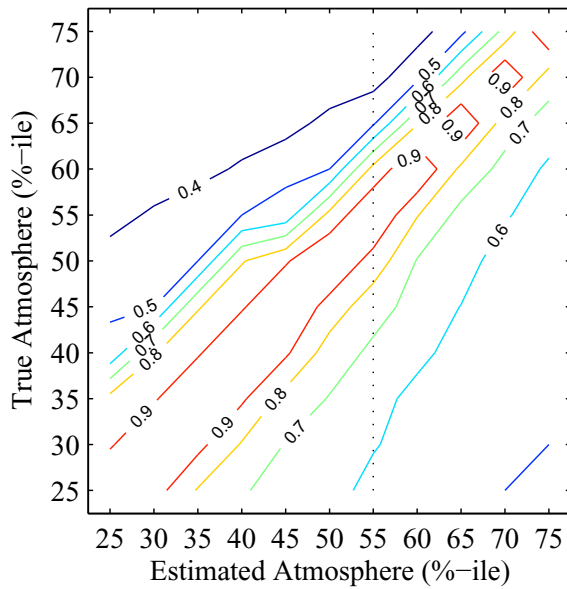
(h) Cranberry Car  $P_{dS}$ , car-class only



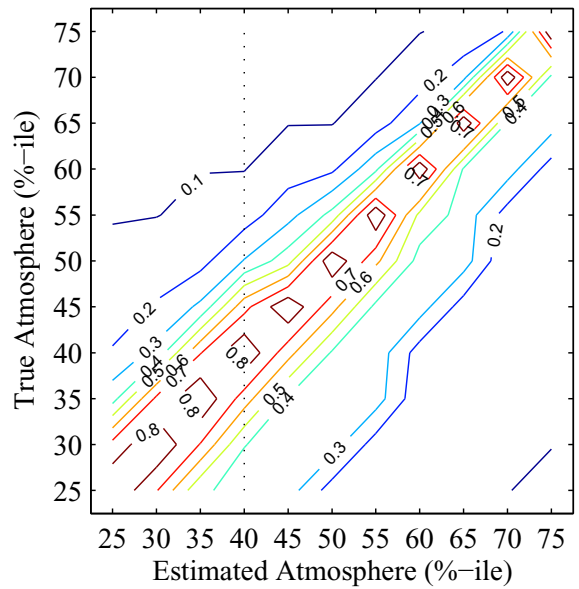
(i) Dark Blue Car  $P_{dS}$ , Entire Background



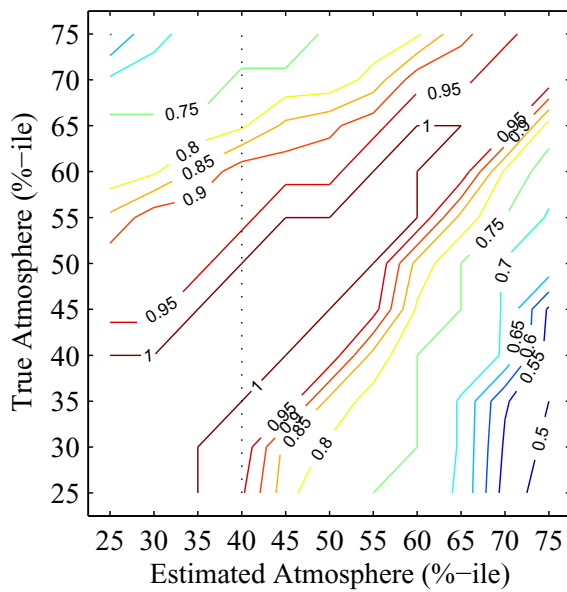
(j) Dark Blue Car  $P_{dS}$ , Car-class Only



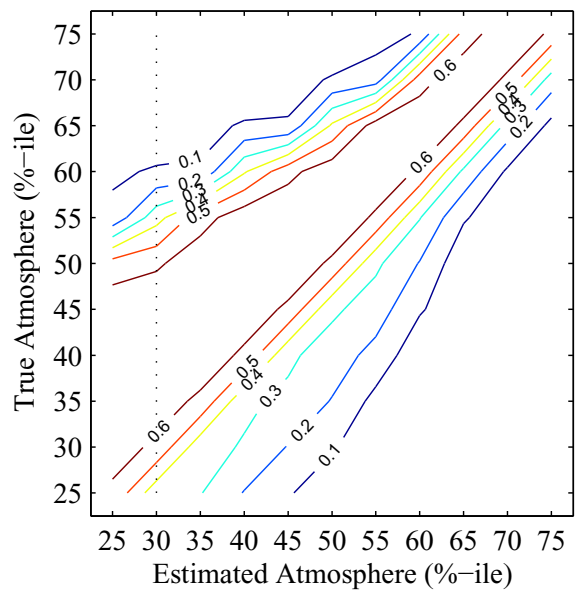
(k) Gray Car  $P_{dS}$ , entire background



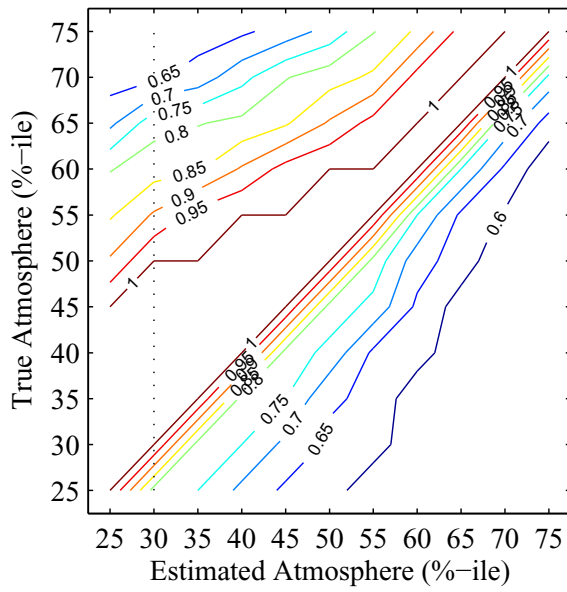
(l) Gray Car  $P_{dS}$ , car-class only



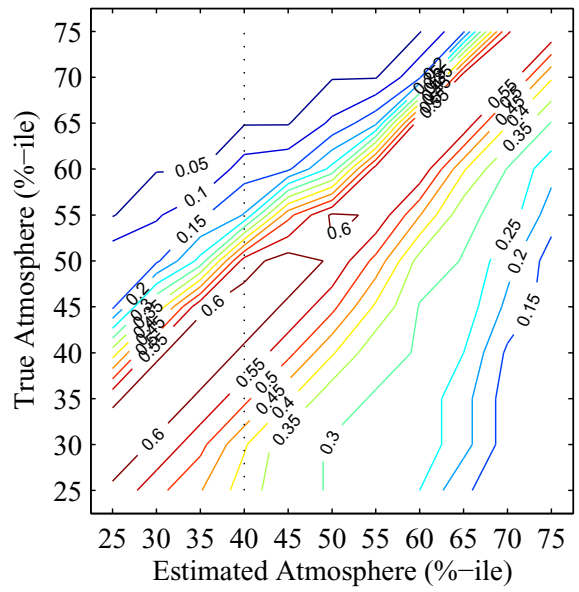
(m) Gray w/ Black Top, Entire Background



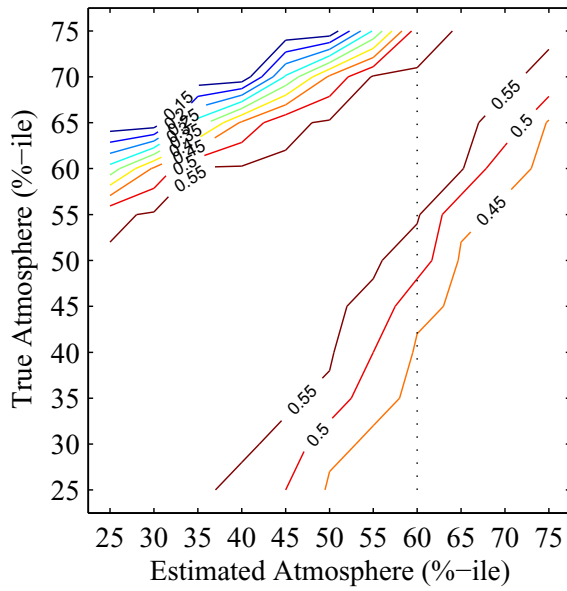
(n) Gray w/ Black Top, Car-class Only



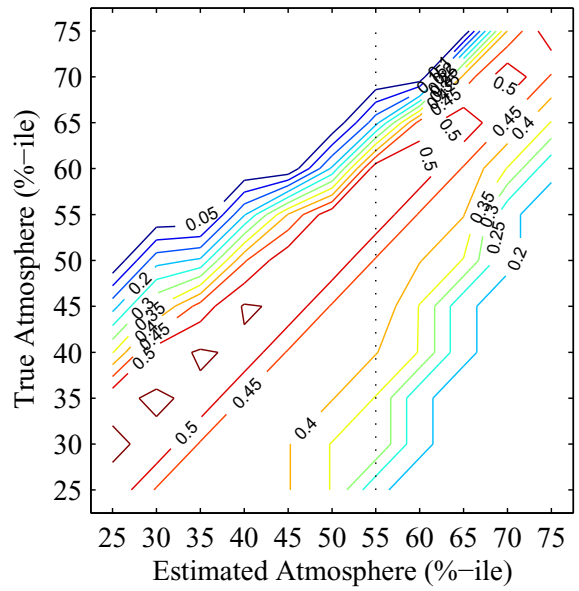
(o) Light Gold Car  $P_{dS}$ , entire background



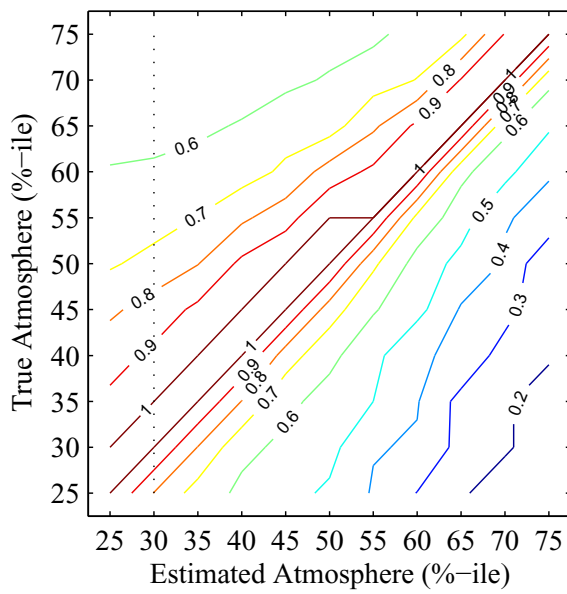
(p) Light Gold Car  $P_{dS}$ , car-class only



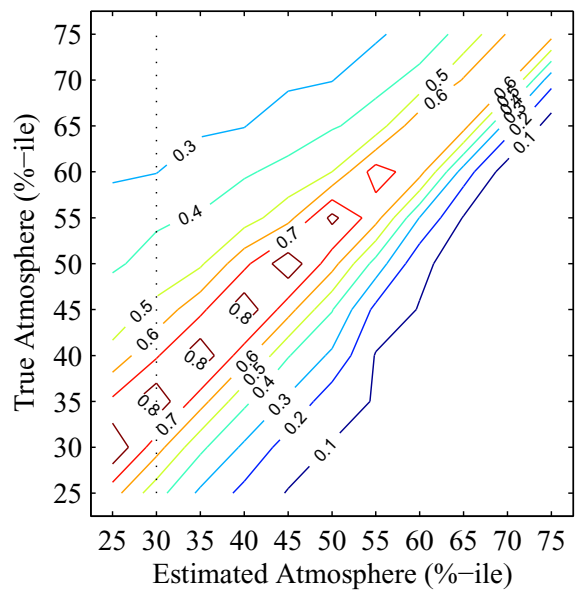
(q) Red-Silver Car  $P_{dS}$ , Entire Background



(r) Red-Silver Car  $P_{dS}$ , Car-class Only

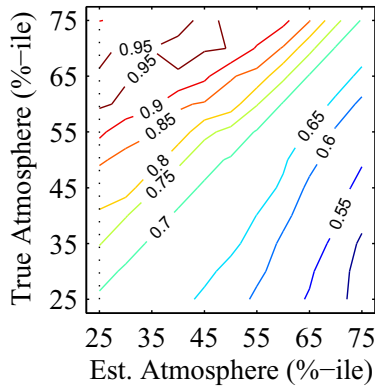


(s) Sterling Car  $P_{ds}$ , entire background

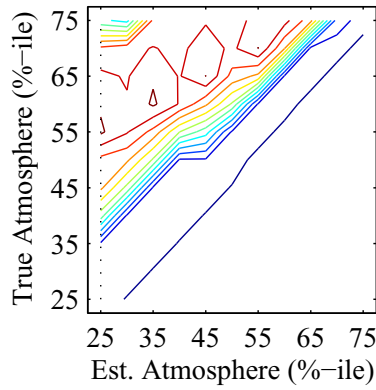


(t) Sterling Car  $P_{ds}$ , car-class only

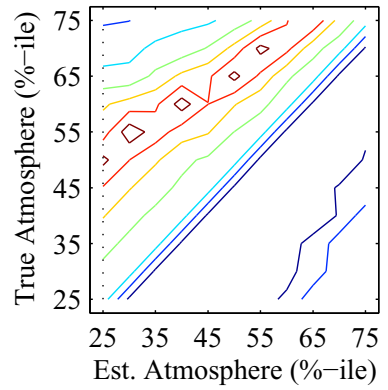
Contour plots of the average ROC  $P_d$  when  $P_{fa} = 0.05$  for AMF detection of the indicated automobiles with the  $P_{fa}$ 's calculated from false alarms generated by all background pixels, automobile pixels only, and like-color automobile pixels. We vary both the “true” image illumination ( $y$ -axis) and the estimated illumination ( $x$ -axis) by their percentiles in the historical distribution at the target site. Note that the estimated illumination percentile that maximizes the  $P_d$  across all possible true illumination percentiles is indicated by the black dotted line.



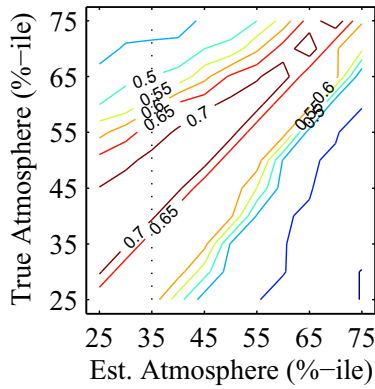
(u) Black, entire background



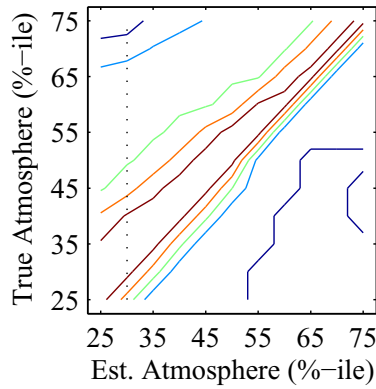
(v) Black, car-class only



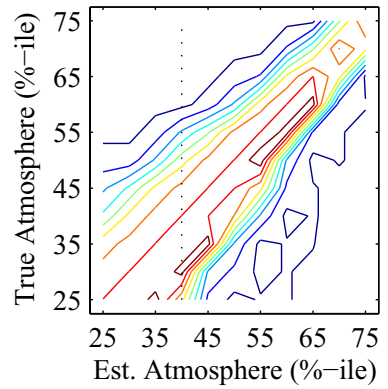
(w) Black, like-color only



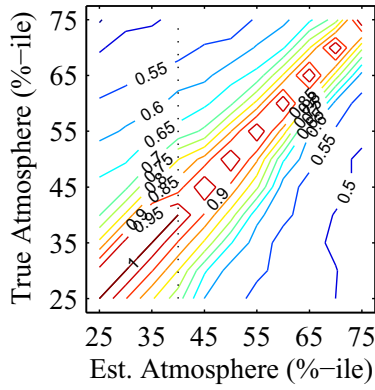
(x) Blue, entire background



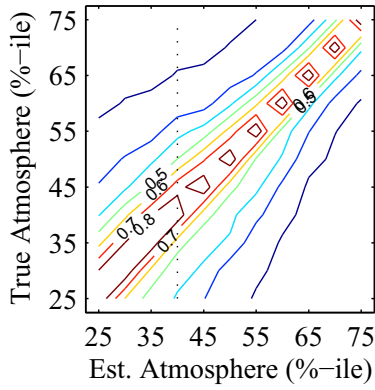
(y) Blue, car-class only



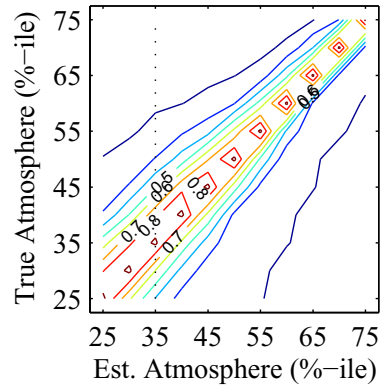
(z) Blue, like-color only



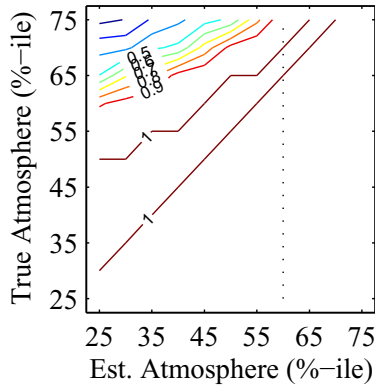
(aa) Gold, entire background



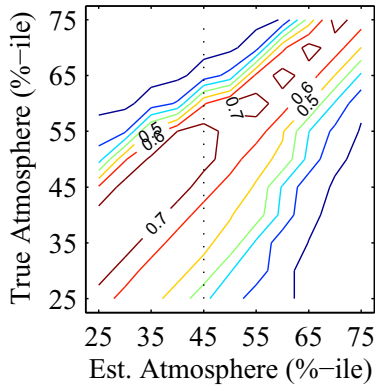
(bb) Gold, car-class only



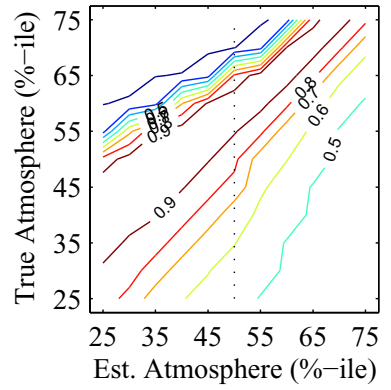
(cc) Gold, like-color only



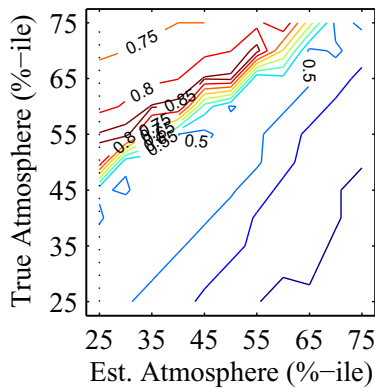
(dd) Green, entire background



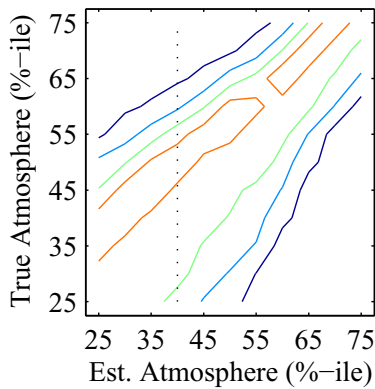
(ee) Green, car-class only



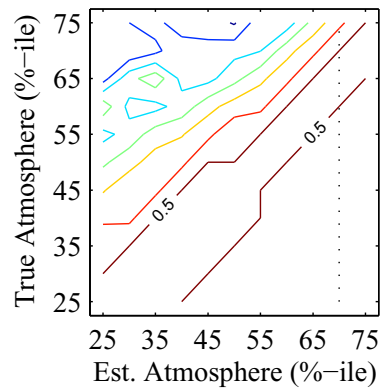
(ff) Green, like-color only



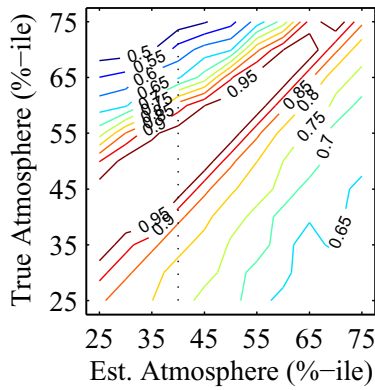
(gg) Maroon, entire background



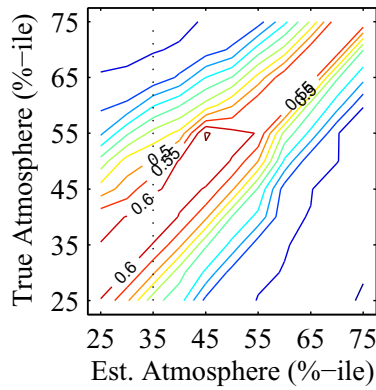
(hh) Maroon, car-class only



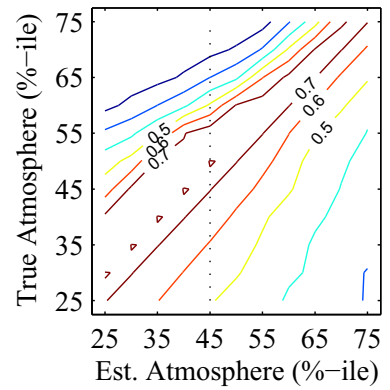
(ii) Maroon, like-color only



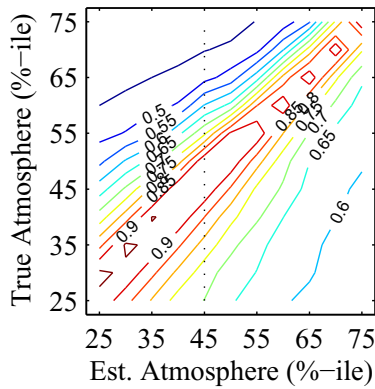
(jj) Red, entire background



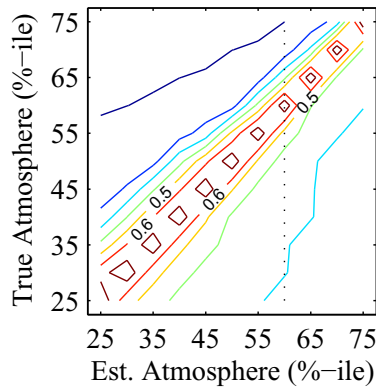
(kk) Red, car-class only



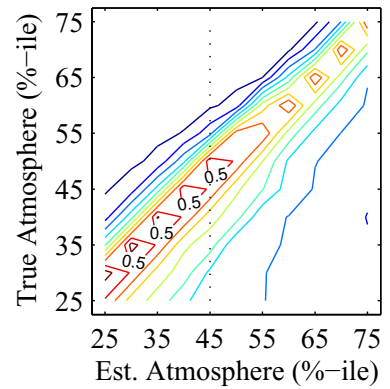
(ll) Red, like-color only



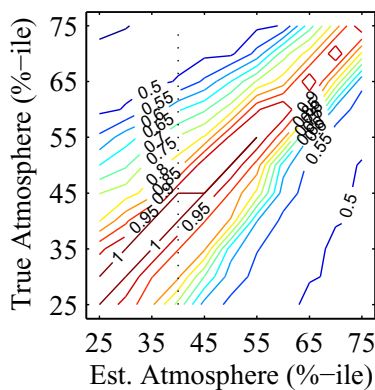
(mm) Silver, entire background



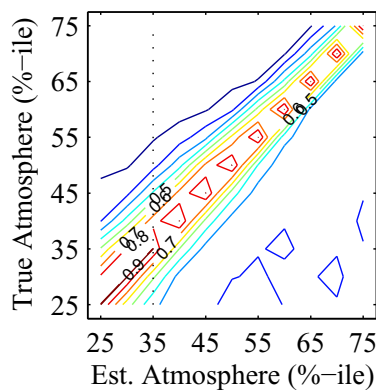
(nn) Silver, car-class only



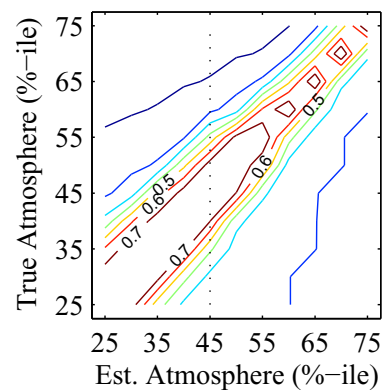
(oo) Silver, like-color only



(pp) White, entire background



(qq) White, car-class only



(rr) White, like-color only

<b>REPORT DOCUMENTATION PAGE</b>			<i>Form Approved</i> <i>OMB No. 074-0188</i>		
<p>The public reporting burden for this collection of information is estimated to average 1 hour per response, including the time for reviewing instructions, searching existing data sources, gathering and maintaining the data needed, and completing and reviewing the collection of information. Send comments regarding this burden estimate or any other aspect of the collection of information, including suggestions for reducing this burden to Department of Defense, Washington Headquarters Services, Directorate for Information Operations and Reports (0704-0188), 1215 Jefferson Davis Highway, Suite 1204, Arlington, VA 22202-4302. Respondents should be aware that notwithstanding any other provision of law, no person shall be subject to a penalty for failing to comply with a collection of information if it does not display a currently valid OMB control number.</p> <p><b>PLEASE DO NOT RETURN YOUR FORM TO THE ABOVE ADDRESS.</b></p>					
<b>1. REPORT DATE (DD-MM-YYYY)</b> 15 Sep 2011		<b>2. REPORT TYPE</b> Dissertation		<b>3. DATES COVERED (From – To)</b> July 2007 – Sep 2011	
<b>4. TITLE AND SUBTITLE</b>  Hyperspectral-Based Adaptive Matched Filter Detector Error as a Function of Atmospheric Profile Estimation			<b>5a. CONTRACT NUMBER</b>		
			<b>5b. GRANT NUMBER</b>		
			<b>5c. PROGRAM ELEMENT NUMBER</b>		
<b>6. AUTHOR(S)</b> Yarbrough, Allan W, Maj			<b>5d. PROJECT NUMBER</b> 08ENG281		
			<b>5e. TASK NUMBER</b>		
			<b>5f. WORK UNIT NUMBER</b>		
<b>7. PERFORMING ORGANIZATION NAMES(S) AND ADDRESS(S)</b> Air Force Institute of Technology, Graduate School of Engineering and Management (AFIT/EN) 2950 Hobson Way Wright-Patterson AFB, OH 45433-7765			<b>8. PERFORMING ORGANIZATION REPORT NUMBER</b> AFIT/DEE/ENG/11-13		
<b>9. SPONSORING/MONITORING AGENCY NAME(S) AND ADDRESS(ES)</b> Air Force Research Lab, Hyperspectral Exploitation Cell Dr. Vincent Velten 2241 Avionics Circle Area B, B620 WPAFB, OH 45433 vincent.velten@wpafb.af.mil			<b>10. SPONSOR/MONITOR'S ACRONYM(S)</b> AFRL/Ryat		
			<b>11. SPONSOR/MONITOR'S REPORT NUMBER(S)</b>		
<b>12. DISTRIBUTION/AVAILABILITY STATEMENT</b> Distribution A. Approved for public release; distribution unlimited					
<b>13. SUPPLEMENTARY NOTES</b>					
<b>14. ABSTRACT</b> Hyperspectral imagery is collected as radiance data. Accurate target detection and classification require that the measurement by the imager matches as closely as possible the known “true” target as collected under controlled conditions and stored in the classification database. Therefore, the effect of the radiation source and the atmosphere must be factored out of the result before detection is attempted. While the spectral profile of solar light is relatively stable, the effect of the atmosphere on this profile varies significantly depending on multiple atmospheric parameters. Our objective is to characterize the uncertainty in the detection method due to the uncertainty in the estimation of atmospheric profiles. We apply a range of atmospheric profiles, correlated with relative humidity, to a radiative transfer model-based prediction of the atmospheric extinction effect using simulated hyperspectral imagery. These profiles are taken from known distribution percentiles as obtained from historic meteorological measurements at the simulated sites. We quantify the expected detection error, given the range of atmospheric conditions in the historic profile. We show that temporal variation in atmospheric parameters across their distribution impacts the accuracy of target detection. We show that, given the uncertainty associated with atmospheric profile estimation, the optimum assumption for purposes of target detection may be other than their median values, and that this effect is target dependent.					
<b>15. SUBJECT TERMS</b> Hyperspectral Imagery, Automatic Target Recognition, Adaptive Matched Filter, Receiver Operating Characteristic					
<b>16. SECURITY CLASSIFICATION OF:</b>		<b>17. LIMITATION OF ABSTRACT</b> UU	<b>18. NUMBER OF PAGES</b>	<b>19a. NAME OF RESPONSIBLE PERSON</b> Dr. Michael J. Mendenhall, Maj, USAF	
REPORT U	ABSTRACT U			<b>19b. TELEPHONE NUMBER (Include area code)</b> 281-733-7389, michael.mendenhall@afit.edu	
c. THIS PAGE U					

**Standard Form 298 (Rev. 8-98)**  
Prescribed by ANSI Std. Z39-18